Aus der

Universitätsklinik für Radioonkolgie mit Poliklinik Tübingen

Sektion Biomedizinische Physik

Establishing clinical cancer treatments with MR-guided adaptive radiotherapy

Inaugural-Dissertation
zur Erlangung des Doktorgrades
der Humanwissenschaften

der Medizinischen Fakultät
der Eberhard Karls Universität
zu Tübingen

vorgelegt von

Nachbar, Marcel

2022

Dekan:	Professor Dr. B. Pichler
1. Berichterstatter:	Professorin Dr. D. Thorwarth
2. Berichterstatter:	Professor Dr. R. Kleiner
Tag der Disputation:	30.03.2022

Contents

Figures

Tables

Abbreviations

CT	computed tomography
CTV	clinical target volume
DFG	Deutsche Forschungsgemeinschaft
DWI	diffusion weighted imaging
DCE	dynamic contrast-enhanced imaging
ERE	electron return effect
ESE	electron stream effect
FBP	filtered backprojection
GTV	gross tumor volume
HU	Hounsfield units
ICRU	International Commission on Radiation Units and Measurements
IGRT	image guided radiotherapy
IMRT	intensity modulated radiotherapy
ITV	internal target volume
KERMA	kinetic energy released per unit mass
LINAC	linear accelerator
MC	Monte Carlo
MRI	magnetic resonance imaging
MLC	multileaf collimator
MRgRT	MR-guided radiotherapy
MU	monitor unit
NTCP	normal tissue complication probability
OAR	organ at risk
PET	positron emission tomography
PTV	planning target volume
QOL	quality of live
TCP	tumor control probability
TPS	treatment planning system

1 Introduction, Aims and objectives of the thesis

1.1 Introduction

Radiotherapy is involved in 50% of cancer treatments worldwide [16]. Its applicability is not limited to a stand-alone treatment, but for a multitude of patients as integral part of a combination therapy, such as chemotherapy, immunotherapy or ablative surgery. Due to its diverse involvement for local therapy of tumor entities, new techniques have been developed in an increasing pace. Whereas new developments were present due to increased knowledge in terms of cell biology and increased clinical experiences, dominant improvements originated in advancing technical capabilities [51, 86, 161].

A milestone of this technical development was the inclusion of anatomical and functional imaging with the purpose to increase tumor control probability (TCP), reduce normal tissue complication probability (NTCP) and in general increase of quality of live (QOL) for cancer patients [82, 139, 174, 186]. This integration of advanced imaging into radiotherapy allowed a three dimensional visualization of targeted structures during therapy. The better visualization of tumor volumes and normal tissue has primarily been implemented in an offline setting on diagnostic imaging systems, but as well on linear accelerators for image guided radiotherapy (IGRT). In IGRT a reference position, for which an optimal treatment was specified, is reproduced with shifts and rotations of the treatment table, based on the daily anatomical information supplied by the imaging systems on the linear accelerator.

The image quality of the X-Ray IGRT systems, on which the daily position of the patient is corrected, thus limits the achievable precision within the treatment. Therefore, margin concepts account for limited soft tissue contrast and also for movement and change of tumor volume during the course of treatment.

Because the acquisition of high quality anatomical and functional images is only possible on diagnostic systems, additional challenges such as patient compliance, increased workforce and correlation between different setups must be acknowledged.

Overcoming this limitation, concepts of hybrid treatment systems, combining a magnetic resonance imaging (MRI) with good imaging capabilities with a linear accelerator (LINAC) have emerged recently [148]. Based on improved daily soft tissue contrast, MR-guided radiotherapy (MRgRT) promises an increased quality of treatments due to better visualization and potential daily optimization of treatment [145]. This daily adaptation on the anatomy of the day is possible due to the high resolution and dose free imaging, which consequently leads to exacter treatments.

Its capability to image moving targets in short time intervals should allow better treatment of targets influenced by respiratory motion (i.e. lung or liver) [49]. In addition, including a scanner with diagnostic quality into daily treatment workflows allows to collect functional information of tumor response during fractionated radiotherapy and consequently to adapt the treatment on a patient specific, individual response [76].

To improve cancer treatments with radiotherapy, based on the above mentioned benefits, hybrid MR-linac systems were developed and first patients irradiated on prototypes [150]. As MRgRT in combination with functional imaging is a primary focus department of radiation oncology tübingen, based on a research grant by the Deutsche Forschungsgemeinschaft (DFG), the 1.5 Tesla MR-linac system should be, as one of the first systems worldwide, established and its additional value researched.

1.2 Theoretical Background

1.2.1 Imaging for simulation and radiotherapy treatment delivery

For image guidance and especially the definition of tumor volumes a variety of functional and anatomical imaging modalities are concurrently employed. Whereas single photon emission computed tomography (SPECT) and positron emission tomography (PET) are supplying only radionuclid specific functional information, magnetic resonance imaging (MRI) and computed tomography (CT) contain in addition anatomical information. Anatomical data derived from CT is additionally

used as a basis for the calculation of dose distributions, because its interaction with matter directly correlates to the atomic cross-sections needed at the therapeutic high energy photons beams. Therefore this theoretical background will focus on MRI and CT, as these are the primary modalities and supply complementary information as shown in Figure 1.

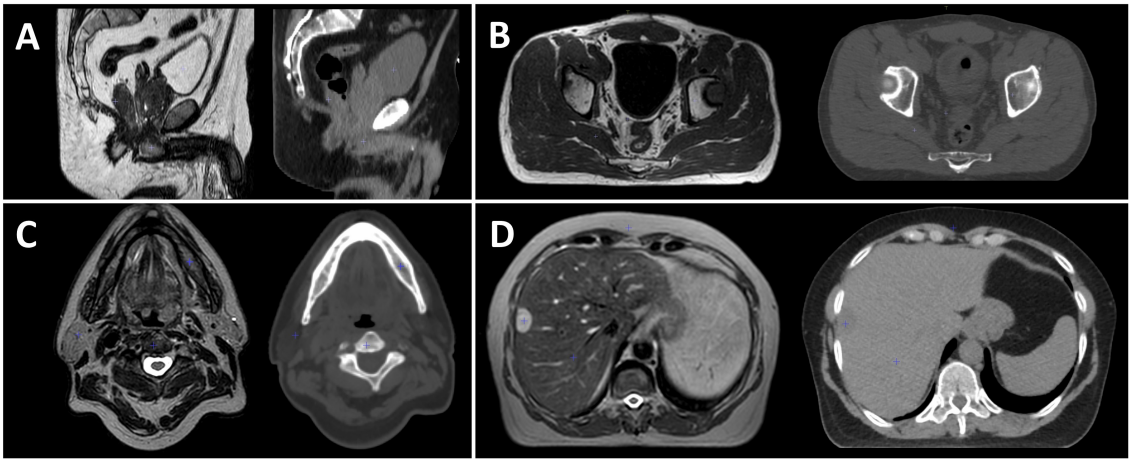

Figure 1: Visualization of differences in contrast between MRI and CT for prostate (A), lymph-node (B), head and neck (C) and liver (D). The left visualizations depict an anatomical MRI, imaged at the 1.5 Tesla MR-linac system and the right side the corresponding planning CT used for dose simulation

1.2.1.1 Computed tomography

Published in 1896 by Carl Röntgen, X-ray imaging is the primarily used modality in radiotherapy [157]. X-ray imaging employs electrons, which are accelerated in a electric field to an energy between 50 and 200 keV. The accelerated electrons are guided on a dense target material on which stopping radiation and characteristic radiation will generate a spectra of photons. Directing this spectrum of photons through a targeted volume and measuring the density based attenuation fluence of passing photons is the principle of X-ray imaging. In this energy range the dominant interaction of photons is the photo-electric effect, of which the cross-section τ is proportional to $\tau \propto \rho \cdot Z^{(4-4.5)}$, resulting in a clear differentiation between materials with different number of protons [67]. The 2-dimensional detection of attenuated photons corresponds to planar imaging and the 3-dimensional reconstruction to computed tomography (CT). For a creation of 3-dimensional volumetric data, a multitude of 2D projections are generated as a function of their angle of entrance, ranging from 0° to 180°. The generated angle dependent attenuation sinograms can generally be

reconstructed to 3-dimensional volumes using a radon transformation. Due to random noise on a general back-projection of the image, a filtered backprojection (FBP) which enables a high-pass filtering in the Fourier space, was applied till 2009. This analytic method however is since then, even in commercial systems, replaced by iterative methods, generating a better image quality even for low dose CTs [198]. To allow quantitative comparison of imaging data between scanners, voxel assigned attenuation coefficients are normalized after reconstruction by:

$$HU(\mu) = 1000 \cdot \frac{\mu - \mu_{Water}}{\mu_{Water} - \mu_{Air}}, \tag{1}$$

in which μ denotes the attenuation coefficient. The Hounsfield units (HU) generally varies in patients between -1000 and 3000. Due to its visual representation of photon attenuation the CT has great spatial information and can be directly correlated to electron density. However, since its attenuation is based on interactions with electrons, differentiations between soft tissues are limited (cf. figure 1).

1.2.1.2 Magnetic resonance imaging

Magnetic resonance imaging has been developed in the early 1970s by Damadian, Lauterbur and Manfield [43, 103, 115]. In contrast to the CT, which generates information based on electron interactions, the MRI uses a signal information from the nucleus. Individual parts of the atomic nucleus, protons and neutrons, exhibit an angular moment, called spin. For an even number of protons and neutrons within the nucleus these angular moments cancel each other out. With an odd number of one or both of them, a resultant spin per nucleus is present and can be detected.

Situated in an external magnetic field however, resultant spins will align parallel or anti-parallel to the magnetic field lines. If the two resulting oriented spins differ in number, the absolute difference can be instrumentalised for the generation of signal and subsequently imaging. The amount of different spin orientations is dependent on the external magnetic field, the temperature of the material and on the type of atom. For one million hydrogen (H) nuclei, this corresponds at a body temperature of T =36.5° Celsius and a static magnetic field of 1.5 Tesla to five more aligned nuclei along the magnetic field [70].

Depending on the static magnetic field, spins are rotating, based on their atom

specific gyro-magnetic constant, in their respective larmor frequency [178]:

$$w = \mu \cdot B_0. \tag{2}$$

With a gyro-magnetic constant of water $\mu_{H20} = 42.58$ MHz/Tesla, this corresponds to a larmor frequency of 63.87 MHz for conventionally used 1.5 Tesla static magnetic fields. By applying a high frequency (HF) field radio wave on this specific frequency, spins can be tilted up to an angle of 180° from their original orientation. After pulse application, spins align back in their original orientation in a time depending on their surroundings. This precession can be detected by an antenna as a decrease of magnetization and is referred to as longitudinal or T1-time:

$$M_z(t) = M_0 \cdot (1 - exp^{\frac{t}{T_1}}). \tag{3}$$

Measuring not the individual spin decrease of the longitudinal magnetization, but a dephasing of the spin precession in regards to the transverse magnetization corresponds to the spin-spin-relaxation or T2-time:

$$M_f(t) = M_t(0) \cdot exp^{\frac{-t}{T_2}}. \tag{4}$$

Spatial encoding of detected signal in an MR-system is based on varying magnetic field gradients in different directions. Whereas the slice selection in the z-direction and the frequency encoding in x-orientation are based on applying magnetic field gradients differentiating larmor frequencies of voxels, phase encoding is based on varying the magnetic field on readout generating a phase shift.

The first image reconstructions of the readout data were based on FBP. Today's medical scanners record signals in the frequency space (k-space) and translate them into a spatial image by Fourier transformation. The main benefit of MRI is the high soft tissue contrast and the potential to perform functional imaging, without applying radiation dose. However, due to its spatial encoding, differences in the static magnetic field due to artefacts, chemical shifts, magnet inhomogeneities or movement may result in geometric distortion leading to an incorrect position of the detected anatomies in the spatial images [171].

1.2.2 Linear accelerator system

While the first linear accelerator (LINAC) systems [62] were already developed and built in 1928 at the RWTH in Aachen by Rolf Wideröe, the decay of radionuclide for the irradiation of patients has been for long the primary system in radiotherapy. In a current modern clinical setting, LINAC systems accelerate electrons with alternating voltage, based on walking- or standing-wave, to a kinetic energy between 2 and 30 MeV [68]. The accelerated electrons can be used directly for the irradiation of eg. tumors close to the skin surface or guided onto a tungsten target generating a bremsstrahlung photon spectrum for the irradiation of deep-seated tumors. For patient treatments the created photon fluence is highly modulated in modern treatments of intensity modulated radiotherapy (IMRT). For this modulation, on a first level the distribution will be limited by diaphragms in x- and y-direction generating rectangular fields. This is then further shaped by multileaf collimator (MLC), consisting of up to 160 individual tungsten leafs with a projected leaf width at patient level of down to 5 mm, and individual sub-millimetre positioning (cf. figure 2). For a directional variation of the beam direction, the accelerator head, in which these fluence limiting structures are positioned, rotates around the patient and orthogonal to the beam direction. In combination with variable dose rates, there is a high number of free parameters, which can be optimized to achieve the most favourable patient specific treatment. The degrees of freedom correspond to:

$$
\begin{aligned}
\text{Segment} = \{ & \textstyle\sum_{i=1}^{2} Diaphragm_x(i) \\
& + \textstyle\sum_{j=1}^{2} Diaphragm_y(j) \\
& + \textstyle\sum_{k=1}^{80} MLC_{Y_1}(k) \\
& + \textstyle\sum_{m=1}^{80} MLC_{Y_2}(m) \\
& + Angle_{Gantry} \\
& + Angle_{Collimator} \\
& + MU \\
& + dose\,rate\}
\end{aligned}
$$

Figure 2: Exemplary accelerator head configuration for a prostate cancer patient. Depicted in green are individual MLC positions. The red cross marks the isocenter.

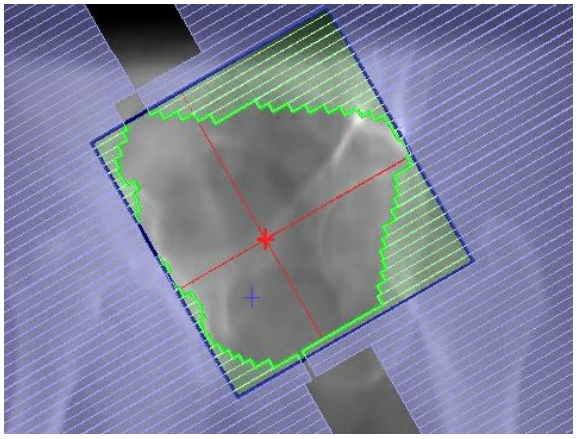

1.2.3 Simulation of dose deposition

A high complexity of free parameters in the accelerator head in combination with a high variability of patient anatomy, has induced a drastic improvement on simulation systems for dose distributions in a clinical setting over the last decade. First calculations were using pencil beam algorithms to calculate distributions of radiotherapy doses. This was based on MLC-position weighted infinitely small rays from the accelerator head, which simulated the deposition of dose based on pre-measured data in water [64]. For the treatment of patients, of which the densities differ to water, these individual rays were stretched or compressed based on the relative electron density of materials they pass trough. Whereas this algorithm is still used for protons today, it creates a wrong distribution for photons, as secondary electrons are spread out from their trajectory and therefore neglected in this model. In a next step super-positioned convolutional kernels were developed [5]. This algorithm, often referred to as collapsed cone, used upfront calculated kernels of the dose distribution deposited by secondary electrons on the given accelerator energy. In combination with a measurement based detection of primary interaction of photons or kinetic energy released per unit mass (KERMA), the dose could be simulated accurately for most anatomies. However, these algorithms were depending on measured dose calculations in water and in consequence exhibit problems for materials with different densities [97]. In consequence with the rise of computing powers, supplying the possibility to simulate the interactions between atoms and therefore deriving from analytical methods, Monte Carlo (MC) based algorithms were introduced. In MC based algorithms the interaction probabilities for materials as well as the different interactions are simulated for individual photons based on the Boltzmann transport equation [46].

Even though full MC-simulations are available in different platforms i.e EGSnrc, GEANT4 or Penelope [9, 15, 79], simulating the full life of particles, especially electrons ,need a large amount of calculation resources. Therefore in a clinical setting fast MC algorithms are being used, which start with a photon spectrum on the end of the accelerator head and, in combination with a form of raytracing and variance reduction methods, allow for a clinical optimization time reproducing experimental data correctly within certain limits [52].

1.2.4 Treatment planning

Based on patient diagnosis and decision in an interdisciplinary meeting, for a treatment with radiotherapy, a planning CT is executed in treatment position. This 3D volume of the patient is segmented into target volumes and organs at risk (OAR). These manual or AI-based annotations are validated and corrected by specialized physicians including additional anatomical and functional information from positron emission tomography (PET) or MRI. Uncertainties between the different modalities, mainly different positioning or temporal differences are minimized by rigid of deformable image registrations, before margin concepts are added.

1.2.4.1 Margin concepts

Margin concepts were introduced by the International Commission on Radiation Units and Measurements (ICRU) 1993 and are accounting for uncertainties in annotations as well as treatment application [83, 102]. Based on the delineation of the gross tumor volume (GTV) in a first step, to account for clinical infiltration, which is not visible based on imaging data, a clinical target volume (CTV) is created by adding a certain safety margin to the GTV. A subsequent margin is used from the CTV to the planning target to account for uncertainties in planning and delivery. This margin from CTV to planning target volume (PTV) takes into account all geometrical errors, machine errors, organ movement and deformations that the CTV is certainly irradiated with the prescribed dose to the PTV. Whereas the ICRU 62 [102] and Stroom et al. [170] published margin recipes, most commonly used formulas are based on a model published by Van Herk et al. [72]:

$$Margin = 2.5 \cdot \Sigma + 1.64 \cdot \sqrt{(\sigma_P^2 - \sigma^2)} - 1.64 \cdot \sigma_P^2 \tag{5}$$

in which, σ_P defines the penumbra width. When this is set to a commonly used value of 3.2 mm this formula can be simplified to:

$$Margin = 2.5 \cdot \Sigma + 0.7 \cdot \sigma \tag{6}$$

For this statistical model, with the derived margin, for 90% of patients the CTV should be irradiated with at least 95% of the prescribed dose to the PTV [73]. This model differentiates between systematic (Σ) and random (σ) errors in the treatment process. Systematic errors Σ account for errors in the generation of the treatment plan and correspond to a type 1 error leading to systematic mistreatment. The

random error σ however represents errors arising on every day of patient irradiation. Even though the time point of the error in this formula is the most important variable, the primary reason for errors are the same on both: Delineation, organ motion, setup error, intrafraction motion.

1.2.4.2 Intrafraction motion management

One of the most dominant sources for errors during fractionated irradiation is intrafraction motion. Whereas random motion is difficult to model, additional concepts are used for the movement of target structures influenced by periodic respiratory motion. These are all tumor entities in proximity to the diaphragm, but predominantly lung and liver cancer. The tumor position in this case is not fixed but changes based on the respective respiratory cycle (cf. figure 3).

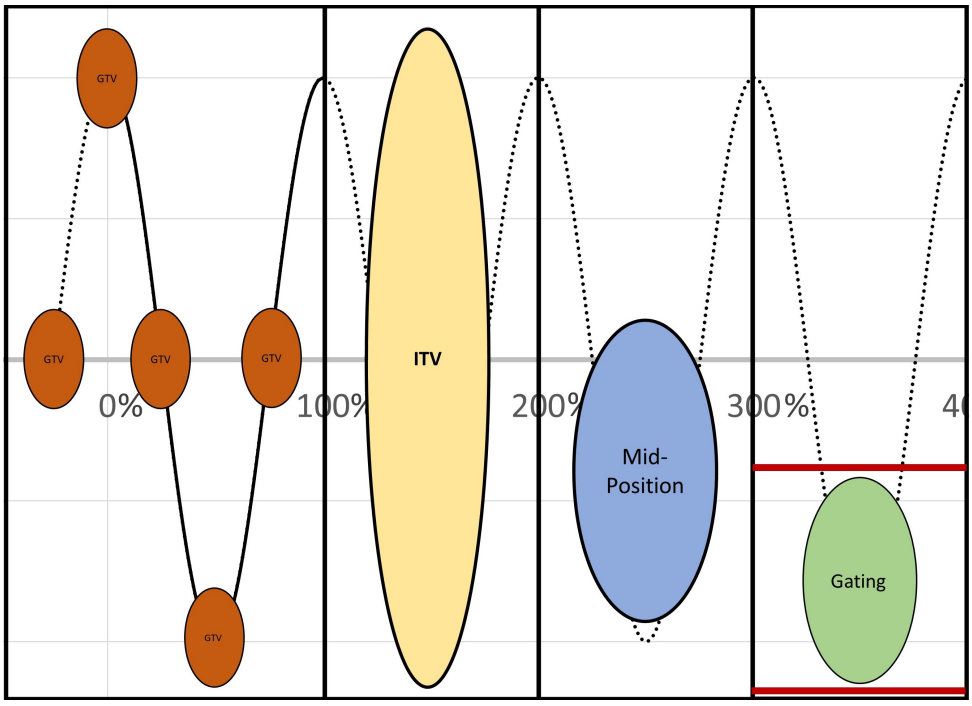

Figure 3: Theoretical one dimensional schema depicting the different margin concepts for tumors influenced by respiratory motion. Depicted in orange is the true position of the GTV within an respiratory cycle. The breathing curve is shown in respect to the respiratory cycle denoting the maximum inhale at 0% and the maximum exhale at 50% repeating in a cycle every 100%. In light yellow shown is the ITV concept covering every possible GTV position. In blue shown, is the mid-position concept, which is shifted to the more dominant exhale phase within a breathing cycle. In green shown is the gating concept, for which a gating window (red) is defined, only in which radiation would be applied.

Two distinct methods are used to account for such regular motion. For the internal target volume (ITV) concept, in the planning state, a 4D CT is being executed, and different respiratory cycles are reconstructed (cf. figure 3). In every cycle the tumor position is identified and all possible positions are combined to create a new target volume, the ITV. In this concept it is ensured, that the target structure will be covered by the prescribed dose in every possible respiratory cycle [21, 47, 55]. In a more advanced concept, a time averaged mid-position CT is reconstructed to minimize the target irradiated area [98, 108]. Based on the respiratory cycle, a deformed image registration is calculated between the different breathing phases to generate a theoretical CT, even though this position never truly exists [200]. This arithmetic generation of a theoretical CT results in a shrinkage of the PTV for lung cancer of approximately a factor of 1.2. Both concepts are used in a free-breathing setup, often combined with an abdominal suppression to minimize motion. However, these concepts are all accompanied with the irradiation of a substantial amount of healthy tissue due to the required margin sizes.

With the aim to reduce the amount of healthy tissue irradiated, new concepts were developed: Gating, meaning the irradiation of the target only at one time-point during the respiratory cycle (cf. figure 3) and tracking, which is an irradiation method where the target volume is tracked and the treatment beam moves according to the tumor position in the respiratory cycle [47, 60]. Most of these setups use motion surrogates, i.e. by scanning the patient surface, or directly measuring the respiratory cycle by active breathing systems. Nevertheless, MRI and X-ray are being introduced in this workflow for the direct positional identification of target volumes.

1.2.4.3 Treatment plan optimization

Following CT annotation and patient individual definition of uncertainties according to the margin concept, the ideal configuration of MLC and all other machine parameters in combination with dosage and beam entrance angle need to be defined. Whereas for simple anatomies the configuration is done manually be a specialist, defining first the machine parameters and then calculating the dose distribution, the degrees of modulation for more complex target structures is highly complex and require mathematical optimizations. In such inverse planning approach a configuration of objectives and constraints is defined upfront representing a dose distribution [8, 26]. These predefined dose distribution parameters are linked to the tumor control probability (TCP) and normal tissue complication probability (NTCP) [18].

The definition of constraints and objectives is formulated in the treatment planning system (TPS) as a problem based on Lagrange multipliers. The equation is solved with an iterative optimization, incorporating the fluences of respective MLC positions. However, since for every planning process the formulation of objectives and constraints can be executed in different ways, each resulting in different results, this step is very specific to the formulation of the problem.

1.2.4.4 Biological concept

Due to differences in cell biology and respective cell origin, tumor cells and healthy tissue cells have different sensitivities to radiation. Cell sensitivity to radiation dose can be described by a two parameter linear-quadratic model (LQ-Model) with an alpha/beta-value ($\frac{\alpha}{\beta}$) characterizing the survival rate of irradiated cells [27, 190]:

$$S = exp^{-\alpha \cdot D - \beta D^2}, \tag{7}$$

in which the linear α term characterizes a single-hit cell kill and the quadratic β term a multi-hit cell kill [30].

The main goal of all advances in radiotherapy is to minimize NTCP while maximizing TCP, which is referred to as the therapeutic window [18, 181]. This describes the probability of tumor control due to deposition of dose into tumor tissue in correlation to the probability of normal tissue complication as shown in red in figure 4. With the solid line the tumor control probability (TCP) for prostate tumor is represented in contrast to the normal tissue complication probability (NTCP) of chronic ($\geqslant$ grade 2) rectal bleeding (dotted line).

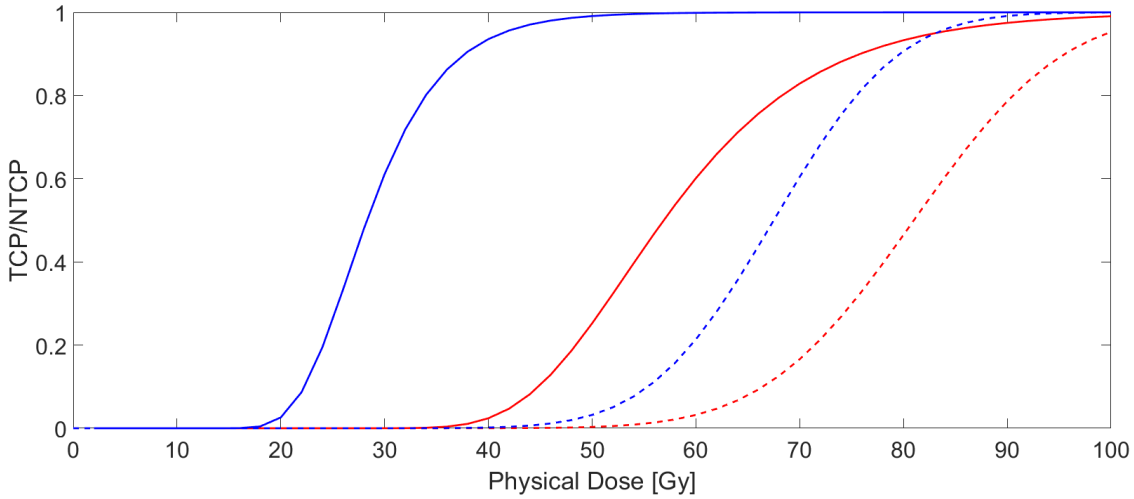

Figure 4: Biological effects of radiation for prostate tumor (solid lines) and for normal rectal tissue (dotted lines). Red depicts a treatment at conventional 2 Gy/Fx, whereas blue depicts a hypofractionation at 3 Gy/Fx. Depicted are the differences in TCP (solid line, $\frac{\alpha}{\beta} = 1.4$) to chronic ($\geqslant$ grade 2) rectal bleeding NTCP for the rectum (dotted line, $\frac{\alpha}{\beta} = 3$)[116, 124]

Normal tissue complications are the main prohibiting factors of radiotherapy, restricting better tumor control. Therefore, with a better differentiation between respective dose points on the two curves, a better tumor control by equal complications is possible. In a simplistic approach this is possible by applying dose only to the target and minimal dose to normal tissue resulting in high TCP with low NTCP [105, 124].

To enable this, the margin of target structures must be minimized to the structure itself and a clear differentiation between normal and cancerous tissue is needed. Next to treating as conformal as possible, additional ways of widening this window are to sensitize tumor cells for radiotherapy or generate a resistance again radiation in normal tissue [125, 127].

However, an additional concept is to apply the total dose in several fractions to the patient over a longer period of time, and in this way utilizing the different repair capabilities of tumor and healthy tissue.

Fractionation sensitivity is characterized by the $\frac{\alpha}{\beta}$ value, differentiating between low sensitivity with high values, i.e. $\frac{\alpha}{\beta}$= 10 Gy for head and neck squamous cell carcinoma, to an high size sensitivity for low values, i.e. $\frac{\alpha}{\beta} = 1.4$ Gy for prostate [105, 124]. The conventional clinical fractionation scheme is 1.8 - 2 Gy per fraction. A daily dose below 1.8 Gy is referred to hyperfractionation and more than 2 Gy to hypofractionation.

Different fractionation methods are chosen based on the respective cell biology and intended increase of treatment quality. To compare different fractionations, the current standard is to calculate the equivalent uniform dose (EQD2). The EQD2 is calculated, based on the $\frac{\alpha}{\beta}$ as follows:

$$EQD2 = Dose_{Total} \times \frac{Dose_{Fx} + \frac{\alpha}{\beta}}{2 + \frac{\alpha}{\beta}} \tag{8}$$

Figure 5 shows, that the EQD2 does not change for a standard fractionation of treatment (red). However, for a hyperfractionation (blue) the EQD2 for the fractionation sensitive prostate tumor (solid line, $\frac{\alpha}{\beta} = 1.43$ Gy) changes in comparison to the EQD2 of the rectum (dotted line, $\frac{\alpha}{\beta} = 3$ Gy). At this comparison of different fractionation sensitivities a hypofractionation would result in a greater equivalent uniform dose to the tumor in comparison to healthy tissue and therefore, this additional equivalent dose at a higher fractionation size would result in a better differentiation between NTCP and TCP as shown in figure 4 in blue.

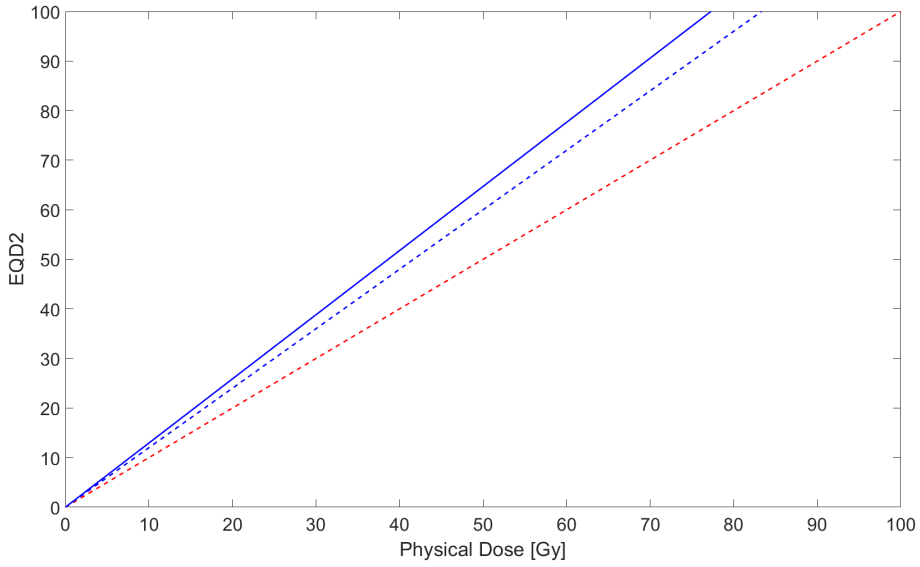

Figure 5: Shown is the comparison of the equivalent uniform dose at 2 Gy (EQD2) per fraction over the applied physical dose for an $\frac{\alpha}{\beta} = 1.4$ (solid line) and $\frac{\alpha}{\beta} = 3$ (dotted line). Red depicts a treatment at conventional 2 Gy/Fx, whereas blue depicts a hypofractionation at 3 Gy/Fx.

1.2.5 MR guided radiotherapy

For the patient position verification on the treatment table, today X-ray imaging is the clinical standard for image guided radiotherapy (IGRT) [19, 117]. Other imaging techniques have up to this point not been introduced. Therefore, the introduction of MRI into the treatment room was the next logical step, promising better soft tissue differentiation, functional imaging and radiation free imaging of the patient. However, the inclusion of a magnetic field into the radiotherapy treatment room was a major challenge, since neither the equipment nor the calculation algorithms were pre-designed to be compatible with magnetic fields. To minimize its influence, the inclusion of MRI has been realized in different complexities, prioritizing different objectives. Four different systems are available worldwide [44], out of which only two systems are used commercially. However, these two clinical systems have chosen very different approaches to the extent of magnetic field inclusion. The MRIdian linac (ViewRay Inc., Oakwood, USA) intended as little influence of the magnetic field as possible, instrumentalizing a static magnetic field of 0.35 Tesla. The second system, which will be explained in detail is based on a complete new design and inclusion of a 1.5 T static magnetic field, with a state of the linear accelerator (LINAC) system.

1.2.5.1 Technical Design of the 1.5 T MR-Linac

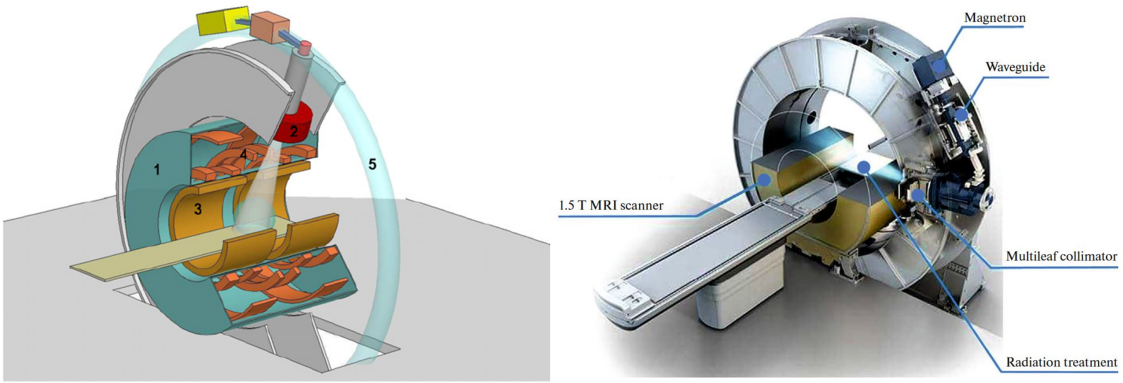

Figure 6: Shown on the left is the concept published by Raaymaker et al. [152] and on the right in correspondance the final developed and CE-marked Elekta Unity MR-linac system [23].

The 1.5 Tesla MR-linac (Unity, Elekta AB, Stockholm, Sweden) is a newly designed linear accelerator system combined with a magnetic resonance tomography system, developed by Raajmakers and Lagendjik [152] at the University of Utrecht (cf. figure

6). The goal for this hybrid system was the inclusion of a diagnostic scanner, in order to achieve high quality MRIs, into the treatment of patients. However, irradiating through a conventional MRI was not possible, as all the high density regions, such as the gradient coils and different shimming objects would have composed attenuation sources barely manageable for the simulation of dose distributions on the patient.

Since a homogeneous static magnetic field however, is the main prerequisite of a MR-scanner, creating a full gap with a split magnet system, as it is used for the MRIdian, was not possible for 1.5 Tesla. Therefore a quasi-split magnet design was developed, leaving a small gap between the gradient coils, but connected with a small pipe. In this gap cryostat and different less attenuating material components are still present, but are positioned homogeneously around the angle of entrance with respect to the radiotherapy beam and therefore considered manageable. With this design the Unity system exhibits the characteristics shown in table 1, based on the vendor supplied technical build and data generated in a multicentre study [176]:

Table 1: Detailed characterization of the MRI system, specified by the vendor for the technical build and based on the commissioning data of a multicentre study published by Tijssen et al. [176]. The B0 homogenity is given an for the 35 cm diameter of spherical volume DSV and the ghosting at echo planar imaging (EPI)

Technical build		**Commissioning testing in the multicenter study**	
Bore diameter	70 cm	B0 homogeneity (35 cm DSV)	0.9 ±0 ppM
Bore length	130 cm	Flip angle accuracy	0.35 ±0.2 %
Gradient amplitude	34mT/m	Gradient fidelity	1.6 ±0.3 mm
Gradient maximal slew rate	120 mT/m/s	Ghosting [EPI]	0.3 ±0 %
RF maximal frequency offset	305 kHz	Absolute field strength	63.88 MHz ±2.2 kHz

In connection with this a static couch was introduced into the system, fixed in the superior-anterior and left-right direction within the bore. On the newly developed LINAC system all electrical and technical components are positioned on a helical gantry rotating outside of the RF-cage and via active shielding barely influenced by the static magnetic field (cf. figure 6). Due to the additional space needed for the MRI, the photon source is, in comparison to conventional linacs, shifted to a greater distance of 143.5 cm to the isocenter. The accelerator system was simplified to a standing wave guide with a single photon energy of 7 MeV.

1.2.5.2 Influence on charged particles

Whereas the uncharged photons are not influenced by the magnetic field, charged secondary particles are. Depending on their electric charge and magnitude of the static magnetic field the charged particles are experiencing the Lorentz force:

$$F_L = q \cdot (\overrightarrow{v} \times \overrightarrow{B}). \tag{9}$$

Therefore electrons are forced on helices of different radii based on the vector product of velocity and magnetic flux density. By extending equation (9) with the centripetal force the helical radius, known as larmor-radius, with which the electrons are rotating, is calculated as follows:

$$r = \frac{m \cdot v_{\perp}}{|q| \cdot B} \tag{10}$$

Electrons at a kinetic energy up to 7 MeV are travelling nearly with the speed of light. If this is taken into account the larmor-radius for generated secondary electrons at the 1.5 T MR-linac can be derived, dependent on their energy and angle with respect to the static magnetic field lines, as shown in Figure 8 (A). In this Figure the larmor radii are shown, in relation to the photon spectrum of the 1.5 T MR-linac. For this calculation the approximation that generated secondary electrons are experiencing the same kinetic energy as their prior photon was employed.

Due to the Lorentz force the electrons experience a change of trajectory, resulting in shifted dose distribution profiles in orientations perpendicular to the magnetic field (cf. figure 7).

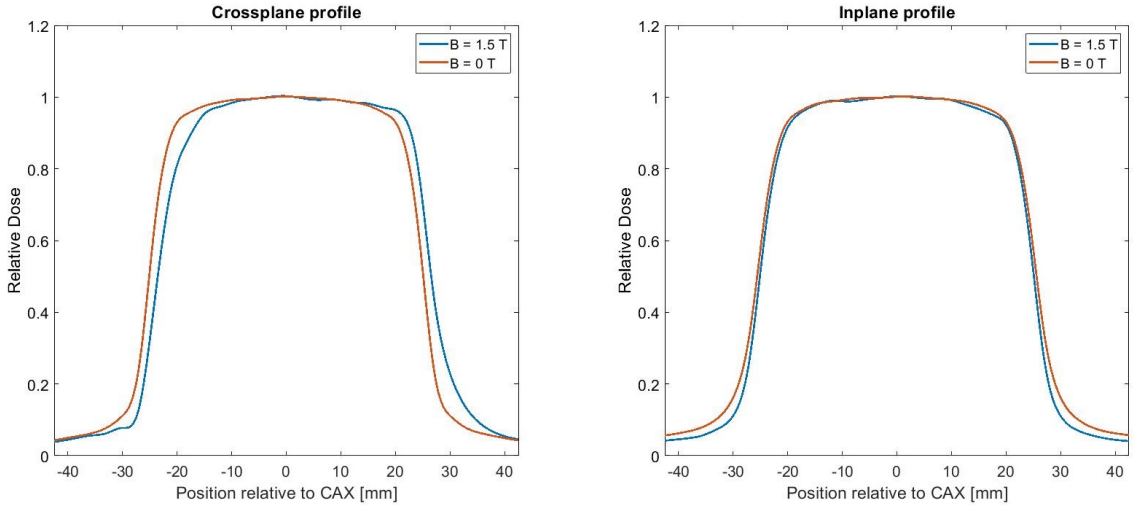

Figure 7: Shown is the magnetic field effect on a relative dose distribution, simulated along the central orientations at the isocenter level for a $5cm \times 5cm$ field irradiated from an angle $= 0$ $^\circ$. Depicted in blue is the true dose distribution at 1.5 Tesla and in red the corresponding dose distribution without the magnetic field effect. The crossplane profile denotes the orientation perpendicular to the magnetic field, whereas the inplane profile denotes the orientation along the magnetic field lines, which is not directly influenced by the Lorentz force. The position on the axis is shown in relation to the central axis (CAX).

Whereas secondary generated electrons have a maximum path length at $E_{max} = 7$ MeV in water of approximately 3.5 cm, the influence of the Lorentz force is greater in low density tissue or air. Within these circumstances the Lorentz force can cause an electron return effect (ERE) or electron stream effect (ESE) (cf. Figure 8 (B-C)). These two effects are both depending on the helical radius of the electrons, which depend on the velocity of the electrons and their angle to the magnetic field lines orientation (cf. figure 8 (A)). However they do materialize themselves differently.

The ERE denominates the effect, which occurs when electrons are exiting the surface of a patient anatomy and based on their radius are capable to return back to the surface of prior exit. Therefore the ERE leads to an increase of dose on interfaces between tissues of different densities, which however is dependent on the energy of the secondary electron, the density interface and the angle of exit. The electron stream effect (ESE) denotes the effect in which the helical trajectory of electrons does result in a low dose deposition on an anatomical point away from the primary ejection point. For anatomies like breast, in which electrons can travel in a free direction, since the breast is not surrounded by anatomical parts, electrons are streamlined along the magnetic field lines and deposit their combined low dose as soon as sudden tissue appears. As consequence this effect shows small dose effects in anatomical parts away from the target, if no additional material is in the way.

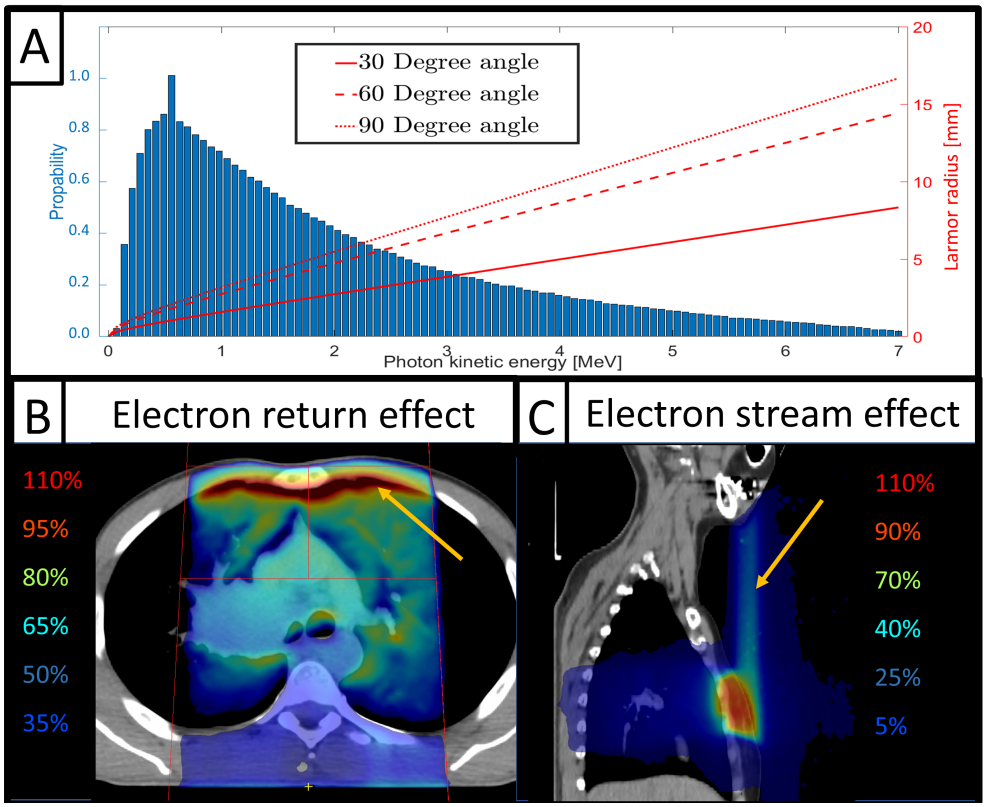

Figure 8: Shown in (A) is the energy distribution at the MR-linac system of primary photons as they enter the bore. In correspondence shown is the larmor radii of electrons at the respective energy in dependence of their angle to the magnetic field lines. In (B) shown is a visual representation of the electron return effect (ERE) is for an esophageal carcinoma. In contrast shown in (C) is the low dose deposition in regards to the electron stream effect (ESE) for a breast patient.The respective effects are highlighted within the figures by an orange arrow.

1.2.5.3 Adaptive Workflow

MRgRT is primarily developed for a daily adaptation of the radiotherapy plan based on the anatomy of the day, while the patient is on the treatment table. Enabling this, the daily MRI is correlated to a predefined reference setting and dose distribution. Based on similarities between the reference and daily image different workflows can be executed. In an adapt to position (ATP) workflow, the daily online anatomical image offers a great representation of a prior reference setup, for which a dose distribution was already ideally optimized. Therefore no necessity to optimize a new plan is present and the optimized plan only needs to be adapted to the daily patient position. Consequently in this workflow only the positional difference to the reference is calculated, the MLC and diaphragm positions are geometrically adapted in regard to the daily position and a simplified warm start optimization is executed [6]. Therefore, this simpler workflow is less time consuming and allows faster patient

treatments. However, if daily anatomical changes in contrast to the prior generated plans are present, a new optimization of dose distribution on the changed anatomy is necessary. In this adapt to shape (ATS) workflow the online MRI is annotated and a plan is optimized without a interruption of the daily patient treatment. Due to scaling of intrafraction motion with treatment times, fast workflow steps including semi-automatic deformable annotation, robust optimization parameters and greater dose calculation uncertainties are employed.

1.2.5.4 Potentials and limitations

MR-guided radiotherapy (MRgRT) enables, thanks to the detailed technical background elaborated, a multitude of new opportunities. Higher soft tissue contrast allows a better differentiation between tumor and surrounding soft tissue. In combination with possible fat suppression or different MRI contrasts, this increased differentiation might result in higher accuracy for target definition and more detailed allocation of tumor volume. Better differentiation should as well reduce the variability of tumor definition between observers and therefore consequently reduce safety margins. Respective safety margins could as well be reduced, as uncertainties in the daily target position (inter-fraction movement) are accounted for by plan adaptation on the daily anatomy. Live imaging during treatment in 2D and 3D in addition opens the door to the treatment of moving tumors due to respiratory motion using a gated workflow, minimizing healthy tissue irradiation. Such online MRgRT is possible due to dose-free three dimensional high quality images, which can be executed multiple times during treatment. Online re-planning does account not only for the variation of daily target positions but also for its deformation during the course of treatment.

Adaptive re-planning additionally allows for daily sparing of OARs, and defining their exact respective daily dose. Accurate daily dose identification and accumulation over the treatment course allows for a first correct correlation of applied dose to responses, as all currently derived probabilities are based on approximations. Secondly the biological correlation of complication and tumor control can be incorporated into planning and employed as thresholds during therapy.

Functional imaging in MRI, primarily diffusion weighted imaging (DWI) and dynamic contrast-enhanced imaging (DCE) has already shown to correlate to tumor response and to normal tissue toxicity [160]. Adding these information's into radiotherapy planning prescriptions might allow the identification of tumor resistant or sensitive

areas and consequently allowing a functional information derived additional dose or sparing of tissue.

However, these possibilities are accompanied by challenges arising due to the magnetic field. Whereas the MRIs show great potential, the physical background does exhibit challenges in contrast to the conventional X-Ray imaging. Due to the interaction with nucleons and not electrons, the information measured from the MRI can not be used for the simulation of dose distributions and based on the reconstructions the detected anatomical information is prone to spatial distortion and in consequence not as accurate.

Whereas this geometric accuracy is not a necessity in diagnostics, in radiotherapy it is crucial in order to avoid the possibility of under treatment of tumor and consequently reduced control. Geometric distortion may arise because of scanner specific limitations, density gradients, respiratory influenced areas or patient induced inhomogeneity.

Another limiting factor of the treatment with an MR-linac system is the confined patient selection. It is limited as the time needed for an MRI is greater then for a CT, the bore dimension is smaller and auditory noises add an additional patient burden. Moreover, patient selection is limited by the presence of pacemakers, implants and ferromagnetic material in general due to patient safety and geometrical distortion.

From a dosimetric point of view, the static magnetic field does not only influence ferromagnetic materials, but in addition changes the trajectory path of secondary generated electrons and consequently modify the dose distribution. Modeling of this effect, as well as additional dosages to healthy tissue due to ERE and ESE must be accounted for. Additional limitations occur since the inclusion of MRI into a hybrid MR-linac system results in linacs and MRIs which are not comparable on their respective technological parameters to modern state of the art systems.

Technical limitations occur next to the hybrid MR-linac system on all used equipment in radiotherapy, which, so far, was not designed to work in a magnetic field. Therefore additional systems must be developed for the quality assurance of MR-linac systems, in which different objectives to the so far used systems are of importance. Consequently quality assurance of online adaptive workflows, which so far were never possible, need to be developed as well. These workflows incorporate offline checks, which have routinely by executed in hours, to be accounted for in a matter of minutes as in this setting, additional time results in intrafraction motion and consequently in a valueless online adaptive workflows.

1.3 Aims and objectives

The aim of this thesis was to investigate the emerging challenges for the clinical usage of adaptive MR-guided radiotherapy (MRgRT). For this, the disadvantages of the system in comparison to modern state of the art radiotherapy must be analyzed. The charged particle interaction due to the magnetic field and the influence of the trajectory trough cryostat must be investigated prior to patient treatment. For the treatment in an online adaptive workflow offline and online quality assurances needed to be developed. Consequently high precision treatment of patients of different entities should be established with the developed workflows based on the prior derived knowledge and analyzed towards the additional value of MRgRT.

The first objective of this thesis was to determine and characterize the technical limitations of the system for the irradiation of patients. The MR-linac system is limited on its technical parameters in comparison to state of the art linear accelerators (LINAC). Main photon fluence defining components, such as MLC are inhibiting a 44% greater width at isocenter level, limiting the sharp edges of segments, and the modulation technique is limited to a static (Step and shoot) instead of dynamic (VMAT) IMRT, decreasing the number of freedoms within an optimization. Additional drawbacks consist of a fixed isocenter position and therefore the use of less optimal, off-isocenter segments, limitation of certain beam entrance angles, flattening filter free profiles, additional scatter of the cryostate and the magnetic field effect on the dose distribution.

A second objective consisted of developing a Monte Carlo (MC) model for accurate simulation of radiation dose in the presence of the magnetic field. So far only a single commercial GPU-oriented Monte Carlo dose calculation platform (GPUMCD) [75] could calculate a dose distribution for the 1.5 Tesla MR-linac system. This GPUMCD however, has only been verified by experimental simple measurements in water and not by a detailed independent system. Thanks to prior information to the related Voxel Monte Carlo (XVMC) code and its application, it is known that fast MC-algorithms are working on approximations, simplifying most of the accelerator head model and systemically suppressing stopping radiation generated by secondary electrons. Whereas the effects of this were known in the conventional system, the influence of the magnetic field and the irradiation trough a cryostat has not been investigated. Therefore the second objective of this thesis was to develop a full accelerator head model, simulating all interactions of particles, including all components of the treatment head and the trajectory trough cryostat. With this

independently build accelerator head model, dose distributions should be compared to the GPUMCD code verifying the calculation algorithm in a patient specific system.

A further objective was to develop a quality assurance workflow for the experimental verification of deposited radiation dose from optimized patient treatments. Due to the magnetic field, conventional electrical components are either not usable or show a high magnetic field influence for the measurement of dose distributions in comparison to their conventional calibration. In this objective, the influence of the magnetic field on two dimensional ionization chamber arrays must be investigated and characterized. Based on this characterization, a workflow needed to be developed for the acquisition of correct experimental data.

A fourth objective was to develop a system for quality assurance during adaptive patient treatments. During online adaptive MRgRT, a new set of treatment plan parameters is derived, while the patient is on the table. This daily optimization specifies, based on online annotations of target and OAR, new machine parameters, which can substantially differ between different days of treatment. To assure, that these machine parameters are not incorrect and therefore result in a inaccurate treatment, it is necessary to independently assess the dose distribution in a secondary system. Therefore, a framework needed to be developed, in which the new parameters can be rapidly validated, before the irradiation of patients assuring safe online adaptive MRgRT.

Finally, patients of different entities must be irradiated at the MR-linac system. Additional knowledge derived from the prior studies must be incorporated into the treatment planing and definition of machine parameters to assure safe and best possible patient irradiation. For different entities, the usage of different workflows, needs to be exploited with their corresponding potential and the magnetic field effects (ERE/ESE) investigated and validated in a clinical setting. In addition, experimental data for the magnetic field specific effects must be measured and compared to their respective simulated data.

2 Results and discussion

2.1 Comparison of treatment plans for a high-field MRI-linac and a conventional linac for esophageal cancer

Authors : **Marcel Nachbar**, David Mönnich, Paul Kalwa, Daniel Zips, Daniela Thorwarth, Cihan Gani

Published in: Strahlentherapie und Onkologie 2019 Vol. 195 Issue 4 Pages 327-33

DOI: 10.1007/s00066-018-1386-z

The research was carried out in accordance the approved statement by the local ethics board (408/2018B02).

2.1.1 Abstract

Purpose: To compare radiotherapy treatments plans in esophageal cancer calculated for a high-field magnetic resonance imaging (MRI)-linac with plans for a conventional linac.

Materials and methods: Ten patients with esophageal squamous cell carcinomas were re-planned retrospectively using the research version of Monaco (V 5.19.03, Elekta AB, Stockholm, Sweden). Intensity modulated radiotherapy (IMRT) plans with a nine-field step-and-shoot technique and two-arc volumetric modulated arc therapy (VMAT) plans were created for the Elekta MRI-linac and a conventional linac, respectively. The prescribed dose was 60 Gy to the primary tumor (PTV_{60}) and 50 Gy to elective volumes (PTV_{50}). Plans were optimized for optimal coverage of the 60 Gy volume and compared using dose–volume histogram parameters.

Results: All calculated treatment plans met predefined criteria for target volume coverage and organs at risk dose both for MRI-linac and conventional linac. Plans for the MRI-linac had a lower number of segments and monitor units. No significant differences between both plans were seen in terms of V_{20Gy} of the lungs and V_{40Gy} of the heart with slightly higher mean doses to the heart (14.0 Gy vs. 12.5 Gy) and lungs (12.8 Gy vs. 12.2 Gy).

Conclusion: Applying conventional target volume and margin concepts as well as dose-fractionation prescription reveals clinically acceptable dose distributions using hybrid MRI-linac in its current configuration compared to standard IMRT/VMAT. This represents an important prerequisite for future studies to investigate the clinical benefit of MRI-guided radiotherapy exploiting the conceptional advantages such as reduced margins, plan adaptation and biological individualization and hypofractionation.

2.1.2 Zusammenfassung

Zielsetzung: Ziel der gegenwärtigen Arbeit ist es, Hochfeld Magnetresonanztomographie (MRT-)-Linac Bestrahlungspläne zur Behandlung von Ösophaguskarzinomen mit Plänen, die für einen konventionellen Linearbeschleuniger berechnet wurden, zu vergleichen.
Material und Methoden: Für 10 Patienten mit einem Plattenepithelkarzinom des Ösophagus wurde retrospektiv eine Replanung mit der Forschungsversion von „Monaco“ (V 5.19.03, Elekta AB, Stockholm, Schweden) durchgeführt. Intensitätsmodulierte Bestrahlungs(IMRT)-Pläne in einer Neun-Felder-step-and-shoot-Technik und volumenmodulierte Arc-Therapie(VMAT)-Pläne mit zwei Bögen wurden jeweils für den Elekta-MRT-Linac und für einen konventionellen Linac erstellt. Die verschriebene Dosis betrug 60 Gy für den Primärtumor (PTV_{60}) und 50 Gy für elektiv nodale Areale (PTV_{50}). Die Pläne wurden auf eine optimale Erfassung des 60-Gy-Volumens hin optimiert und über Dosis-Volumen-Histogrammparameter miteinander verglichen.
Ergebnisse: Alle Behandlungspläne erfüllten die vordefinierten Kriterien zur Zielvolumenabdeckung und für die Risikoorgane sowohl für den MRT-Linac als auch für den konventionellen Linac. Die Pläne für den MRT-Linac wiesen eine niedrigere Anzahl von Segmenten und Monitoreinheiten auf. Keine signifikanten Unterschiede zwischen den Plänen wurden in Bezug auf die V_{20Gy} der Lunge und die V_{40Gy} des Herzens gesehen, mit leicht höheren mittleren Herz- (14,0 Gy vs. 12,5 Gy) und Lungendosen (12,8 Gy vs. 12,2 Gy).
Schlussfolgerung: Unter Anwendung konventioneller Zielvolumenkonzepte, Sicherheitssäume und Dosisfraktionierungskonzepte zeigen sich klinisch akzeptable Dosisverteilungen für den MRT-Linac in seiner aktuellen Konfiguration im Vergleich zur Standard-IMRT/VMAT. Dies stellt eine wichtige Voraussetzung für zukünftige Studien dar, die den klinischen Nutzen der MRT-gestützten Strahlentherapie untersuchen und die konzeptionellen Vorteile, wie verminderte Sicherheitssäume, Adaptationen, biologische Individualisierungen sowie Hypofraktionierung, implementieren.

2.1.3 Introduction

Radiotherapy of esophageal cancer is challenging due to the poor visualization of intraluminal tumors on computed tomography (CT) imaging, resulting in geographic uncertainties and therefore large margins during treatment planning. This inevitably is associated with increased doses to organs at risk such as the heart and lungs, which is particularly critical in patients presenting with limited cardiac and pulmonary function due to predisposing factors often seen in patients with esophageal cancer. The concept of hybrid devices combining a linear accelerator (linac) and magnetic resonance imaging (MRI) is a door-opener to innovative, more effective and less toxic treatments in radiation oncology. In terms of esophageal cancer, MRI-guided radiotherapy with superior tumor visualization on a daily basis may decrease the likelihood of geographical misses and allow smaller margins and daily adapted treatment, resulting in lower doses to organs at risk [129]. Furthermore, functional imaging data, such as diffusion weighted imaging (DWI), acquired on the MRI-linac, may be used as a predictive imaging biomarker for treatment response [158]. The combination of an MRI with a linear accelerator as realized in the Elekta high-field MRI-linac (Elekta AB, Stockholm, Sweden) with the MRI component placed within the linac gantry, brings about relevant technical differences with possible implications for treatment plan quality compared to a standard linear accelerator. The most important differences that may influence treatment plan quality are a larger source to isocenter distance, the interaction of secondary electrons with the magnetic field and limited possibilities for patient positioning in the MRI bore [100, 146, 205]. Therefore, the goal of the present study was to investigate whether similar treatment plan quality can be achieved for the MRI-linac compared to a standard linear accelerator for esophageal cancer.

2.1.4 Methods

2.1.4.1 Patients

Twelve consecutive patients (6 male, 6 female) with thoracic esophageal squamous cell carcinoma were identified retrospectively from our institutional database. Six patients were node positive; the primary tumor was staged T3 in all but two cases, which were found to be T2 and T4, respectively. Median length of the primary tumor was 4 cm (range 2–10 cm).

2.1.4.2 Target volume and organ at risk definition

For the purpose of this planning study all target volumes were re-contoured by a single investigator (CG) following a consensus recommendation by Wu et al. [202]. Briefly, the gross tumor volume (GTV) was delineated on a planning CT with 3 mm slice thickness using information from endoscopic and positron emission tomography (PET) studies wherever available. For generation of clinical target volume (CTV_{50}) intended to receive a dose of 50 Gy, a radial margin of 1 cm was added and extended to cover mediastinal and para-esophageal lymph nodes. Cranio-caudally, a margin of 4.2 cm was added in each direction. In case of positive lymph nodes above or below this margin the CTV_{50} was extended 12 mm above or below the given lymph node. For planning target volume (PTV) a 9 mm margin was added isotropically to generate the PTV_{50}. A 10 Gy percutaneous boost to the primary tumor was planned by adding a 9 mm margin to the CTV60, which covered the GTV and the adjacent 12 mm of the esophagus, resulting in the PTV_{60}. Both PTV_{50} and PTV_{60} were planned in fractions of 2 Gy. Normal tissues were contoured according to the RTOG lung atlas (https://www.rtog.org/CoreLab/ContouringAtlases/LungAtlas.aspx). Skin as an organ at risk was defined as the tissue covering 5 mm inside the patient contour. To evaluate the isolated electron return effect (ERE), we analyzed, next to the skin dose, which is not only influenced by the ERE but as well by the shorter dose build-up at air-tissue interfaces, a lung fringe, defined as the first 3 mm within the lung tissue [34, 159].

2.1.4.3 Treatment planning

Treatment plans for a standard linac as well as for an MRIlinac were created with Monaco Research Version 5.19.03 (Elekta AB, Stockholm, Sweden) using constrained optimization and Monte Carlo dose calculation. In the research version of the treatment planning system (TPS), MRI-linac specific treatment plans can be created, including the influence of the magnetic field, the MRI cryostat and a linac beam model. The plans also account for the MRI-linac specific couch, receiver coil and an isocenter fixed in a height of 13 cm above the couch. Additional specifications for treatment planning are given in table 2. Both plans were calculated in Monaco with the TPS parametergiven in Table 2. The step-and-shoot plans were limited to a maximum of 250 segments, whereas the volumetric modulated arc therapy (VMAT) plans were limited to a maximum of 360 control points and 2 arcs. For the MRI-linac, step-and-shoot treatment plans with nine beam angles

were created. Optimum beam angles were automatically obtained by analyzing the angular distribution of monitor units of VMAT plans with two arcs optimized for the MRI-linac.

Table 2: Device specific differences and treatment planning system (TPS) parameters for the MRI-linac and a standard linac

Device specific parametersr	**MRI-linac**	**Standard linac**
Distance focus-IC (cm)	143.5	100
Leaf width at IC (mm)	7.2	5
Field size at IC (cm)	22× 56	40× 40
Leaf travel direction	Cranio-caudal	Arbitrary
IMRT technique	Step-and-shoot	VMAT
Photon energy (MeV)	7	6
Flattening filter	FFF	FF
IC position	MRI isocenter	Center of PTV_{60}
Static magnetic field (T)	1.5	–
TPS parameter		
Calculation grid (cm^3)	0.3 × 0.3 × 0.3	0.3 × 0.3 × 0.3
Calculation uncertainty	1%	1%
Calculation algorithm	GPUMCD	XVMC
Segments/Arcs allowed	250/–	360/2

IC isocenter, TPS treatment planning system, IMRT intensitymodulated radiotherapy, VMAT volumetric modulated arc therapy,FFF flattening filter free, FF flattening filter

For this analysis the angular distribution of monitor units was pre-processed by applying a Gaussian filtering to account for sudden drop offs in the monitor unit distribution, as well as to combine the dose distributions from both arcs (Figure 9 a). To identify the optimal beam angles, we then searched for the local maxima within the angular distribution and generated artificial angles if the angle difference between two local maxima surpasses a threshold (Figure 9 b). After this pre-processing, depending on the desired number of beam angles, a weighted averaging between two adjacent local maxima is applied if the distance between them is too small. Afterwards an iterative rank scoring was initialized for which every angle was ranked depending on its relative number of MUs and distance to the next adjacent beams. For every iteration the angle with the smallest scoring gets eliminated until the intended number of beams is achieved (Figure 9 c). All plans were optimized for

optimal target coverage of PTV_{60} with a comparable mean dose for all patients. If a target volume associated criterion could not be met, the dose constraints for individual OARs were relaxed starting with OARs with the highest impact on target coverage and still meeting the dose constraints. The predefined dose constraints for OARs are shown in Table 3. To improve comparability, MRI-linac and corresponding standard linac plans were rescaled after optimization to achieve a mean dose of exactly 60 Gy in PTV_{60}, which cannot be achieved with the TPS. Conformality was evaluated by the ratio of target volume and volume receiving more than 95% of the prescribed dose

$$CI = \frac{TV}{V_{95\%}}$$

The evaluated dose homogeneity index HI is defined as follows:

$$HI = \frac{(D_{2\%} - D_{98\%})}{D_p} \times 100\%$$

Dp denotes the prescribed dose for the evaluated target volume.

Differences between dose-volume histogram (DVH) parameters in MRI-linac and standard linac plans were analyzed with a Wilcoxon signed rank test in R 3.4.3. The retrospective assessment of patient related data was approved by the local ethics committee.

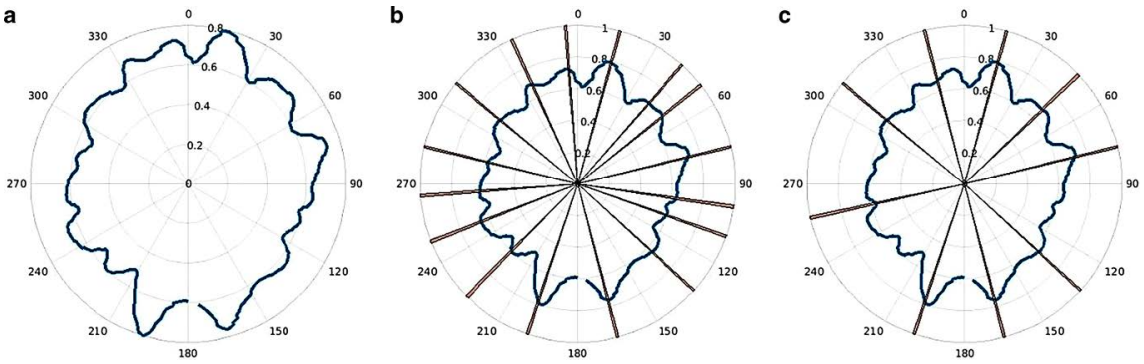

Figure 9: Workflow of the beam angle optimization from left to right: Starting with the Gaussian filtered angular distribution of monitor units of optimized volumetric modulated arc therapy (VMAT) plans (a), pre-processing of local maxima (b) and the calculated optimized beam angles (c)

2.1.5 Results

2.1.5.1 Treatment plan characteristics

The maximum allowed number of segments was neither reached for the MRI-linac nor the standard linac. For the MRI-linac only 3 of 20 plans (10 initial/10 boost) exceeded 100 segments. The mean number of segments for the MRIlinac was 87 with a mean of 600 monitor units (MU) per fraction. For the standard linac the mean number of segments was 215 with 665 mean MU per fraction.The beam angle optimization for the MRI-linac resulted in an angle distribution with an average median angle distance between two adjacent beams of 36.4°± 2.8°, which is similar to equidistant beam angles with a distance of 40°. A plan comparison between nine equidistant and nine individualized beam angles for all 10 patients showed a higher conformity and marginally better OAR sparing for individualized beam angles (Supplementary material: Figure S1).

2.1.5.2 Feasibility of treatment plans for the MRI-linac

For ten of the twelve target volumes a treatment plan could be calculated. The mean longitudinal extension of the PTV_{50} in these ten cases was 15.1 cm (range 12.7–19.5 cm). The remaining two cases had a longitudinal extension of 22.0 cm and 22.6 cm, respectively, exceeding the maximum superior-inferior field size of 22 cm of the MRI-linac. Plan realization of these two target volumes would have been possible with a single isocenter at the conventional linac. For both devices all predefined constraints regarding organs at risk were met. Constraints regarding the target coverage were met as well in all cases. However, after rescaling the dose distribution to compare treatment plans for both devices, the GTV "minimal dose constraint" no longer met the required criterion for one patient at the standard linac (56.985 Gy) and for two patients at the MRIlinac (56.965 Gy / 56.405 Gy). The mean rescaling factor for the MRI-linac was 0.1%, whereas the mean rescaling factor for the standard linac was –0.3%. A Wilcoxon singed rank test comparing the rescaling factors showed no significance (p= 0.11). Therefore, the rescaling was moderate and not systematic with respect to one modality.

2.1.5.3 Comparison of treatment plans for a standard linac and the MRI-linac

Regarding target volume related parameters no significant differences were found for $D_{98\%}$ and $D_{2\%}$, neither for PTV_{60} nor for PTV_{50}. Conformality was significantly higher for VMAT plans than for the MRI-linac with respect to PTV_{60} (0.71 vs. 0.57, p= 0.004) and PTV_{50} (0.70 vs. 0.60, p= 0.002). The difference in conformality between the devices is illustrated for an exemplary case in Figure 10. The homogeneity index for the PTV_{60} showed no significant difference between the devices (6.8% vs 6.3% p= 0.28). With respect to the normal tissues, significantly higher values were observed for the MRI-linac for the mean lung dose (12.8 Gy vs. 12.2 Gy, p= 0.006). Similarly, mean heart doses (MHD) (14.0 Gy vs. 12.5 Gy, p= 0.002) and maximal spinal cord dose were higher in plans optimized for the MRI-linac (40.3 Gy vs. 39.1 Gy p= 0.027). All evaluated skin related parameters were significantly higher in the MRI-Linac plans with Dmean 4.16 Gy vs. 3.14 Gy, p= 0.002, D_{max} 45.9Gy vs. 41.3, p= 0.002 and skin $D_{2\%}$ 25.7 Gy vs 20.0 Gy, p= 0.002.

Table 3: Dose constraints for organs at risk

Structure	DVH restriction
PTV Boost	$D_{98\%}$> 90% (54 Gy)
	$D_{2\%}$< 107% (64.2 Gy)
PTV	$D_{98\%}$> 90% (45 Gy)
GTV	D_{max}< 110% (66 Gy)
	D_{min}> 95% (57 Gy)
Total lung	V_{5Gy}< 70%
	V_{10Gy}< 55%
	V_{20Gy}< 35%
	D_{mean}<20Gy
Heart	D_{mean}<31 Gy
Spinal cord	D_{max}< 48 Gy
	$D_{2\%}$<45 Gy
LAD	Dmean<30 Gy

OAR organs at risk, PTV planning target volume, GTV gross tumor volume, LAD left anterior descending artery

Figure 11 depicts the differences in terms of DVH parameters between the MRI-linac and the conventional linac. The analyses of the lung fringe showed an increase in mean dose for the MRI-linac of in median 1.15 Gy, with a minimal increase of 0.59 Gy and a maximal increase of 2.14 Gy. This is due to the ERE, which

induces a return of electrons radiating from the tissue into the lung caused by the Lorentz force. Following the analysis of DVH parameters, we visually evaluated the subtracted dose distributions in order to identify relevant differences, which are not covered by the chosen parameters.Within this analysis we inspected the difference in dose distributions as shown in figure 10 c and 12 c. While dose deviations within the boost volume are marginal, more pronounced differences are seen outside the target volume at the cranial and caudal field margins in figure 10 c. This dose increases in structures positioned at this geographical location relative to the high dose volume. In the presented case this resulted in a higher mean dose to the adjacent larynx (6.6 Gy vs 2.6 Gy) for the MRI-linac plan.

2.1.6 Discussion

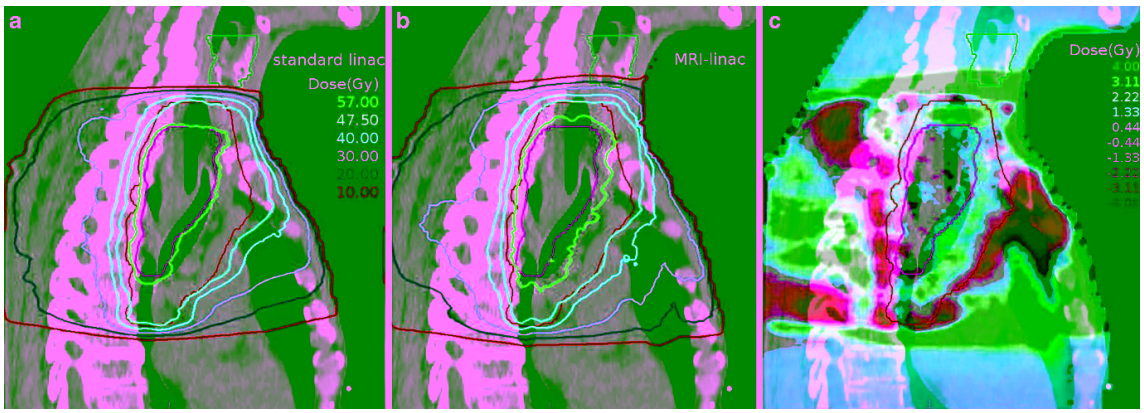

Figure 10: Sagittal views of the target volumes and dose distributions for the standard linac (a), the MRI-linac (b) and a subtraction of the dose distribution between both devices (c) MRI linac – standard linac). Colors: Light blue PTV_{60}, dark blue PTV_{50}, red larynx. Isolines represent 95% of 60 Gy (red) and 50 Gy (orange)

The present study is the first published to investigate in silico the feasibility of definitive dose escalated radiotherapy for thoracic esophageal cancer using MRI-linac technology. The MRI-linac plans were optimized without limitations of plan quality by integrating a beam angle optimization and allowing up to 250 segments, which exceeds the clinically used standard and would cohere with a long radiation time. However, the sequencer settings resulted in plans with mean numbers of segments remaining in a clinically acceptable timeframe, depending on the device performance.

We were able to show that in all plans for the MRI-linac DVH constraints were met. Slightly higher mean doses to the lungs in the nine beam step-and-shoot plans still remained below the steep increase in dose-response curves for radiation pneumonitis

which does take place beyond a mean lung dose of 15 Gy [202]. Regarding cardiac toxicity, it should be noted that valid normal tissue complication probability models for cardiac toxicity after radiotherapy of esophageal cancer have not been established yet [22]. The vast majority of the data underlying dose constraint recommendation are derived from patients treated with radiotherapy for lymphoma breast cancer, diseases which in general have a better prognosis than esophageal cancer or lung cancer [135]. For the latter a recent pooled analysis came to the conclusion that the mean heart dose should be kept below 20 Gy in order to limit the risk for cardiac events, as it is clearly the case for both techniques in our trial [191]. Furthermore, in our study plans were optimized using a constraint to keep the mean heart dose below 31 Gy, which is far higher than the doses that were actually achieved. It therefore appears likely that with a stricter prescription equal heart doses between the two techniques can be achieved. This stricter prescription to achieve an equal heart dose will result in a trade-off to another OAR (in most cases lung), or target coverage, which must be decided by the treating physician considering factors such as pre-existing diseases or baseline pulmonary function.

While the MRIlinac in its first clinical version will support only step-andshoot as IMRT technique, VMAT implementation is currently under development. As expected and previously reported, skin doses are higher at MRI-linac, possibly due to electron return effects [66, 69, 120]. Despite the unique physical (B-field) and geometrical properties (leaf width, focus-skin distance, etc.) of the MRI-linac, our observations in terms of differences between VMAT and step-and-shoot plans are in line with published literature showing higher conformality and superior organ at risk sparing of VMAT at the expense of an increased low dose irradiation volume [206, 208]. The higher OAR and skin dose for the MRI-linac might be the consequence of MRI cryostat scatter and a larger penumbra resulting from increased source to isocenter distance and effectively wider MLC leafs compared to a standard linac. The maximum field size of the MRI-linac is limited to 22 cm in the superior-inferior direction. In our cohort ten of twelve target volumes (83%) showed target volume extensions suitable for the MRI-linac, comparable with a study by Chuter et al. who found that 84% of esophageal cancer plans from their registry were suitable for the MRIlinac [37]. In their study, more than 95% of patients with prostate, rectal, lung or brain tumor could have been treated using the MRI-linac. The lowest percentage was seen for extremity sarcomas (22 %) and cancers of the uterine cervix (61%) [37].

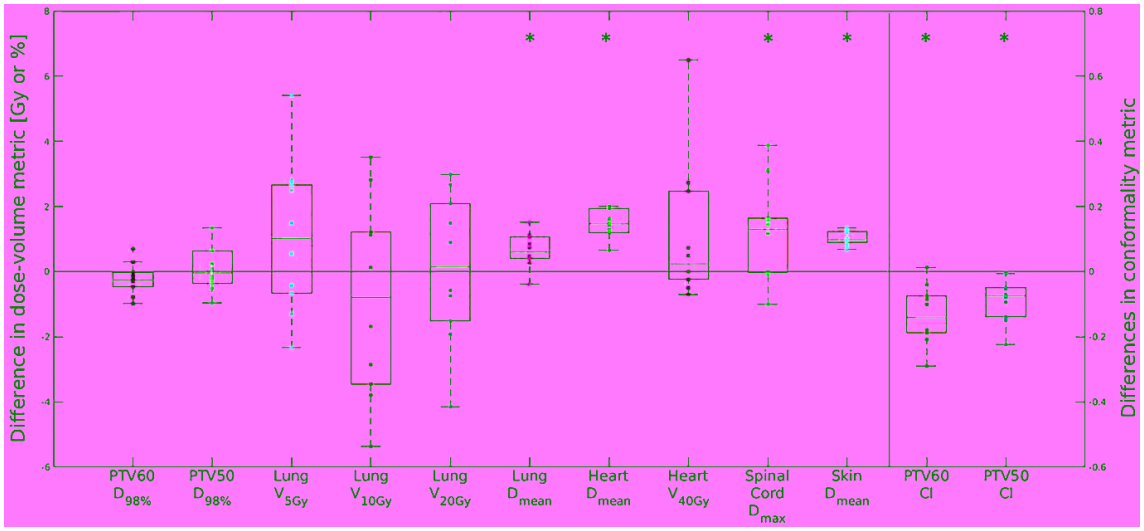

Figure 11: Differences between the plans generated for the standard linac and the MRI-linac. Positive differences mark an increase in the respective metric for the MRI-linac plans. The evaluated parameters showing a significant difference ($p < 0.05$) are marked

An unexpected finding while evaluating the geographical dose difference between the two devices was seen at the superior and inferior edges of the target volume resulting in higher doses in a region of approximately 2–3 cm with the MRI-linac. This observation is possibly associated with the increased source to isocenter distance and consequently a different divergence of the photon beams. This results in larger beam profiles for the MRI-linac in front of and smaller beam profiles behind the isocenter. Since we were able to show that clinically acceptable plans can be created for the MR-linac in its current configuration the subsequent step will be to evolve innovative treatment strategies exploiting the MR component of the hybrid device. The most obvious of such strategies is margin reduction enabled by the improved soft-tissue contrast and therefore less uncertainty regarding tumor extent.While this alone can already result in a less toxic but equally effective treatment, the reduced doses to normal tissues could also allow isotoxic dose escalation to the target volume.

This approach has recently been investigated by Bainbridge et al. in a set of locally advanced lung cancer patients. The authors assumed that the MRI-linac would permit margin reduction from 7 to 3 mm. The mean escalated isotoxic dose to the target volume with reduced margins was 81.2 Gy compared to 79.0 Gy with standard margins at a conventional linac [14]. As lung cancer, esophageal cancer is also associated with poor local control providing a rationale for dose escalated radiotherapy [193]. Additionally, a clear dose-response relationship for radiochemotherapy in esophageal cancer has been described previously [59, 193]. Therefore, dose escalation using advanced radiation technologies is a field worth being investigated using

the MRI-linac, despite the negative INT-0123 trial, which recruited patients in the mid 1990s [123]. Besides the better anatomical imaging due to the higher soft tissue contrast a major interest in multiparametric functional imaging has emerged in radiation oncology. For instance, changes of the apparent diffusion coefficient during radiotherapy have been shown to be predictive for treatment response in a variety of malignancies, such as esophageal cancer, rectal cancer or anal cancer and might therefore be a tool to stratify patients into more or less aggressive treatments [54, 84, 158, 172, 173]. The majority of these studies have used a limited number of distinct time points during the course of radiotherapy for the—offline—assessment of these functional imaging parameters. By using a hybrid device, it will be possible to collect more imaging data "online" without the need of using a separate device and the associated logistic issues. The additional data can then be used to evaluate the dynamics of these functional imaging parameters and create improved prognostic models for the personalization of treatment. Clinical trials exploiting the potential benefits of the new technology are under way.

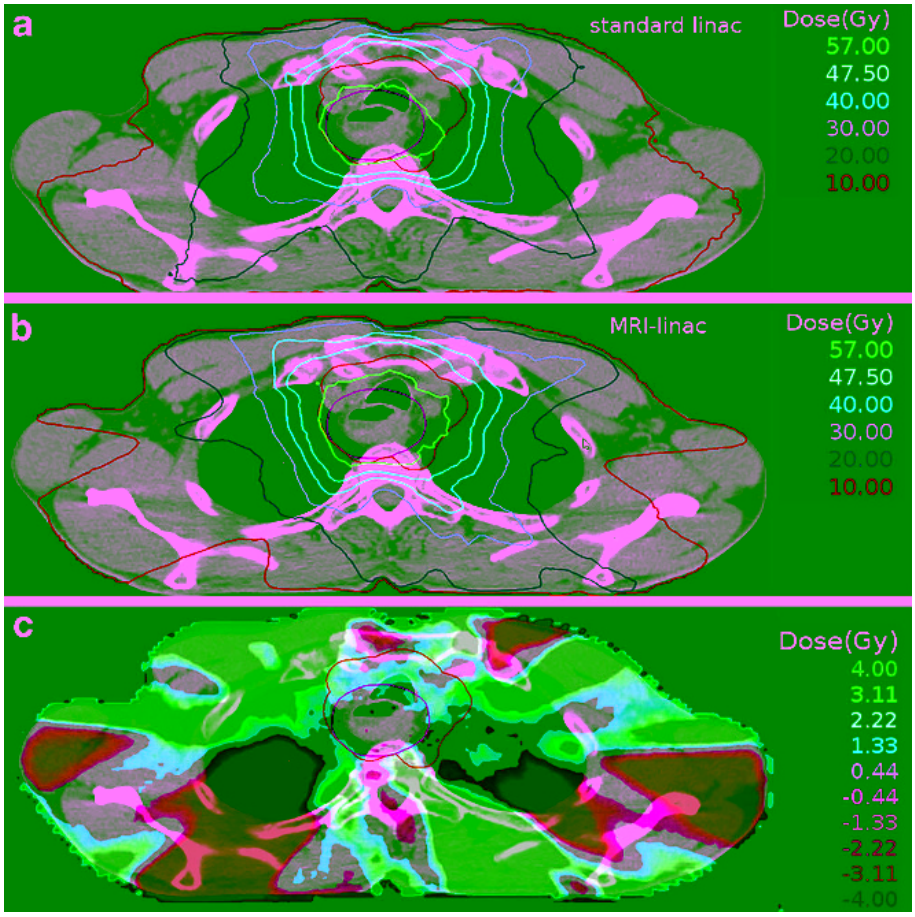

Figure 12: Transversal view of the target volumes and dose distributions for the standard linac (a), the MRI-linac (b) and a subtraction of the dose distributions (c). Colors: Light blue PTV_{60}, dark blue PTV_{50}. Isolines represent 95% of 60 Gy (red) and 50 Gy (orange). The loss of conformality can be seen by the additional margin in comparison between the isoline and their corresponding PTV structure (a,b)

2.1.7 Conclusion

Despite the technical challenges, esophageal cancer treatment plans generated for the MRI linac in its current configuration are comparable to plans for a conventional linac in terms of the predefined dose constraints. Subsequent studies will investigate the potential for biologically individualized isotoxic dose escalation and adaptive treatment individualization based on repeated multiparametric imaging.

Supplementary Material

The supplementary material of the publication is depicted in the supplementary material of the dissertation at section 9.1.

2.2 Development and validation of a 1.5 T MR-Linac full accelerator head and cryostat model for Monte Carlo dose simulations

Authors : Marina Friedel, **Marcel Nachbar**, David Mönnich, Oliver Dohm, Daniela Thorwarth

Published in: Medical Physics 2019 Vol. 46 Issue 11 Pages 5304-5313

DOI: 10.1002/mp.13829

2.2.1 Abstract

Purpose: To develop, implement and validate a full 1.5 T/7 MV MR-Linac accelerator head and cryostat model in EGSnrc for high precision dose calculations accounting for magnetic field effects that are independent from the vendor treatment planning system.
Methods: Primary electron beam parameters for the implemented model were adapted to be in accordance with measured dose profiles of the Elekta Unity (Elekta AB, Stockholm, Sweden). Parameters to be investigated were the mean electron energy as well as the gaussian radial intensity and energy distributions. Energy tuning was done comparing depth dose profiles simulated with monoenergetic beams of varying energies to measurements. The optimum radial intensity distribution was found by varying the radial FWHM and comparing simulated and measured lateral profiles. The influence of the energy distribution was investigated comparing simulated lateral and depth dose profiles with varying energy spreads to measured data. Comparison of simulations and measurements was performed by calculating average and maximum local dose deviations. The model was validated recalculating a clinical IMRT plan for the MR-Linac and comparing the resulting dose distribution with simulations from the commercial treatment planning system Monaco using the gamma criterion.
Results: Comparison of simulated and measured data showed that the optimum

initial electron beam for MR-Linac simulations was monoenergetic with an electron energy of (7.4 ± 0.2) MeV. The optimum gaussian radial intensity distribution has a FWHM of (2.2 ± 0.3) mm. Average relative deviations were smaller than 1% for all simulated profiles with optimum electron parameters, whereas the largest maximum deviation of 2.07% was found for the 22 × 22 cm^2 cross plane profile. Profiles were insensitive to energy spread variations. The IMRT plan recalculated with the final MR-Linac model with optimized initial electron beam parameters showed a gamma pass rate of 99.83 % using a gamma criterion of 3%/3mm.
Conclusions: The EGSnrc MR-Linac model developed in this study showed good accordance with measurements and was successfully used to recalculate a first full clinical IMRT treatment plan. Thus, it shows the general possibility for future secondary dose calculations of full IMRT plans with EGSnrc, which needs further detailed investigations before clinical use.

2.2.2 Introduction

In radiotherapy (RT), the balance between a high tumor control probability and a low normal tissue complication probability is crucial and determines the treatment outcome [134]. Geometrical uncertainties during radiotherapy deteriorate the treatment accuracy and thus limit the tumor dose and decrease the patients quality of life [100]. During magnetic resonance guided radiotherapy (MRgRT), these positioning uncertainties originating from imperfect patient alignment and varying tumor localization are reduced through high soft tissue contrast imaging prior to and during treatment [100, 146]. Currently, several MRgRT platforms are already in clinical use or under development [119, 138]. The 1.5 T/7 MV magnetic resonance linear accelerator (MR-Linac) Elekta Unity (Elekta AB, Stockholm, Sweden) [101] combines the advantages of a 1.5 T magnetic resonance imaging (MRI) system (Philips Oy, Vantaa, Finland) and a 7 MV standing wave linear accelerator and offers not only MRI with a high soft-tissue contrast without radiation exposure to the patient, but also online plan adaptation and functional imaging capabilities [99, 141, 199].
Because of its hybrid character, MRgRT presents technical and dosimetric challenges arising from the interplay of the MRI system and the linear accelerator, which requires beam transmission through the MRI cryostat and dose deposition within a strong magnetic field [101]. The magnetic field influences trajectories of secondary electrons generated inside the patient, which leads to a decreased dose build-up distance and asymmetric lateral dose profiles perpendicular to the magnetic field [101].

At tissue-air interfaces, the magentic field impact on dose distributions is most distinct, as the so-called electron-return effect leads to a dose peak at the interface [148]. Those effects of the magnetic field have to be taken into account in dose calculations [101].
The magnetic field influence on the MR-Linac dose deposition has already been investigated by several studies using Monte Carlo simulations [3, 147, 148, 151, 156]. Monte Carlo-based dose simulations are not only considered the gold standard for dose calculations in radiotherapy due to their high accuracy, but, despite analytical dose calculation methods being develeoped [207], they are also the suggested technique for the computation of dose distributions in the presence of a magnetic field [24]. For treatment planning and adaptation with the MR-Linac, a novel GPU-based Monte Carlo dose (GPUMCD) calculation algorithm has been developed and implemented in the Monaco treatment planning system (TPS) (Version 5.40), offering fast and accurate dose calculations in strong magnetic fields [74]. Patient-specific verification of intensity-modulated radiation therapy (IMRT) plans calculated with GPUMCD is currently either done by recalculating plans with a secondary, independent clinical dose algorithm neglecting magnetic field effects, or by measuring delivered dose distributions in a dedicated phantom [150]. Those quality assurance (QA) methods are either inaccurate or extensive and thus emphasize the need for an independent secondary offline dose calculation engine including magnetic field effects in order to verify MR-Linac treatment plans calculated by GPUMCD. First attempts have been made to evaluate GPUMCD-based dose calculations with GEANT4, using the MR-Linac photon spectrum and rectangular fields for dose calculations in a homogeneous water and heterogeneous lung-tumor phantoms [4]. For a more holistic simulation of radiation dose deposited in an MR-Linac, a full MR-Linac accelerator head model for dose recalculations of whole IMRT treatment plans calculated with Monaco in patient CTs with highly modulated beams is desirable. The aim of this study was to develop and implement a full MR-Linac accelerator head and cryostat model in the software EGSnrc. Initial electron beam parameters for the EGSnrc accelerator head model, including the mean electron energy, the energy spread and the radial intensity distribution, were adjusted to get the best agreement between measurements taken with the Elekta Unity (Elekta AB, Stockholm, Sweden) and EGSnrc simulations. The implemented accelerator head model with optimized initial electron beam parameters was compared with the vendor TPS recalculating a whole clinical prostate treatment plan.

2.2.3 Materials and Methods

2.2.3.1 BEAMnrc simulations

An accelerator head model based on construction details of the 1.5 T/7 MV Elekta Unity (Elekta AB, Stockholm, Sweden) [101] was implemented in the EGSnrc [79] user code BEAMnrc [78]. Key characteristics of the Elekta Unity are a source-isocentre distance of 143.5 cm, a multileaf collimator (MLC) with a leaf width of 7.1 mm travelling in cranial-caudal direction, and a maximum field size in the isocentre of 57.4 cm in lateral and 22 cm in cranial caudal direction [150]. The following component modules were used for the BEAMnrc model: CONS3R (Target), PYRAMIDS (Primary Collimator), CHAMBER (2x, Monitor Chamber), MIRROR (mirror), MLCE in Y direction (MLC), MLCQ in X direction (Diaphragm) and SLABS (Anti-Backscatter Plate). The MRI cryostat is modelled as part of the accelerator head using SLABS with 36 different layers. The BEAMnrc model was compiled as shared library and used as direct input for dose calculations in DOSXYZnrc with a source-isocentre distance of 143.5 cm. This method makes the generation of large phase space files redundant while allowing for efficient dose calculations with reduced uncertainty [91]. To increase efficiency, directional bremsstrahlung splitting (DBS) was applied [90, 91] with varying splitting radii adapted to the corresponding field size. No charged particle splitting was performed due to the absence of a flattening filter. Additionally, range rejection was performed everywhere except in the target. For a summary of used variance reduction parameters, refer to table 4. NRC swept beam (ISOURCE=15) was used to simulate a primary electron beam with a radial intensity and energy distribution, where both distributions were assumed to be gaussian [45, 163, 182]. Field sizes of 2×2 cm^2 and 22×22 cm^2 were simulated in order to tune initial electron beam parameters. Parameters to be adjusted were the mean electron energy, the full width at half maximum (FWHM) of the gaussian radial intensity distribution and the FWHM of the energy distribution. The 2×2 cm^2 field was simulated using monoenergetic electron beams with varying energies in the range of 6.7 - 7.7 MeV in steps of 0.1 MeV and a radial intensity spread of 0.4 mm in order to perform energy tuning. To find the optimum radial and energy distribution, the 22×22 cm^2 field was simulated with varying FWHM values for both radial and energy distribution using the optimum mean energy value found through energy tuning. The FWHM of the radial intensity distribution was varied from 0.2 - 4.0 mm, whereas the gaussian energy distribution was modiefied from 0 - 20% FWHM of the nominal mean energy.

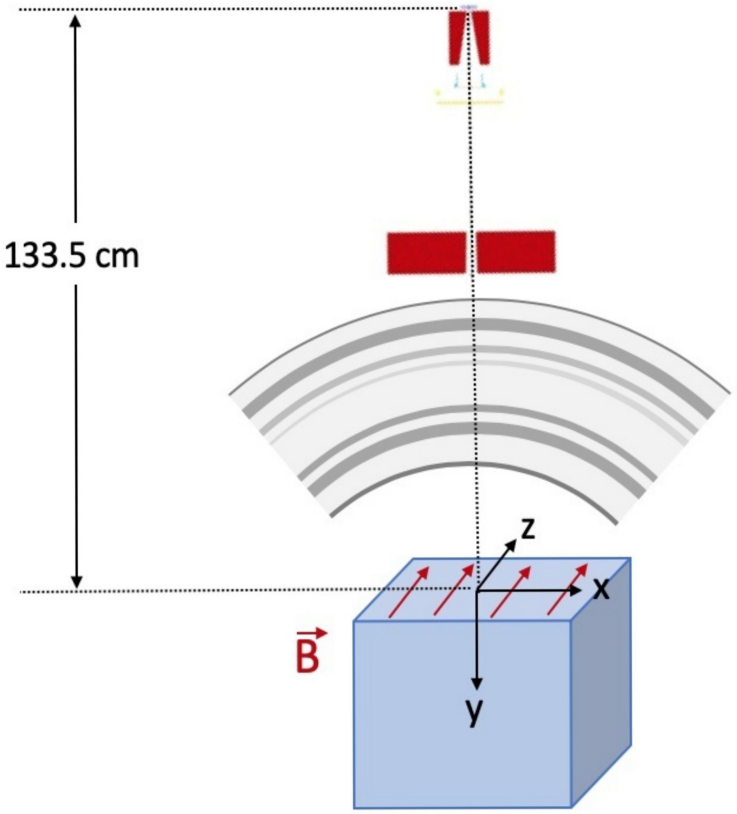

Figure 13: Schematic illustration of magnetic resonance (MR)-Linac, Cryostat, and water phantom setup as implemented in DOSXYZnrc (not to scale).

2.2.3.2 DOSXYZnrc simulations

Dose calculations for parameter tuning of the initial electron beam were performed in a voxelized water phantom implemented in the EGSnrc user code DOSXYnrc [13]. The water phantom with dimensions of $61.0 \times 23.4 \times 30.2$ cm^3 was divided into $305 \times 117 \times 151$ voxels of $2 \times 2 \times 2$ mm^3 each. A homogeneous magnetic field with a magnetic flux density of $B = 1.5$ T was included perpendicular to the beam direction. A schematic view of the DOSXYZnrc setting is shown in figure 13. Variance reduction was performed in form of charged particle range rejection and rejection of fat photons as well as photon and electron splitting [13, 91]. In total, $1.0 \cdot 10^9$ and $1.32 \cdot 10^9$ histories in 200 and 220 parallel runs were simulated for the 2×2 cm^2 and 22×22 cm^2 fields, respectively, using a high performance computing (HPC) Cluster. CPU time for each run was 2.5 - 3.5 h for the 2×2 cm^2 and 6.2 - 6.4 h for the 22×22 cm^2 field. Average uncertainties were estimated to be 0.07% and 0.40% for the small and the large field, respectively [91]. With the final MR-Linac

Table 4: Summary of variance reduction parameters used for BEAMnrc and DOSXYZnrc simulations

	Parameter	Value
BEAMnrc	ECUT	0.7 MeV
	PCUT	0.01 MeV
	NBRSPL	5000 [78]
	ESAVE	2 MeV
DOSXYZnrc	ECUT	0.7 MeV
	PCUT	0.01 MeV
	ESAVE	2 MeV
	EM ESTEPE	0.02
	n_split	40 [13, 91]
	e_split	40 [13, 91]

model, field sizes of 2×2 cm^2, 3×3 cm^2, 5×5 cm^2, 10×10 cm^2, 15×15 cm^2 and 22×22 cm^2 were simulated and corresponding output factors were calculated and compared to measurements.

2.2.3.3 Experimental Data

Experimental data was measured using the 1.5 T/7 MV Elekta Unity (Elekta AB, Stockholm, Sweden) with a source-to-surface distance (SSD) of 133.5 cm and a 1.5 T magnetic field perpendicular to the central axis of the photon beam. All measurements were made in a MR-compatible prototype motorized water phantom (Beamscan MR, PTW, Freiburg, Germany). For measurements of the 22×22 cm^2 field, an ion chamber (Semiflex 3D Type TW31021, PTW, Freiburg, Germany) with a nominal sensitive volume of 0.07 cm^3 was used. The 2×2 cm^2 field was measured using a single crystal diamond detector (microDiamond Type TW60019, PTW, Freiburg, Germany) with a very small sensitive volume of 0.004 mm^3 and thus negligible volume effects. As the magnetic field leads to a displacement of the effective monitor chamber measurement point, profiles measured with monitor chambers were shifted in order to match solid state detector readings. The detector positioning accuracy of the water scanning system was estimated to be 0.1 mm. Beams were irradiated

from a gantry angle of 0°. Depth dose profiles along the central axis as well as lateral profiles at isocentre plane in 10 cm depth were measured. Lateral profiles were measured both perpendicular (cross plane) and parallel (in plane) to the magnetic field. Data points for the depth dose profile were taken every 0.5 mm for depths up to 2 cm, every 2.0 mm for depths up to 7 cm and every 4 mm in greater depths. Data points for lateral profiles were measured every 4 mm with smaller step sizes of 2 mm in the penumbral region. The data was analyzed using Python Version 3.6.3.

2.2.3.4 Data Analysis

To examine the impact of variations in mean energy, radial distribution and energy distribution of the initial electron beam on the deposited dose, simulated and measured dose profiles were compared. Depth dose profiles were normalized to the dose value in 10 cm depth determined by fitting the fall-off region 1 cm past dose maximum with a fourth-order polynomial. Lateral profiles were normalized to an average of the three highest dose values. Simulated voxel dose values were interpolated to match measurement points. To determine an optimal initial electron energy, the simulated 2×2 cm^2 depth dose profiles were compared to measured depth dose profiles by calculating local relative dose differences in the fall off region. The maximum and average relative dose differences were determined for each simulation. To compare measured and simulated in plane profiles, which are parallel to the magnetic field and therefore not influenced by the Lorentz force, the average relative difference of measured and simulated profiles in the beam shoulder region at $\pm$ 9.5 cm was determined [162, 182]. For this purpose, dose values at + 9.5 cm and -9.5 cm were averaged for simulated and measured in plane profiles. The percentage dose difference between those mean dose values was calculated for all 22×22 cm^2 simulations. This calculated value is refered to as off-axis factor. Due to the magnetic field influence, cross plane profiles are not symmetric and the calculation of an off-axis factor is not feasible. Therefore, maximum and average local relative dose differences were determined additionally for both in and cross plane profiles in the region between $\pm$ 9.5 cm from the central axis, thus not taking into account the penumbral region, where small profile shifts lead to large local deviations. As in previous studies depth dose profiles showed insensitivity to the radial intensity distribution [35, 162], only lateral profiles were examined for radial FWHM tuning. To investigate the influence of energy spread on dose deposition, both lateral and depth dose profiles as well as the depth dose profile of the 22×22 cm^2 simulations

were examined. In addition, the gamma value was determined for each voxel of every simulation with a gamma criterion of 2 %/2 mm of the dose maximum with a pass criterion of $\gamma < 1$ [110]. The determined average and maximum relative deviations, the off-axis factor as well as the gamma values were plotted and fitted with a second order parabolic function. The minimum value of this fit function was determined for each parameter. The optimum energy and radial distribution FWHM values were chosen as an average of the minimum values, uncertainties were estimated from the respective standard deviations.

2.2.3.5 Clinical Treatment Plan Comparison

As a proof of principle, that the BEAMnrc MR-Linac model with optimized initial electron beam parameters is suitable for clinical usage, the dose distribution of a clinical treatment plan was recalculated in EGSnrc and compared to the dose calculated by the GPUMCD based treatment planning system (Monaco, Elekta AB, Stockholm, Sweden) [74]. For this purpose, a clinical treatment plan from a prostate cancer patient was exported from Monaco in DICOM format and appropriate leaf and diaphragm positions were applied in the BEAMnrc model. The recalculated prostate plan was composed of 8 beams with a total of 23 segments. For each segment, $4 \cdot 10^6$ histories were simulated in 40 parallel runs. CPU time ranged from 0.2 h to 0.6 h. The dose distribution was calculated based on a voxelized patient CT file created by the stand-alone code *ctcreate* using the default EGSnrc material conversion ramp based on four different materials (air, lung, tissue, bone) with a voxel size of $3 \times 3 \times 3$ mm^3. Variance reduction for BEAMnrc and DOSXYZnrc calculations was applied as described earlier with the exception of using uniform bremsstrahlung splitting (NBRSPL=1000) in combination with Russian Roulette in BEAMnrc simulations due to irregular field sizes. Doses of individual segments were added up voxel-wise according to the corresponding Monitor Units. MRI Helium-cryostat inhomogenieties were taken into account by applying an additional weight factor to each segment dependent on the corresponding beam gantry angle. Dose calculations with Monaco were performed using GPUMCD with a predetermined uncertainty of 1% for the entire plan. The Hounsfield unit to material density conversion ramp used by Monaco was CT-scanner specific based on one material (water) and has been defined by phantom measurements on device at hand. 3D Dose distributions obtained by Monaco and EGSnrc were compared using a gamma criterion of 3 %/3 mm of the dose maximum with a pass criterion of $\gamma < 1$.

2.2.4 Results

2.2.4.1 Energy Tuning

Table 5 shows the resulting maximum and average relative deviations between simulated and measured depth dose profiles for energies in the range of 6.7 - 7.7 MeV. The average relative error was minimal in the energy range of 7.2 - 7.4 MeV with relative deviations ranging from 0.17 % - 0.18 %. The maximum relative error was minimal for an electron energy of 7.4 MeV with a value of 0.45%. The average of the minimum values for the maximum and average relative deviations determined through a parabolic fit of the difference plots was (7.4 ± 0.2) MeV. An optimum beam energy of 7.4 MeV was therefore chosen. The maximum error for an optimum energy of 7.4 MeV was below 0.5 %, which means a good agreement could be found between measurement and calculation. The measured 2×2 cm^2 depth dose profile as well as profiles simulated in Monaco and EGSnrc using an initial electron energy of 7.4 MeV are shown in figure 14. Gamma pass rates for both Monaco and EGSnrc simulated profiles were 100 %.

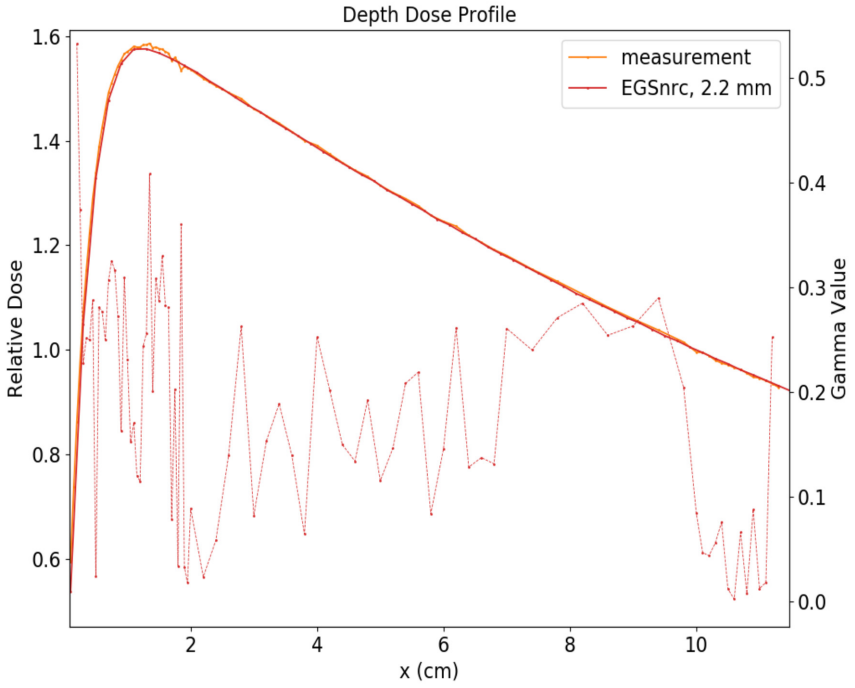

Figure 14: Comparison of measured depth dose profiles of a $2 \times 2cm^2$field with simulations performed with Monaco and EGsnrc for a monoenergetic primary electron beam energy of 7.4 MeV. The dotted line shows gamma values for a gamma criterion of 2 %/2 mm. All points show a gamma value smaller than 1

2.2.4.2 Radial intensity Distribution

Table 6 shows results for maximum and average relative errors for both in and cross plane profiles as well as the off-axis factor for varying FWHM values in the range of 0.2 mm to 4 mm. For cross plane profiles, the maximum error was minimal for 1.5 mm FWHM, whereas the average error showed a minimum value at 1 mm FWHM. In addition, both average and maximum deviation showed a local minimum at 2.2 mm FWHM with values of 0.69 % and 2.07 %, respectively. In contrast, for calculated in plane profiles all three examined parameters showed clear minimum values of 0.37 % (average deviation), 1.44 % (maximum deviation) and 0.17 % (off-axis factor) at 2.2 mm, whereas values for all three parameters were considerably larger for 1 mm and 1.5 mm FWHM. Overall, in plane profiles were found to be more sensitive to variations of the radial intensity FWHM than cross plane profiles, as differences between errors for different FWHM values were greater for in plane profiles than for cross plane profiles. The average of the minimum values for the maximum and average relative deviations, gamma pass rates and off-axis factor determined through a parabolic fit of the difference plots was (2.2 $\pm$ 0.3) mm. An optimum radial FWHM of 2.2 mm was therefore chosen. Resulting simulations for in and cross plane profiles produced with a FWHM of 2.2 mm in comparison to measurements and Monaco simulations are shown in figure 15. Gamma pass rates for EGSnrc (Monaco) simulations were 98.94 % (95.74 %) and 90.32 % (88.71 %) for cross and in plane profiles, respectively.

Table 5: Average and maximum relative errors in the fall-off region of depth dose profiles for a 2×2 cm^2 when comparing measured data and EGSnrc simulations to varying mean electron energies. Both maximum and average deviations are minimal for an optimum electron energy of 7.4 MeV (grey marking).

Electron energy (MeV)	Max. rel. error (%)	Av. rel. error(%)	gamma rate (%)
6.7	1.45	0.54	95.56
6.8	1.27	0.45	93.33
6.9	1.05	0.40	100.00
7	0.89	0.33	100.00
7.1	0.66	0.24	100.00
7.2	0.51	0.18	100.00
7.3	0.51	0.17	100.00
7.4	0.45	0.18	100.00
7.5	0.55	0.26	100.00
7.6	0.63	0.32	100.00
7.7	0.73	0.38	100.00

2.2.4.3 Energy Distribution

Resulting deviations for variations of the energy spread from 0 % (monoenergetic) to a gaussian energy FWHM of 20 % (1.48 MeV) of the optimum mean energy value are shown in table 7. For the cross plane profile, slightly smaller errors were found for monoenergetic beams and beams with a 20 % electron spread, whereas in plane and depth dose profiles showed a marginal tendency to beams with a 10 % energy spread. Besides, in plane profiles showed the highest gamma pass rate for monoenergetic beams. Cross plane profiles seem to be more sensitive to energy spread variations, as differences in errors were larger than for in plane profiles. However, differences in deviations were found to be minor for a varying energy spread compared to differences provoked by changes in electron energy and radial

distribution. Therefore, no clear result can be found and simulations are assumend to be insensitive to energy spread variations. Therefore, initial electron beams were assumed to be monoenergetic.

Comparisons of measured and simulated depth dose, in and cross plane profiles of a 10×10 cm^2 field (figs. S3 to S5) and a 57×22 cm^2 field (figs. S6 to S8) performed with the final MR-Linac model with a monoenergetic 7.4 MeV electron beam and a radial FWHM of 2.2 mm, as well as the depth dose profile of the 22×22 cm^2 field (figure S2) are shown in the supplementary material.

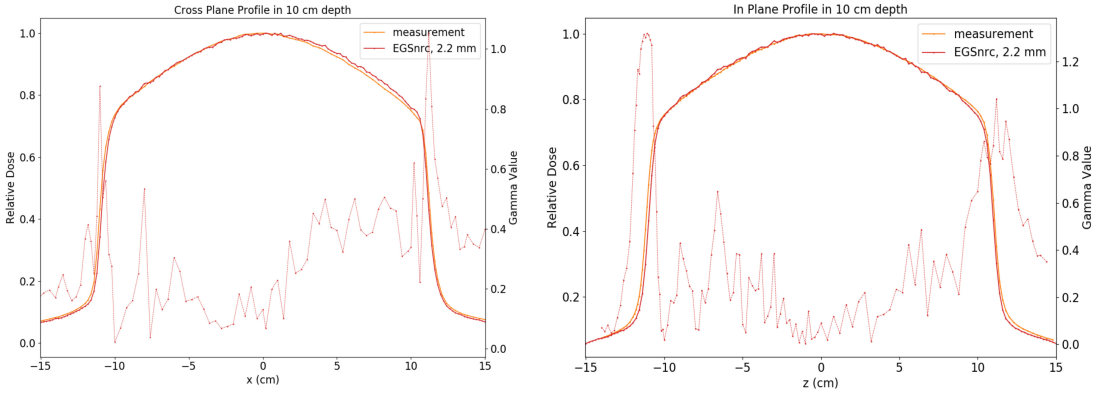

Figure 15: Comparison of measured in- and cross-plane profiles of a 22 9 22 cm2 field in 10 cm depth with simulations performed with Monaco and EGsnrc for a monoenergetic primary electron beam energy of 7.4 MeV and a radial full width at half maximum of 2.2 mm. The dotted line shows gamma values for a gamma criterion of 2 %/2 mm.

2.2.4.4 Output factors

With the final MR-Linac model, output factors for varying field sizes have been calculated and compared to measurements as a cross-check for the determined primary electron beam parameters. The average relative deviation between measured and simulated ouput factors was 0.60 % with a maximum relative deviation of 1.18 % for a field size of 3×3 cm^2. A good agreement between measured and simulated output factors could therefore be achieved with the final MR-Linac model using a electron mean energy of 7.4 MeV and a radial FWHM of 2.2 mm. Measured and simulated output factors are listed in table 8 and shown in figure 16.

Table 6: Comparison of in and cross plane profiles of measurements and simulations for varying FWHM of the gaussian radial distribution. An optimum value of 2.2 mm with minimum errors was chosen based on the average of the optimum values found for the individual parameters (grey marking).

	Cross Plane			**In Plane**			
FWHM (mm)	max. rel. error (%)	av. rel. error (%)	gamma rate (%)	max. rel. error (%)	av. rel. error (%)	off-axis factor (%)	gamma rate (%)
0.4	3.16	0.90	98.88	3.71	1.29	2.55	84.87
0.6	3.08	0.92	98.88	3.04	1.06	2.46	85.87
0.8	2.56	0.88	100.00	1.93	1.00	2.57	81.51
1.0	2.29	0.59	98.88	2.65	0.91	1.77	84.03
1.5	1.52	0.62	98.88	2.72	0.95	1.80	84.89
1.8	2.50	0.72	98.88	2.11	0.53	1.00	89.08
2.0	2.27	0.70	100.00	1.46	0.41	0.47	88.26
2.2	2.07	0.69	100.00	1.44	0.37	0.17	90.76
2.5	2.96	0.90	100.00	1.71	0.49	0.47	91.60
3.0	3.62	1.12	100.00	1.83	0.67	0.76	89.92
3.5	4.70	1.57	97.75	2.37	1.01	1.08	88.24
4.0	4.13	1.61	89.89	2.88	1.18	1.49	86.55

Table 7: Comparison of measured and simulated in, cross plane and depth dose profiles of a 22 × 22 cm^2 field for varying FWHM values of the gaussian energy distribution. Gamma pass rates for all depth dose profiles were 100 %.

	Cross Plane			**In Plane**				**Depth Dose**	
FWHM (MeV)	max. rel. err. (%)	av. rel. err. (%)	gamma rate (%)	max. rel. err. (%)	av. rel. err. (%)	off-axis factor (%)	gamma rate (%)	max. rel. err. (%)	av. rel. err. (%)
0	2.07	0.69	98.86	1.44	0.37	0.17	90.32	1.30	0.48
0.74	3.31	0.87	98.94	1.06	0.35	0.14	89.52	1.14	0.44
1.48	2.47	0.66	100.00	1.41	0.36	0.21	89.51	1.25	0.50

Table 8: Output factors for EGSnrc MC calculations wit the final MR-Linac model in comparison with measurements.

Field Size (cm)	Measurement	EGSnrc MC	% Diff Meas-EGSnrc
2 × 2	0.8096	0.8046	-0.62%
3 × 3	0.8651	0.8753	1.18%
5 × 5	0.9201	0.9235	0.37%
10 × 10	1.0000	1.0000	0.00%
15 × 15	1.0519	1.0466	-0.50%
22 × 22	1.1058	1.0959	-0.90%

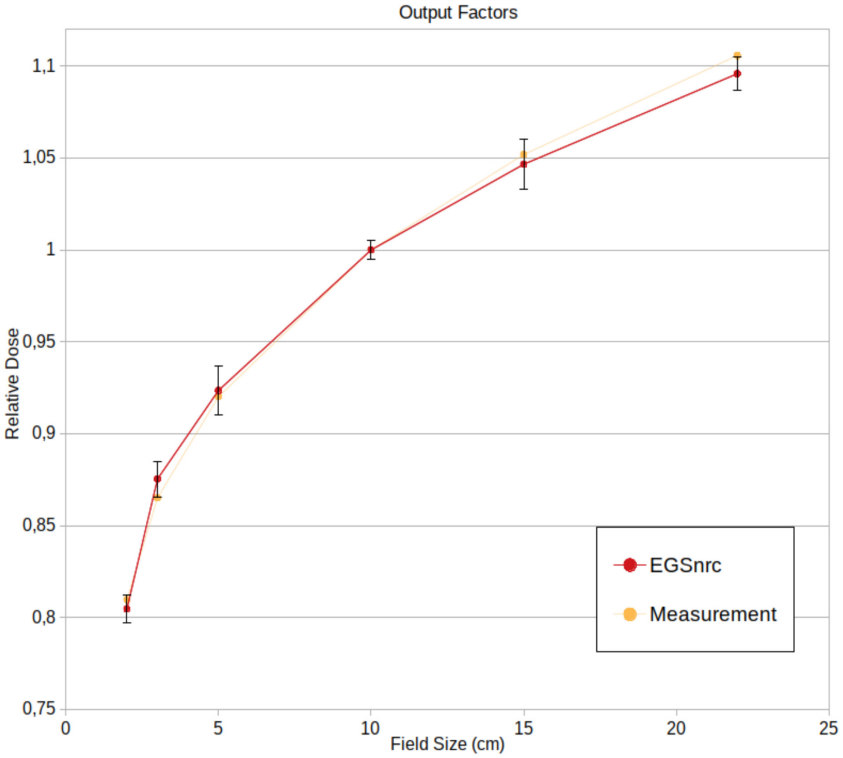

Figure 16: Comparison of measured and simulated output factors

2.2.4.5 Clinical Treatment Plan

A comparison of a clinical step-and-shoot IMRT plan for a prostate cancer patient with 23 segments calculated in Monaco and EGSnrc is shown in figure 17. The gamma pass rate for all voxels inside the patient with a dose value greater than zero was 99.83 %, whereas the gamma pass rate for all voxels with a dose greater than 40 % of the maximum dose was 97.77 %.

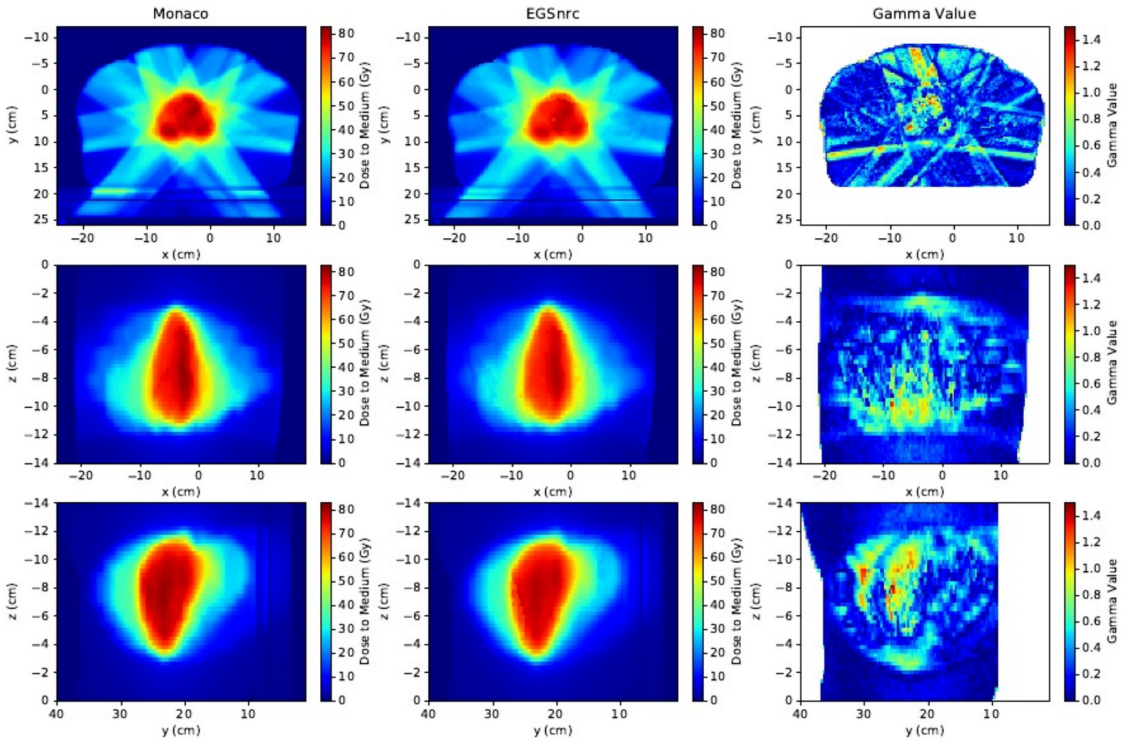

Figure 17: Simulated intensity-modulated radiation therapy plan with 23 segments in Monaco (first column) and EGSnrc (second column) shown in three different planes (coronal (xz), axial (xy), and sagittal (yz)) through the high-dose area. In the third column, the gamma values are shown for all planes. The percentage of voxels passed was 99.83% of all voxels inside the patient. [Color figure can be viewed at wileyonlinelibrary.com]

2.2.5 Discussion

In this study, a 1.5 T/7 MV Elekta Unity (Elekta AB, Stockholm, Sweden) model was implemented in BEAMnrc and initial electron beam parameters were optimized by comparing DOSXYZnrc simulations to water phantom measurements. The optimal inital electron beam model was found to be monoenergetic with a mean energy of (7.4 $\pm$ 0.2) MeV and a gaussian radial intensity distribution with a FHWM of

(2.2 ± 0.3) mm. For parameter values within the given uncertainty range, no considerable difference in dose deposition is expected. Average relative deviations of EGSnrc simulations with optimal parameters from measurements were below 1% for all profiles. A maximum relative deviation of 2.07 % was found for the 22 × 22 cm^2 cross plane profile. In general, in plane profiles showed a better accordance with measurements than cross plane profiles, which might be a result of imperfect measurements due to magnetic field influences. One possible explanation is the magnetic field induced shift of the effective measurement point for ionization chambers when measuring cross plane profiles [136]. In addition, uncertainties in the detector alignment on the water tank scanning system may have led to slightly tilted profile measurements.

During parameter tuning, variations of the electron mean energy showed a larger impact on depth dose than lateral profiles, whereas lateral profiles were shown to be more sensitive to variations of the radial FWHM. The largest relative difference between simulations performed with 2 × 2 cm^2 monoenergetic electrons beams of 6.7 MeV and 7.7 MeV was 7.55 % for depth dose profiles and 0.90 % for lateral profiles for voxels with doses greater than 50 % of the maximum dose. The largest relative difference between simulations performed with radial FWHMs of 0.2 mm and 4.0 mm was 9.49 % for lateral profiles and 1.39 % for depth dose profiles for 22 × 22 cm^2 fields and voxels with doses greater than 50 % of the maximum dose. All profiles were found to be insensitive to energy spread variations. Those observations are in accordance to findings of previous studies performing initial electron beam parameter tuning without considering magnetic field effects [45, 112, 162, 163, 182]. Compared with those studies, a generally lower sensitivity of lateral profiles to variations of initial electron beam parameters was found for simulations with the MR-Linac model. This is probably due to the absence of a flattening filter, whose presence leads to typical dose profile “horns” in the shoulder region of lateral profiles with decreasing energy and small radial distribution FHWM [182].

Due to the magnetic field influence on cross plane profiles, off-axis factors typically used for the comparison of simulated and measured lateral profiles [162, 182] could only be calculated for in plane profiles. Hence, other parameters for the comparison of measured and simulated cross plane profiles had to be identified. The chosen maximum and average relative deviations in the region of ±9.5 cm around the central axis showed a similar behaviour compared to the off-axis factor, but with a lower sensitivity to radial intensity variations. The maximum relative deviation beteween measured and simulated depth dose profiles was more sensitive to variations of the initial electron beam energy compared to the average deviation.

Overall, ouptut factors calculated with the final MR-Linac EGSnrc model were in good agreement with measurements. In comparison to Monaco simulations, EGSnrc simulated profiles showed higher gamma pass rates for all performed simulations. This is partly due to the higher statistical uncertainty of the Monaco simulations which deteriorates gamma pass rates. Nevertheless, a difference of almost 2 % in gamma pass rates achieved with Monaco and EGSnrc simulations cannot be sufficiently explained by differences in statistical uncertainty, hence suggesting a better accuracy and agreement with measurements compared to simulations performed by Monaco.

For a proof of principle, the accelerator head model with optimized initial electron beam parameters was used to recalculate a clinical IMRT treatment plan with 23 segments exported from Monaco. Despite a high overall gamma pass rate of 99.83 %, some voxels in the medium and high dose regions showed a gamma value greater than 1. The majority of voxels failing the gamma criterion are located in areas with steep dose gradients. Especially in high dose areas, steep gradients are present, which explains the lower gamma pass rate of 97.77 % for voxels with doses greater than 40 % of the maximum dose. Dose differences outside of gradient regions probably originate from different material densities used within EGSnrc and Monaco, as the default EGSnrc material conversion ramp was used for phantom creation with *ctcreate*. Dose differences close to the couch surface and in the couch structure itself (upper y-axis) are due to different material asignments of couch materials in EGSnrc and Monaco, which leads to a lower dose deposition in the couch structure in EGSnrc.

GEANT4 MR-Linac dose simulations in a heterogeneous lung-tumor phantom including a magnetic field of 1.5 T performed by Ahmad et al.[4] showed similar gamma pass rates to the present study, ranging from 98.91 % to 99.98 % for quadratic beams with fields sizes of 2×2 cm^2 to 10×10 cm^2 using a gamma criterion of 2 %/2 mm. Again, voxels failing the gamma criterion were mostly located at beam edges and in high dose gradient regions. Overall, the GEANT4 simulations showed smaller deviations from Monaco calculations compared to the EGSnrc simulations presented in this study. This can be due to the use of different Monte Carlo codes, variance reduction techniques, residual errors in the final MR-Linac accelerator head model and differences in beam definitions, as Ahmad et al. used a MR-Linac spectrum for the creation of quadratic beams, whereas the present study was based on a full accelerator head model. The simplicity of the lung-tumor phantom used by Ahmad et al. [4] compared to the full patient CT model in our study is another source of differences in uncertainty and associated gamma pass rates. Further, the sum-

mation of individually simulated segments in the present study leads to an overall uncertainty of the dose distribution of 1.6 % which affects the gamma pass rate.
To further improve the agreement of Monaco simulations and dose calculations performed with the EGSnrc MR-Linac model, the Hounsfield unit to material density conversion used by ctcreate has to be adapted to match material definitions used by Monaco.

2.2.6 Conclusion

In this study, a full MR-Linac accelerator head and cryostat model was developed and successfully implemented in EGSnrc. Dose calculations with the implemented MR-Linac model with optimized primary electron beam parameters are in good agreement with measurements. The model developed in this study was successfully used to recalculate a first full clinical IMRT treatment plan and thus shows the general possibility to perform secondary dose calculations of full IMRT plans. However, in order to achieve conclusive and accurate IMRT modelling, further investigations of the model have to be conducted in future studies.

Supplementary Material

The supplementary material of the publication is depicted in the supplementary material of the dissertation at section 9.2.

2.3 Quality assurance of IMRT treatment plans for a 1.5 T MR-linac using a 2D ionization chamber array and a static solid phantom

Authors : David Mönnich, Jasmin Winter, **Marcel Nachbar**, Luise Künzel, Simon Boeke, Cihan Gani, Oliver Dohm, Daniel Zips, Daniela Thorwarth

Published in: Physics in Medicine & Biology 2020 Vol. 65 Issue 16 Pages 16NT01

DOI: 10.1088/1361-6560/aba5ec

Manuscript version: Accepted Manuscript

Quality assurance of IMRT treatment plans for a 1.5 T MR-linac using a 2D ionization chamber array and a static solid phantom

To cite this article before publication: David Mönnich *et al* 2020 *Phys. Med. Biol.* in press https://doi.org/10.1088/1361-6560/aba5ec

2.3.1 Abstract

MR-guided radiotherapy requires novel QA methods for IMRT treatment plans (TPs). Here, an optimized method for TPs for a 1.5T MR-linac was developed and implemented clinically.A static solid phantom and an MR-compatible 2D ionization chamber array were used. The array's response with respect to the incident beam gantry angles was characterized for four different orientations of the array relative to the beam. A lookup table was created identifying the optimum orientation for each gantry angle. For the QA of clinical MR-linac TPs, beams were grouped according to their gantry angles and measured with up to four setups. The method was applied to n=106 clinical TPs of 54 patients for different tumour entities. Reference plans and plans created in the online adaptive workflow were analyzed, using a local 3 %/3 mm gamma criterion for dose values larger than 30 % of the maximum. Pass rates were averaged over all beam groups.The array's response strongly depends on the beam incidence angle. Optimum angles typically range from -10° to 80° around the phantom setup angle. Consequently, plan verification required up to four setups. For clinical MR-linac TPs, the overall median pass rate was 98.5 % (range 88.6 %-100 %). Pass rates depended on the tumour entity. Median pass rates were for liver metastases SBRT 99.2 %, prostate cancer 99 %, pancreatic cancer 98.9%, lymph node metastases 98.7%, partial breast irradiation 98%, head-and-neck cancer 97.7 %, rectal cancer 94 % and others 96.6 %. 85 % of plans were accepted straightaway, with pass rates above 95%. A single plan with a pass rate below 90% was subsequently verified with a modified method. Off-axis target volumes, e.g. partial breast irradiations, were verified successfully using a lateral shift of the phantom.The method is suitable to verify reference and online adapted TPs for a 1.5T MR-linac, including plans for off-axis target volumes.Ethical Statement: The research was carried out in accordance with the principles outlined in the IOP Publishing ethical policy. All patients gave informed consent in a clinical trial that was approved by the local ethics board (659/2017BO1).

2.3.2 Introduction

Magnetic resonance imaging (MRI)-guided adaptive radiotherapy (RT) is a novel treatment modality which has recently been introduced clinically [1, 150]. It promises accurate soft-tissue and tumour visualization for online RT plan adaptation as well as functional characterization and intra-fraction imaging. This may enable safety

margin reduction, improved organ at risk sparing and hypo-fractionation in anatomical sites that can only be poorly visualized on cone-beam CT. Furthermore online functional imaging may facilitate biologically individualized RT [28].Novel methods and tools for commissioning and quality assurance (QA) of MR-linac systems have to be developed, e.g. because of magnetic field effects and space requirements [201]. One particular QA aspect in RT is the validation of IMRT treatments plans, i.e. plan QA. Typical measurement procedures test the beam model and the dose calculation of the treatment planning system (TPS), as well as the transfer to the record and verify system and finally the correct application of the plan by the linac. Plan QA systems by different vendors have been characterized for the use in MR-linac systems, including phantoms using diodes [77, 189]. Also, radiochromic films can be used, but magnetic field effects have to be considered, e.g. the electron return effect in thin air layers close to the film [153, 154]. The measurement of transit beams through a phantom or in vivo through the patient using an on-board portal imaging device can potentially be used for plan QA [179]. Another, less direct, QA procedure for plans is the recalculation of the dose distribution with independent software and comparing it with the original dose distribution, checking just the software part of the workflow. This gap may partly be closed by additionally comparing the parameters logged by the linac control system, e.g. leaf/jaw positions and gantry angles, with the set values in the treatment plan [166]. In this work, an optimized method for plan QA for the Elekta 1.5T MR-linac named Unity (Elekta AB, Stockholm, Sweden) is described and validated for the first n=54 clinical treatments at our institution [199]. The method can also be transferred to other MR-linac systems. It requires the solid octagonal QA phantom Octavius (PTW Freiburg, Germany) and the MR compatible Octavius ionization chamber array Octavius 1500MR (PTW Freiburg, Germany). The performance of the non MR compatible version of the chamber array has been characterized earlier [168, 184], including the dependence of the chamber array response on the incidence beam angle. As the static phantom can accommodate a maximum number of eight orientations of the array, we report a method using the optimum possible phantom setup for each beam gantry angle in a treatment plan.

2.3.3 Material and Methods

2.3.3.1 Plan QA equipment

For patient plan QA a hexagonal Octavius polystyrene phantom (PTW Freiburg, Germany) and a 2D ionization chamber array 1500MR (PTW Freiburg Germany) were used. The spatial resolution of the array is 7.1 mm. An absolute dose calibration for all detectors in the array was available, which can be applied for measurements outside of strong magnetic fields. For measurements in a 1.5T magnetic field, a cross-calibration with the monitor calibration setup was performed. For cross-calibration, the central chamber of the detector array was placed in the isocenter of the MR-linac covered by a 9.5 cm stack of RW3. This setup results in a measurement depth of 10 cm (SSD of 134.5 cm and SDD 144.5 cm), which is equivalent to our institutional setup for absolute dose calibration in a water tank phantom. The magnetic field dose correction factor for the central chamber in the array was obtained for horizontal orientation of the array (gantry angle 0°). For the horizontal setup a correction factor of 1.015 was used, accounting for the lower attenuation of the helium cryostat compared to the 90° setup that is used for monitor calibration. The cryostat attenuation was characterized during commissioning of the MR-linac. The use of RW3 instead of water was corrected by a factor of 1.010. Dose measurements were recorded and compared with simulated (i.e. evaluated) dose distributions with a gamma comparison method [110] using the software tool Verisoft 7.2 (PTW Freiburg, Germany). For an accurate calculation of a minimum gamma value for each measured dose point, the sample step size of the evaluated dose matrix must be much lower than the distance to agreement (DTA) criterion being used. To achieve this, different methods have been developed, with a focus on computational efficiency [85, 194].

2.3.3.2 Treatment planning and QA plans

Patient treatment plans were created in the TPS Monaco 5.4 (Elekta AB, Stockholm, Sweden). This TPS includes magnetic field effects on the dose deposition. Monte Carlo dose calculation accuracy was 1 % in the high dose volume and the dose grid resolution was 3 mm. The fluence sequencing parameters were set to a minimum segment area of 4 cm^2 and a minimum MU/segment of 4. In total, 106 MR-linac IMRT treatment plans of 54 patients were measured and evaluated according to the

protocol presented in this study. 56 reference plans and 50 online adapted treatment plans were measured before the first treatment or following adapted treatment fractions, respectively. Four to eleven IMRT step-and-shoot beams were used. The number of segments per plan varied between 13 and 72. Additional plan characteristics can be found in Supplementary Material 1.QA plans were calculated on a contoured CT scan of the Octavius phantom in the TPS. The relative electron density in the whole phantom, including the chamber array, was forced to 1.012. Dose calculation accuracy and dose grid resolution was 1 % and 3 mm, respectively. In the lateral (IEC 61217 X) and longitudinal direction (Y) the position of the central chamber coincided with the isocenter. In the vertical direction (Z) the MR-linac isocenter is located at a fixed height of 14cm above the couch surface. Due to the phantom geometry and mechanical play, the vertical position of the array center is located 1.9cm and 1.8cm above isocenter, for horizontal and vertical arrays setups, respectively. This was accounted for when measuring and evaluating the dose in Verisoft.

2.3.3.3 Measurements

In order to achieve acceptable results with the static setup, the orientation of the chamber array had to be adapted to the gantry angles of the measured beams. The optimum performance is achieved for almost perpendicular beam incidence. As this cannot be realized for all IMRT beams, the four cardinal orientations were considered for the phantom setup (Figure 18). A lookup table of optimum phantom/array orientation with respect to the beam angle was created by measuring static rectangular $10 \times 22 cm^2$ fields in steps of 10° gantry angle for each orientation. The optimum setup for each beam gantry angle was identified by the highest gamma pass rate compared to the dose calculated in Monaco for the respective beam. The gamma criterion was 3 mm / 3% referred to the maximum dose for perpendicular incidence (i.e. 0.9 Gy). No cut-off was used.For patient plan QA the phantom was placed on the MR-linac couch top without comfort mattress. Most treatment plans were measured with the phantom laterally centered on the couch using the sagittal laser. For the Unity MR-linac the isocenter is located at a fixed lateral and vertical position with respect to the patient. Therefore, target volumes are often positioned far off-axis, e.g. partial breast irradiations (PBI). For large offsets, a lateral shift of the whole phantom setup on the treatment couch was necessary. A typical shift for PBIs was 11 cm. The longitudinal phantom position was defined by an index bar at couch index 26.5 and a set table position of 206.5 cm. The correct alignment of

the phantom/chamber array was verified using the on-board MR-linac MV imaging panel and by checking the location of the dose maximum of open fields measured with the phantom/array.Following the setup, the chamber array was zeroed and pre-irradiated with 500 MU.Typically, all four phantom orientations were used to validate a plan. Treatment plans were measured in QA mode by grouping the IMRT beams according to their respective beam angle using the lookup table. The dose of each beam group was stored as a single measurement.

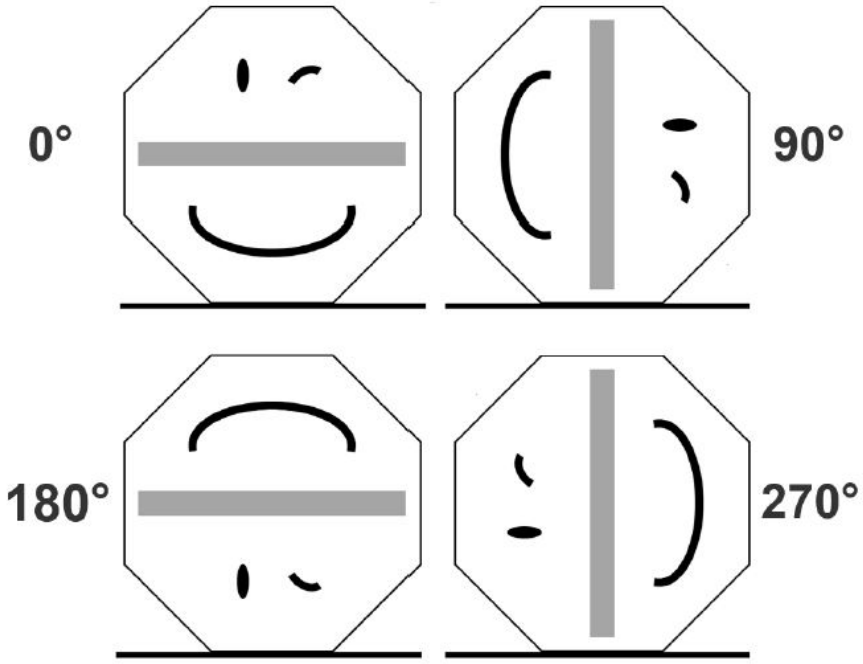

Figure 18: Illustration of the four phantom/chamber array setups used for IMRT plan QA. The Octavius smiley was pointing out of the bore in IEC 61217 –Y direction for all but the 270° setup, for which it was pointing into the bore (+Y direction). The upside of the panel was always pointing towards the upside/eyes of the phantom

2.3.3.4 Evaluation

Measured and simulated dose distributions were compared using a 3 mm/3 % gamma criterion relative to the local dose. Regions with less than 30 % of the maximum dose were excluded from the analysis. Each group of beams measured in a particular setup was evaluated separately. The resulting gamma pass rates were averaged over all phantom setups. Mean pass rates larger than 90 % were considered acceptable. Measurements with values higher than 95 % were accepted without further investigation, while between 90 % and 95 % results were visually inspected.

2.3.4 Results

2.3.4.1 Ionization chamber array cross-calibration

A magnetic field correction factor of 0.972 was found for the central chamber of the array.

2.3.4.2 Optimum phantom setup vs. beam gantry angle

In Figure 19 the gamma pass rates are plotted against gantry angle for the four phantom orientations. Pass rates are strongly dependent on the gantry angle and range from around 20 % to close to 100 % for parallel and perpendicular beam incidence, respectively. The curves are not symmetrical around the perpendicular beam angle. For all setups, pass rates decline much quicker in counter-clockwise direction (decreasing gantry angle) than in clockwise direction.From these data, a lookup table/plot showing the optimum phantom orientation for a particular beam gantry angle was generated. Typically, a particular setup is suitable for measuring beam gantry angles from -10° to 80° around the setup angle, e.g. 80° to 170° for the horizontal 0° phantom setup.

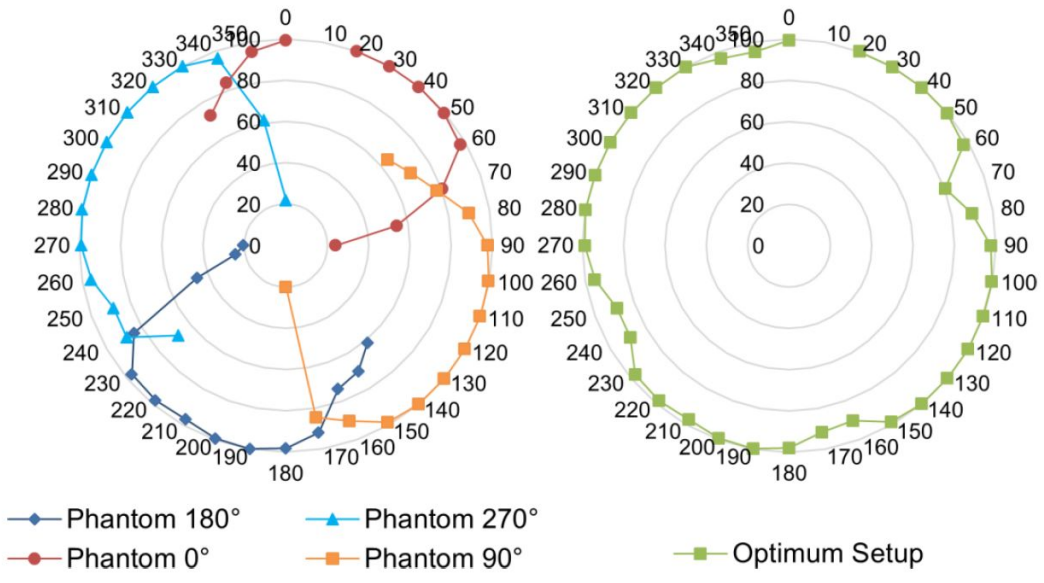

Figure 19: The dependency of the chamber array response (gamma pass rate in%) on the beam gantry angle (in °) for all phantom setups and the pass rate of the optimum phantom setup for each beam gantry angle. Pass rates of a $10 \times 22 cm^2$ field comparing measurement and TPS dose are shown

2.3.4.3 Treatment plan QA

All treatment plans were verified successfully using two to four phantom setups. The median pass rate averaged over all patients was 98.5 % and ranged from 88.6 % to 100 %. Overall, 85 % of the measurements were accepted immediately with pass rates higher than 95 %. Only a single plan showed a pass rate lower than 90 %. This plan passed the test when it was re-measured with the 0° phantom setup and all beam gantry angles set to 0°. The pass rates for each treatment plan and each phantom setup can be found in Supplementary Material S1. An example for the evaluation of a plan for a prostate cancer patient is given in Supplementary Material S9.The pass rates strongly depend on the tumour entity and the respective location and extension of the beam segments with respect to the chamber array (Table 9). The highest median pass rate of 99.2 % was observed for plans of liver SBRT (range 97.6 %-100 %). Plans for the large pelvic target volumes of rectal cancer showed a lower median pass rate of 94% (range 88.6 % - 98.5 %). Smaller off-axis volumes were measured successfully, e.g. PBIs with a median pass rate of 98.7 % (range 94.4 % - 99.5 %) Similar average pass rates, including standard deviations, were observed for the four phantom orientations.

Table 9: Plan QA statistics per tumour site

Plan type	Median	Min	Max	Number
Lymph node met	98.7	95.6	99.9	14
Partial breast	98.0	94.4	99.5	19
Prostate cancer	99.0	95.6	100.0	19
Rectal cancer	94.0	88.6	98.5	14
Liver SBRT	99.2	97.6	100.0	21
Head and neck	97.7	94.6	99.7	7
Pancreas	98.9	94.3	99.6	4
Other	96.6	93.1	99.3	8
Total				106

2.3.5 Discussion

In this manuscript, a method for the QA of IMRT treatment plans for the Elekta Unity was presented in detail. Its performance was evaluated based on the measurement of 106 plans. To our knowledge, this is the first work reporting a plan QA method for this type of equipment.Before measuring clinical treatment plans, the angular response of the combination of the static Octavius phantom and the Octavius 1500MR chamber array has been characterized. A strongly augmented angular dependency was found for the use of the array in a 1.5T magnetic field, which cannot be compensated by a simple angle dependent correction factor. Typically, an angle range of -10° to 80° around perpendicular beam incidence can be accurately measured, which is different for measurements at a conventional linac, i.e. without magnetic field, where the response is isotropic and accurate for incidence angles up to 60° [184]. It was validated, that the particular chamber array used in this study performs as expected for conventional linac fields. As a consequence, up to four different orientations were used for plan verification and the optimum setup for each beam was taken from a lookup table. Beams never crossed the bottom part of the phantom; therefore it is not a problem that it contained a compensation cavity designed for use in combination with the predecessor version of the Octavius 1500 chamber array, the Octavius 729. We hypothesize, that the arrays anisotropic response results from the influence of the magnetic field on the secondary electrons in the air cavities of the ionization chambers. For instance, oblique beams rotated counter-clockwise/clockwise from perpendicular incidence, the Lorentz force accelerates electrons towards/away from the entrance electrodes of the chambers, respectively. This may be interpreted as an electron return effect for oblique beam incidence [149]. For a thorough understanding of the effect, an investigation of the complex interaction of photon beam, chamber geometry and electric as well as magnetic fields is necessary.The absolute dose calibration of the chamber array supplied by the vendor is not valid in a 1.5 T magnetic field. A correction factor was obtained experimentally under monitor calibration conditions. This is in accordance with AAPM recommendations to perform a cross calibration against a standard dose before each measurement session [122]. However, the array has proven stable enough to simply correct for temperature and air pressure before each session.In general, measurements and simulations were in very good agreement for both reference and online adapted plans. A high fraction of plans was accepted immediately and only 15 % of the plans underwent further review. The gamma pass rates were strongly dependent on the plan type. Treatment plans of rectal cancer

patients generally showed lower pass rates and a greater variance over the phantom setups.The rectal cancer target volumes are centered in the lateral direction, but very close to the couch top and hence off axis. Typical segments have a large area and often extend to the longitudinal limits of the MLC. By investigating the gamma maps it became obvious that large deviations predominantly occur when segments hit the lateral edges of the array, where a bar of high density material is running along both edges. This can occur in all four phantom setups and could be mitigated by different lateral shifts for each phantom orientation. Though, this method is limited by the large segments hitting the array from oblique angles. An alternative option would be to collapse all beam gantry angles to 0° for plan QA. This method neglects influences of the angular dependence of the attenuation by the helium cryostat, the complex construction of the MR-linac couch and gravitational effects on the beam limiting devices.The acceptance criterion used in this study deviates from AAPM recommendations [122]. Here, the local dose deviation was used, being much more demanding in low dose regions than the recommended deviation relative to the maximum dose. On the other hand, only voxels with a dose higher than 30 % of the maximum dose were evaluated, as opposed to the recommended 10 %. The higher cut-off was chosen, because low dose regions in the measurement plane grow for oblique beams.The presented method has proven very flexible in measuring off-axis target volumes. For example all PBI treatment plans, which are typically located more than 10 cm from the isocenter of the MR-linac, could be verified successfully with a lateral offset of the phantom. Not all plan QA systems offer this flexibility. An additional advantage is its simplicity, combining existing and new devices. The measurements are not limited to a single dose plane, but cover up to four dose planes in the phantom, though not the full dose distribution. Therefore it is a semi three dimensional method, which does not require further processing of the measured data, such as extrapolation via depth dose curves.

2.3.6 Conclusion

A novel method for the QA of IMRT treatment plans for a 1.5T MR-linac was developed and characterized for 106 treatment plans. A static solid octagonal phantom and a detector array with 1405 ion chambers were used. Plans were measured with phantom orientations optimized for specific beam gantry angles. Reference and online adapted treatment plans were verified successfully, with very high agreement between measurement and simulation for almost all plans. For very large off-axis target volumes intermediate pass rates were observed, due to geometric limitations

of the phantom. The method has proven suitable for the QA of treatment plans for off-axis target volumes.

Supplementary Material

The supplementary material of the publication is depicted in the supplementary material of the dissertation at section 9.3.

2.4 Automatic 3D Monte-Carlo-based secondary dose calculation for online verification of 1.5 T magnetic resonance imaging guided radiotherapy

Authors : **Marcel Nachbar**, David Mönnich, Oliver Dohm, Melissa Friedlein, Daniel Zips, Daniela Thorwarth

Published in: Physics & Imaging in Radiation Oncology 2021 Vol. 19 Pages 6-12

DOI: 10.1016/j.phro.2021.05.002.

Abstract

Background and Purpose: Hybrid magnetic resonance linear accelerator (MR-Linac) systems represent a novel technology for online adaptive radiotherapy. 3D secondary dose calculation (SDC) of online adapted plans is required to assure patient safety. Currently, no 3D-SDC solution is available for 1.5T MR-Linac systems. Therefore, the aim of this project was to develop and validate a method for online automatic 3D-SDC for adaptive MR-Linac treatments.

Materials and Methods: An accelerator head model was designed for an 1.5T MR-Linac system, neglecting the magnetic field. The use of this model for online 3D-SDC of MR-Linac plans was validated in a three-step process: (1) comparison to measured beam data, (2) investigation of performance and limitations in a planning phantom and (3) clinical validation using n=100 patient plans from different tumor entities, comparing the developed 3D-SDC with experimental plan QA.

Results: The developed model showed median gamma passing rates compared to MR-Linac base data of 84.7 %, 100 % and 99.1 % for crossplane, inplane and depth-dose-profiles, respectively. Comparison of 3D-SDC and full dose calculation in a planning phantom revealed that with $\geqslant$5 beams gamma passing rates >95 % can be achieved for central target locations. With a median calculation time of 1:23 min, 3D-SDC of online adapted clinical MR-Linac plans demonstrated a median gamma passing rate of 98.9 % compared to full dose calculation, whereas experimental plan QA reached 99.5 %.

Conclusion: Here, we describe the first technical 3D-SDC solution for online adaptive MR-guided radiotherapy. For clinical situations with peripheral targets and a small number of beams additional verification appears necessary. Further improvement may include 3D-SDC with consideration of the magnetic field.

Keywords: MR-guided radiotherapy; MR-Linac; Online secondary dose calculation; Adaptive radiotherapy; Online plan quality assurance

2.4.1 Introduction

Hybrid systems combining a linear accelerator (Linac) and a magnetic resonance imaging (MRI) device (MR-Linac) for online adaptive radiotherapy (RT) are a promising new technology, which has recently been introduced clinically for a broad spectrum of tumor entities [50, 131, 195, 199]. Currently, two different technical realizations of MR-Linac systems with magnetic field strengths of 0.35 and 1.5 T are clinically available [49, 93, 175]. The main advantage of online adaptive MR-guided RT (MRgRT) is the high soft tissue contrast yielded by the MRI and the possibility of real-time RT plan adaptation on the MRI of the day [177, 203]. Such online adaptive MRgRT potentially allows the use of smaller margins and therefore better organ at risk sparing and tumor control in the future [41].

Online MR-guided adaptive RT implies the generation of a new treatment plan for each treatment fraction. Consequently, quality assurance (QA) of such online adapted treatment plans cannot be carried out using time-consuming experimental validation in phantoms which is classically used for conventional RT plan QA [17, 106]. Using simulated dose distributions for an independent secondary dose calculation (SDC) was proposed as an alternative to experimental plan QA [12, 188]. The SDC concept checks the integrity and accuracy of the simulated dose distribution by dose re-calculation using an independent calculation method. In an online setting where the RT plan has to be validated while the patient is on the treatment couch, experimental plan validation can only be done prior to the first treatment fraction [33, 126] but not during daily online adaptation. To bridge this gap and ensure patient safety in MRgRT, a fast solution for real-time evaluation of the dose distribution is required. First implementations for MRI-Linac subsystems used a point dose comparison for a check of monitor units [32, 61]. However, such point dose comparison only gives a rough dose estimation based on radiological depth but does not consider missing segments, patient or leaf positioning errors. An identified main risk of online adaptive workflows is an incorrect assignment of electron densities

[94], which can, due to high variability of plans, not be checked comprehensively by monitorunit checks and simplified calculation algorithms. Therefore, an automatic 3D-SDC, identifying dose contributions in off-isocenter positions is needed.

Recently Li et al. [107] quantified differences in dose distribution for utilization of a commercial collapsed cone dose engine in an offline comparison of treatment plans. Whereas, for a fast SDC, accelerating options of the Monte Carlo (MC) code are available for the 0.35 T MR-linac system [32, 192],magnetic field effects can only be simulated in full MC codes [53] on the 1.5 T MR-linac system. The potential of accelerated dose predictions, based on deep learning approaches [96], must still be investigated as they are dependent on training data and do not mechanistically correspond to particle interactions.

The underlying assumption of this study was, that magnetic field effects on dose profiles are most dominant in the penumbra region and that for plans with multiple beams these effects might cancel out, as for opposing beams also the Lorentz force has the opposite direction. Consequently, high dose contributions on multiple beam IMRT should be largely independent of the magnetic field.

Therefore, the hypothesis was that an independently created accelerator head model for 1.5 T MR-Linac systems neglecting the influence of the magnetic field (B = 0 T) allows fast SDC for online verification of MR-Linac plans and provides a similar level of accuracy compared to experimental plan QA at the MR-Linac.

2.4.2 Material and Methods

An accelerator head model was developed for a 1.5 T MR-Linac, implemented for fast SDC in an online MRgRT setting and the clinical performance evaluated. The MR-Linac head model was validated in a three-step process: (1) comparison to measured beam data, (2) investigation of performance and limitations in a simplified planning phantom and (3) clinical validation using n = 100 patient plans by comparing the differences between SDC and full TPS dose calculation results to those between experimental offline plan QA and the TPS.

2.4.2.1 Independent MR-Linac accelerator head model for B=0 T

The beam data of a 1.5 T MR-Linac (Unity, Elekta AB, Stockholm, Sweden) was collected with a MR-compatible prototype water tank (Beamscan-MR, PTW Freiburg,

Germany). Profiles in in- (IP) and cross-plane (CP) direction, percentage depth dose (PDD) curves and output factors (OF) were measured using a microdiamond detector (60019, PTW Freiburg, Germany) for field sizes up to 16×16 cm² and a Semiflex 3D (31021, PTW Freiburg, Germany) for fields from 16×16 to 40×22 cm². Fields were measured with gantry angle 0° at isocenter level with a source-to-isocenter distance (SID) of 143.5 cm. Due to the limited dimensions of the water tank in the bore, for this gantry angle PDDs could only be measured up to a depth of 10 cm. To consider PDDs up to a depth of 30 cm, additional square fields from 2×2 to 16×16 cm² were measured for gantry 270° with a SSD of 113.2 cm. For gantry 0°and 270°, profiles and OFs were assessed in water depths of 10 cm. This corresponds to a respective source-to-detector distances of 143.5 cm and 123.2 cm, and therefore unequal fields size at point of measurement. Profiles were normalized to the mean of the three highest scoring dose values. Profiles measured with the Semiflex 3D were shifted based on a registration from microdiamond to Semiflex to account for the lateral shift of the effective point of measurement induced by the magnetic field and were deconvolved using the BEAMSCAN software (PTW Freiburg, Version 4.3) [136]. Normalization of the PDD was done in 10 cm depth after fitting a 4th order polynomial function to the measured data starting 1 cm after the dose maximum [53]. A detailed list of measured items is shown in table 10.

A MC head model, neglecting the influence of the magnetic field (B=0 T), was created in the research TPS Hyperion [7] for the 1.5 T MR-Linac based on measured PDDs, OFs, and profiles. Hyperion simulates dose distributions based on a XVMC [89], whereas the commercial TPS (Monaco 5.40.01, Elekta, Stockholm, Sweden) uses the GPUMCD algorithm [75], thus ensuring independent calculations. Dose distributions for the water phantom were simulated in Hyperion for all measured fields for both gantry orientations with a MC-variance of 0.1 % using a grid size of 3×3×3 mm³ for comparison with the measurements. In addition, the experimental data was compared to the dose distribution simulated by the TPS , taking into account the magnetic field effect [3]. The simulations in the TPS were performed with a statistical uncertainty of 0.5% per calculation and a grid size of 3×3×3 mm³.

All data points were interpolated to the minimal measurement grid of 0.1 mm and compared as reference with the dose distribution using a global 2D gamma criterion [110] of 2 mm/2 % in Matlab R2019a (Mathworks Inc., Natick, MA, USA). All data points from -60 % to +60 % of the evaluated field size were analyzed.

2.4.2.2 Planning phantom

Magnetic field effects on the dose distributions of single beams are expected to be dominant in the penumbra of crossline profiles and, due to the electron-return-effect (ERE) [148], at air-tissue interfaces. Therefore, an in-silico phantom study was performed to investigate the influence of the magnetic field on 3D dose distributions, depending on the number of beams and proximity to air-tissue interfaces. In this phantom experiment, two planning scenarios were designed. In scenario A, the plan isocenter was positioned in the center of a cylindrical homogeneous water phantom (r=13 cm). In scenario B, the isocenter was placed 6 cm below the surface of a half cylindrical homogeneous phantom (r=19 cm), simulating a target volume near the skin surface. For both scenarios nine different MR-Linac plans were generated, with one to nine equidistant 10x 10 cm² open fields with 200 MU in the TPS (B=1.5 T) and compared to the dose distributions obtained from the SDC (B=0 T).

For both scenarios dose distributions of the TPS were compared to the SDC using an interpolated 1×1×1 mm^3 grid, a 2 mm/2 % gamma criterion and a threshold dose of 40 %D_{max}, implemented in python 2.7.

2.4.2.3 Clinical validation of MR-Linac SDC and comparison with experimental plan QA

A total of 100 plans from 57 patients which had been irradiated in the context of a phase 2 feasibility trial (NCT04172753) at the MR-Linac system between January and November 2019 were retrospectively included into this analysis. The trial was approved by the institutional review board (IRB 659/2017BO1). Plans corresponded to six different treatment sites. For each MR-Linac plan, dose distributions calculated by the TPS including magnetic field effects were compared to dose distributions for those plans generated with SDC. A detailed list of patient data is shown in table 11.

Experimental plan QA was performed for all 100 plans following our institutional QA protocol [126] with a static hexagonal phantom (Octavius, PTW Freiburg, Germany), using an ion chamber array (1500MR, PTW Freiburg, Germany). Briefly, for the plan QA, beam angle specific measurements were performed, and a weighted average of the different setups was further analyzed. Evaluation of the measurement data was done using a local gamma criterion of 3 mm/3 %, excluding doses below 30 % of the maximum dose.

For all patient plans included into this analysis, the performance of the proposed SDC approach was assessed in a clinical setting. The dose distribution generated by the TPS during online adaptive MR-guided RT (1 % statistical uncertainty per calculation, 3×3×3 mm^3 grid) was transferred to the SDC, an isocenter shift was applied based on the registration between the reference planning CT and the daily MR, followed by an immediate recalculation of the plan using the simplified MR-Linac beam model (MC-variance: 5 % per control point, 3×3×3 mm^3 grid). Calculation time was measured from the plan submission to the finalization of the SDC and gamma analysis.

Gamma analyses were calculated on a voxel grid of 3×3×3 mm^3 and evaluated with a cut-off threshold of 40 %. Due to the calculation speed requirements during the online workflow on MR-Linac systems, gamma analysis was performed on a non-interpolated voxel grid resulting in a gamma criterion of 6 mm/3 % (fast online criterion, FOC). This criterion was chosen to allow evaluation of all neighboring voxels with the greatest diagonal distance being 5.2 mm. To evaluate the accuracy of the FOC, additional gamma analysis was performed using a precision offline criterion (POC) which was recalculated after treatment on an interpolated voxel grid of 1×1×1 mm^3 with a gamma criterion of 3mm/3%. Processing of the DICOM files, voxel interpolation and global gamma analysis were performed in Python V 2.7.

2.4.2.4 Statistical analyses

Statistical analyses to assess differences between experimental plan QA results and SDC were evaluated using a Wilcoxon signed-rank test implemented in Matlab (Version R2019a).

2.4.3 Results

2.4.3.1 Independent MR-Linac accelerator head model for B=0 T

The comparison of measured MR-Linac beam data and the simplified accelerator head model for B=0 T showed median (range) 2D gamma passing rates of 84.7% (52.3-93.4%), 100.0% (94.4-100 %), and 99.1 % (58.6-100 %) for CP and IP profiles as well as PDDs (cf. table 10). PDD, as well as profiles simulated with the SDC and the TPS for the largest 16×16 cm^2 and smallest 2×2 cm^2 measured field sizes from

270° are depicted in figure 20(A-B). The mean relative deviation in OFs between the measurement and the SDC was -1.4%. A maximum deviation was observed for the largest field with -6.4 % (cf. figure 20C-D). A detailed analysis is shown in the supplementary table S3.

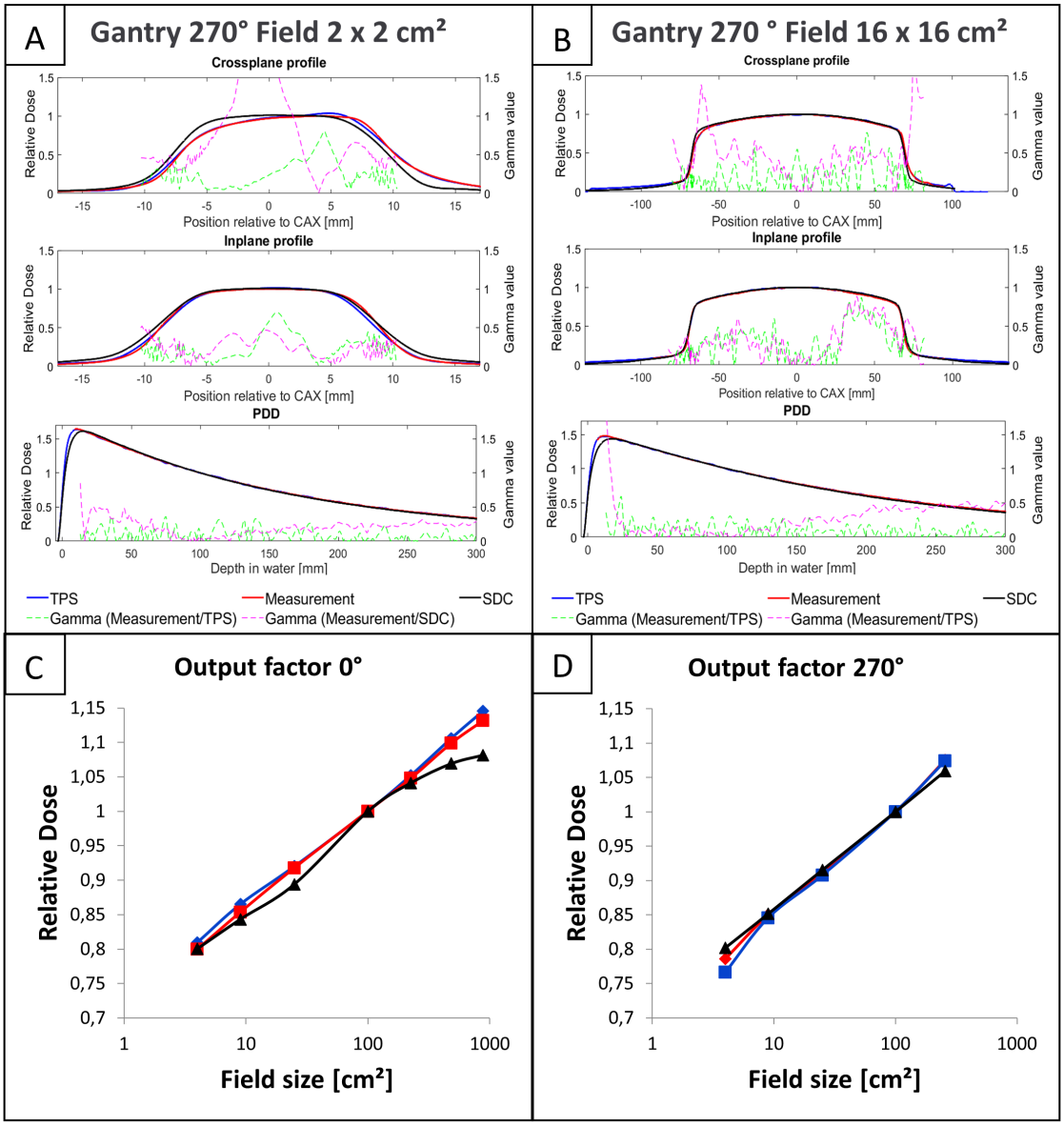

Figure 20: Comparison of the developed simplified in-house head model (black, B = 0 T), the TPS Monaco (blue, B = 1.5 T) and the measurement (red, B = 1.5 T). Dashed magenta lines depict the gamma values comparing measured data with the in-house head model. Green lines represent gamma values comparing measurement and treatment planing system (TPS). Profiles are evaluated at a depth of 10 cm and an SSD of 113.2 cm. Therefore, the shown profiles do not correspond to their field size definition at isocenter. (A) shows the smallest evaluated field size of 2×2 cm², (B) the largest field of 16×16 cm², comparing the profiles relative to the central axis (CAX) and the percentage depth dose (PDD) (C), (D) depict the comparison of the output factors at gantry angles of 0° and 270°, respectively.

Table 10: 2D gamma passing rates, comparing the experimental data in the crossplane (CP), inplane (IP) and percentage depth dose (PDD) curves to the calculated dose distribution of the SDC and TPS for various field sizes.

Gantry angle [°]	**Field size CP [cm]**	**Field size IP[cm]**	2D gamma passing rate (Measurement vs. SDC) [%]			2D gamma passing rate (Measurement vs.TPS) [%]		
			CP	**IP**	**PDD**	**CP**	**IP**	**PDD**
0	2	2	64.0	100.0	58.6	100.0	100.0	100.0
0	3	3	68.3	100.0	95.8	100.0	100.0	100.0
0	5	5	85.3	100.0	98.9	99.7	100.0	100.0
0	10	10	85.2	100.0	99.7	100.0	100.0	100.0
0	15	15	93.4	100.0	99.1	99.7	100.0	100.0
0	22	22	84.1	100.0	99.1	99.4	100.0	100.0
0	40	22	52.3	94.4	98.5	99.2	100.0	100.0
270	2	2	73.9	100.0	100.0	100.0	100.0	100.0
270	3	3	76.7	100.0	100.0	100.0	100.0	100.0
270	5	5	86.0	99.2	100.0	100.0	100.0	100.0
270	10	10	92.4	100.0	99.6	100.0	100.0	100.0
270	16	16	91.1	100.0	98.9	100.0	100.0	100.0
Median			84.7	100.0	99.1	100.0	100.0	100.0

2.4.3.2 Planning phantom

The gamma passing rate for the cylindrical phantom with a central target varied between 89.2 % and 99.9 % for three and eight beams, respectively whereas for the half cylindrical phantom with the target close to the surface the gamma passing rates varied between 84.2 % and 95.8 %.

Overall, plans using more than five beams yielded pass rates of approximately 95%. Detailed results of the comparison for both planning scenarios are shown in figure 21.

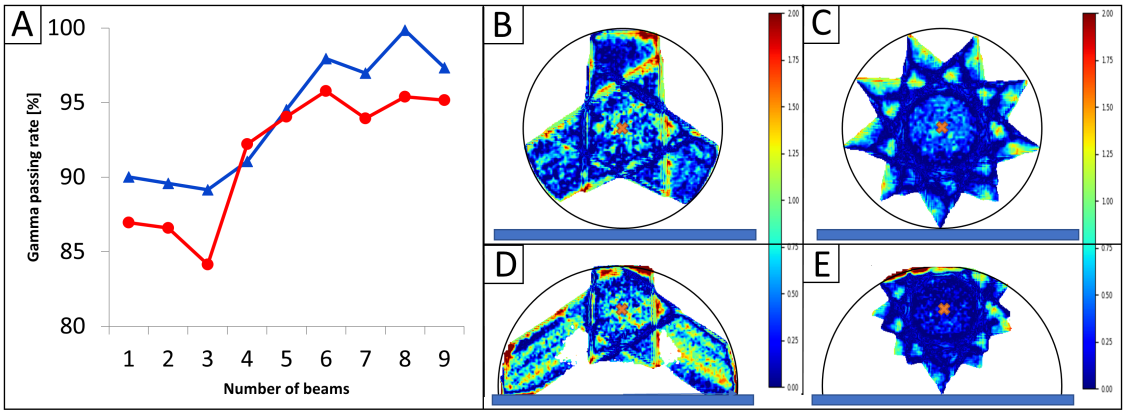

Figure 21: Resulting gamma passing rate as a function of the number of beams for planning scenario A (Blue) and scenario B (Red). In B-C the gamma map is shown for the cylindrical phantom, in D-E for the half cylindrical phantom for 3 and 9 beams, respectively. Depicted in black is the external phantom outline. Depicted in blue is the couch position and the corresponding isocenter position is marked in orange.

2.4.3.3 Clinical validation of MR-Linac SDC and comparison with experimental plan QA

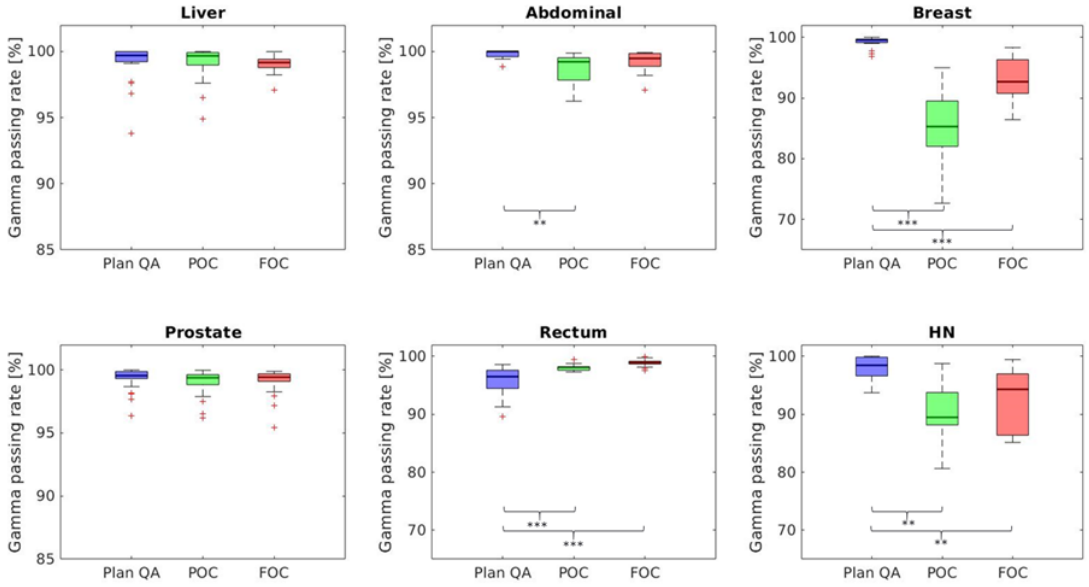

Figure 22: Boxplots showing the experimental plan verification (Plan QA) in blue, the precision offline criterion (POC) in green and the fast online criterion (FOC) in red . The y-axis depicts the gamma passing rate in % (*p<0.05, **p<0.01, ***p<0.001).

Overall, the measured plan QA data showed a median (IQR) gamma agreement with the simulated dose distributions by the SDC of 98.9 (97.0-99.5) % (p=0.005) and 98.2 (94.1-99.5) % (p<0.001) for the FOC and POC, respectively, whereas the

median (IQR) experimental gamma agreement with the TPS was 99.5 (98.1-100) %. However, the gamma analysis of the SDC showed a distinct entity specific variation: For liver, prostate, abdomen and rectum cancer MR-Linac SDC using the FOC resulted in median gamma passing rates with respect to measured data of 99.2 % (p=ns), 99.4 % (p=ns), 99.5 % (p=ns) and 98.9 % (p<0.001), respectively. For breast cancer the TPS dose agreed with the SDC with a passing rate of only 92.7 % (FOC, p<0.001), whereas the measurement corresponded to 99.5%. HN plans resulted in 98.4% agreement of measurement with TPS simulation, whereas SDC using the FOC demonstrated a gamma passing rate of 94.3 % (p=0.01). An overview of SDC and experimental results is provided in figure 22. A detailed entity specific analysis is presented in table 11,and an exemplary SDC analysis are presented in the supplementary figure S10. The median calculation time for the FOC over all entities was 01:23 min.

Table 11: Entity specific analysis of the evaluated plans. Values are given in median (Interquartile range) for the measurement, fast online criterion (FOC) and precision offline criterion (POC).

Tumor entity	Liver	Prostate	Abdominal	Rectum	Breast	Head & Neck	Total
Number of patients	12	11	8	11	11	4	57
Number of plans	21	24	13	14	18	10	100
Number of Segments	58 (57-60)	32 (21-36)	46 (31-50)	36 (26-36)	23 (20-25	48 (42-54)	35 (25-56)
Calculation time [min] Voxel: 3×3×3mm³	01:38 (01:05 - 01:45)	01:07 (0:56 - 01:19)	01:32 (0:50 - 01:42)	02:16 (01:52 - 02:21)	00:57 (0:50 - 01:03)	01:55 (01:32 - 02:38)	01:23 (00:58 - 01:47)
Calculation time [min] Voxel: 1×1×1mm³	07:49 (04:53 - 08:20)	07:03 (06:13 - 07:52)	08:11 (04:21 - 09:40)	16:08 (15:11 - 17:30)	06:12 (05:51 - 06:53)	11:26 (09:01 - 12:33)	07:47 (06:08 - 09:50)
Measurement gamma passing rate [%] (3 mm /3 %)	99.7 (99.3-100)	99.6 (99.3-99.9)	100 (99.6-100)	96.5 (94.7-97.6)	99.5 (99.1-99.7)	98.4 (96.7-99.8)	99.5 (98.1-100)
FOC gamma passing rate [%] (6 mm /3 %)	99.2 (98.8-99.4)	99.4 (99.1-99.7)	99.5 (99.0-99.9)	98.9 (98.7-99.1)	92.7 (90.8-96.2)	94.3 (88.2-96.4)	98.9 (97.0-99.5)
Wilcoxon signed-rank test Measurement vs. FOC	0.31	0.51	0.15	**<0.001**	**<0.001**	**0.01**	**0.005**
POC gamma passing rate [%] (3 mm /3 %)	99.7 (99.1-99.9)	99.4 (98.9-99.6)	99.2 (98.2-99.5)	98.1 (97.6-98.2)	85.3 (82.2-89.5)	89.4 (88.4-93.8)	98.2 (94.1-99.5)
Wilcoxon signed-rank test Measurement vs. POC	0.71	0.21	**0.005**	**<0.001**	**<0.001**	**0.004**	**<0.001**

2.4.4 Discussion

A simplified MC head model for a 1.5 T MR-linac system neglecting the effects of the magnetic field (B=0 T) was developed, replicating the experimental data, and implemented as a SDC for online adaptive MRgRT. In the online workflow the developed system was able to verify the dose distribution of the TPS based on a 3D gamma analysis, with a median calculation time of 01:23 min. The analysis showed a good median agreement over all plans between the TPS and the SDC (98.9 %) as well as the plan QA measurement (99.5 %). In the entity specific analysis, the SDC showed results with accuracies comparable to experimental plan QA for

liver, prostate and abdominal cancers, whereas the measured data in breast, HN and rectal cancer was significantly different ($p<0.01$) compared to the SDC.

The proposed approach was successfully implemented in the clinical MR-Linac online workflow. Consequently, the validation of the TPS dose distributions during online MRgRT was shown to be feasible in a clinical setting. The general acceptance criterion for SDC results in the online workflow was a gamma passing rate greater than 95 %. For dose distributions that were strongly influenced by the magnetic field, an alternative validation strategy was implemented: Reference plans with gamma passing lower than 95 % were experimentally verified. During online validation similar pass rates as for the SDC of the reference plan were accepted if the failed points were clearly located at air-tissue interfaces, which are particularly susceptible to magnetic field effects.

Neglecting the magnetic field effect in the MC dose calculations resulted in differences in the dose distribution between the measured data and the simulated dose distribution. Whereas the IP profiles and the fall-off region of the PDD showed good agreement with the measurement, the dose build-up region as well as the CP profiles presented with magnetic field specific differences. The magnetic field causes a steeper dose build-up in the first 15 mm below the tissue surface and an asymmetrical CP profile, of which the relative influence depends on the evaluated field size [148]. As a consequence, the developed beam model showed best agreement for medium sized fields, due to the high relative magnetic field influence for small fields and, for the biggest fields in the CP profiles, dose overestimation of the model on the field edges were observed. The OF for very large field sizes could not be further improved without loss of quality for smaller fields. Due to a limited impact of segment areas >70 cm^2 [88] in a modulated IMRT, this prioritization of middle-sized fields was chosen. The limited agreement of very small field sizes, which is restricted by the recommended IMRT-parameter on minimal segment size of 4 cm^2 must be further investigated. The model generation on experimental beam data is transferable to other MC-based calculation systems and not limited to the in-house system Hyperion. The phantom planning study showed that the observed differences were most dominant for targets close to air-tissue interfaces, as well as for plans with a low number of beams. With an increasing number of beams the influence of the magnetic field decreased. However, for regions close to the surface, the magnetic field has a bigger impact due to ERE and electron stream effect (ESE) [65, 114].

In an online workflow, the time delay between plan calculation and application can induce anatomical uncertainties, resulting in differences between dose simulation

and application [121, 128]. Therefore, the calculation and evaluation criteria are optimized with respect to speed. This results in the evaluation of a gamma criterion of 6 mm and 3 % on the original voxel grid without interpolation between dose points.

The differences for breast cancer are most likely due to the magnetic field effect for a limited number of beams and proximity to air tissue interfaces, as confirmed by our phantom experiments. Also for HN cases, air-tissue interfaces seem to be the reason for the lower observed agreement between SDC and measured plan data. For the rectal cancer cases the SDC showed better agreement to the TPS than the measured data. This is due to limitations reported for experimental MR-Linac QA of plans with large off-axis target volumes [126].

The SDC concept implemented in this study only checks the online adapted dose distribution whereas errors may also occur during dose delivery. Therefore a subsequent offline log file analysis may be added to the proposed SDC workflow to compare the planned dose distribution with the applied dose [121]. Additionally, the calculation of a 3D dose cube may allow an anatomical contour-based evaluation of differences in DVH-parameter [167].

In conclusion, this study showed that 3D-SDC of online adapted MRgRT plans using a simplified MC head model of an 1.5T MR-Linac system, neglecting the magnetic field effects is feasible in a clinical online workflow. The proposed technical 3D-SDC solution is able to accurately estimate the dose distribution for plans with more than five beams and centrally located target volumes. For clinical situations with peripheral targets and a small number of beams additional verification appears necessary. Consequently, for central tumors the fast SDC provides a similar accuracy compared to experimental plan QA. As a next step further improvement may include the consideration of the magnetic field for high precision 3D-SDC.

Supplementary Material

The supplementary material of the publication is depicted in the supplementary material of the dissertation at section 9.4.

2.5 Partial breast irradiation with the 1.5 T MR-Linac: First patient treatment and analysis of electron return and stream effects

Authors : **Marcel Nachbar**, David Mönnich, Simon Boeke, Cihan Gani, Nicola Weidner, Vanessa Heinrich, Monica lo Russo, Lorenzo Livi, Jasmin Winter, Savas Tsitsekidis, Oliver Dohm, Daniela Thorwarth, Daniel Zips, Chiara De-Colle

Published in: Radiotherapy and Oncology 2020 Vol. 145 Pages 30-35

DOI: 10.1016/j.radonc.2019.11.025

2.5.1 Abstract

Introduction: External beam partial breast irradiation (PBI) provides equal oncological outcomes compared to whole breast irradiation when applied to patients with low risk tumours. Recently, linacs with an integrated magnetic resonance image-guidance system have become clinically available. Here we report the first-in-human PBI performed at the 1.5 T MR-Linac, with a focus on clinical feasibility and investigation of the air electron stream effect (ESE) and the electron return effect (ERE) in the presence of the 1.5 T magnetic field, which might influence the dose on the chin (out-of-field dose, due to the ESE), the skin and the lung/chest wall interface (in-field dose, ERE). Methods: A 59 years old patient affected by a 15 mm unifocal grade 1 carcinoma not special type of the right breast staged pT1c pN0 cM0 was planned and treated at Unity 1.5 T MR-Linac. To investigate the ERE and the ESE, an MR-Linac treatment plan was simulated without considering the 1.5 T B field using a research version of Monaco (V. 5.19.03). In vivo dosimetry was performed using Gafchromic® EBT3 films placed on top and underneath a 1 cm bolus which was placed on the patient's chin. The plans with and without 1.5 T magnetic field were compared in terms of dose to the chin, to the skin and to the interface lung/chest wall. Finally, the dose on the chin measured with the in vivo dosimetry was compared with the dose calculated by Monaco. Results: PBI using the 1.5 T MR-Linac was successfully performed with a 7 MV photon 7-beams IMRT step-and-shoot plan. The treatment was well tolerated, the patient developed

a slight acute toxicity, i.e. breast skin erythema and breast oedema CTC V.4 grade 1. The plan with 1.5 T magnetic field documented a fractional dose of 0.17 Gy in the chin area (2.6 Gy in 15 fractions), which was reduced to 0.05 Gy (0.75 in 15 fractions) by the presence of 1 cm bolus. The simulated plan without magnetic field showed a dose reduced by 2.3 Gy in the chin area. With the in vivo dosimetry a fractional dose of, respectively, 0.12 Gy and 0.034 Gy on top and underneath the bolus were measured (1.8 and 0.51 Gy in 15 fractions). The plan with 1.5 T magnetic field showed a skin D_2 of 40 Gy and a skin V_{35} of 40.2 %, which were reduced to, respectively, 39.7 Gy and 24.9 % in the simulation without magnetic field. At the interface lung/chest there were no differences in DVH statistics. Conclusion: PBI with the 1.5 T MR-Linac was performed for the first time. ESE is accurately calculated by the treatment planning system, can be effectively reduced with a 1 cm bolus and is comparable to dose of cone beam-CT based position verification. The additional dose caused by ERE is not associated with an increased risk of acute toxicity.

2.5.2 Introduction

Localized low risk breast tumours, usually characterized as small, hormone receptor positive, Her2 negative lesions with a low proliferation index, represent the majority of newly diagnosed breast cancers. Patients have a very favourable prognosis with overall survival rates at five years of almost 100 % [164]. The challenge is to reduce the treatment related morbidities without compromising oncological outcomes. In this context, randomized trials demonstrated that irradiation of the initial tumour area only (partial breast irradiation, PBI) instead of the entire breast (whole breast irradiation, WBI) after surgery is feasible and oncologically safe [143, 144, 169, 183, 187, 197]. Lately, the IMPORT LOW trial showed equal failure rates between PBI and WBI with better cosmesis after PBI with 40.05 Gy in 15 fractions [39]. Based on these randomized trials, PBI has become standard of care option in localized low risk breast tumours [29, 38, 80]. Recently, hybrid systems integrating a 1.5 Tesla magnetic resonance imaging device with a linear accelerator (MR-linac) have been introduced into clinical practice. MR images offer superior soft tissue contrast compared to computer tomography, which might result in better visualization of targets and organs at risk (OARs) [11, 36, 42, 57, 111, 130, 199]. Moreover, radiotherapy can be adapted online, based on the daily anatomy imaged by MR and real time MRimages can be obtained during treatment to ensure precise delivery. For PBI, the MR-linac might allow a better visualization of the tumour bed and the possibility to

adapt the treatment plan if changes such as seroma modification or breast swelling occur. On the other hand, peculiarities of hybrid MR-guided treatment devices such as interactions of secondary electrons within the magnetic field have to be considered [48, 65, 69, 92, 113, 114, 137, 148, 155]. These interactions include the electron air stream effect (ESE) which can lead to out-of-field dose deposition and the electron return effect (ERE) which may result in increased dose to the skin and at air/tissue interface. Both effects need to be correctly calculated and if possible compensated for. Experiences of PBI using low field (0.35 T) magnetic resonance image guidance have been previously reported [2, 71, 137]. Here we report the first-in-human PBI with the 1.5 T MR-linac, i.e. the translation of this novel technology into the clinical setting of breast cancer radiotherapy. Dosimetric investigations were performed to describe ESE and ERE as well as to evaluate methods to minimize their impact.

2.5.3 Material and methods

In January 2019 we treated the first patient with PBI at the 1.5 T MR-linac. She was a 59 years old patient with a primarily resected 15 mm unifocal grade 1 breast carcinoma (not special type, hormonal receptors positive, Ki 67 5%, Her2 negative). The tumour was located in the upper outer quadrant of the right breast. The patient was enrolled in a prospective phase 2 study which investigates the feasibility of imaging and treatment at the MR-linac (IRB approval number 659/2017BO1). Planning CT (Brilliance Big Bore, Philips, Eindhoven, The Netherlands) and planning MR (1.5 T Unity MR-Linac, Elekta, AB, Stockholm, Sweden) were performed on the same day in supine position with the wing board device and in free breathing. A rigid automatic registration with manual adjustments was performed to align planning CT and MR. Target definition and dose prescription were based on the IMPORT LOW protocol [39]. Briefly, the clinical target volume (CTV) was defined by including the surgical clips, the seroma/tumour bed including visible postoperative changes in the surrounding breast tissue. As the patient underwent mastoplastic surgery resulting in a relatively large postoperative surgical bed including about the upper/outer quadrant, no additional margins were added to generate a CTV2. The planning target volume (PTV) was defined as 10 mm added to the CTV, bound by 5 mm from the skin surface and limited to 7 mm posteriorly, as for PBI at the conventional linac. Following organs at risk (OAR) were considered: ipsilateral and contralateral breast, heart, ventricles, left and right coronary artery and the lungs. The skin was defined according to the publication of van Heist et al. [69], namely

as the 5 mm layer under the patient's outer contour in the area of the target volume with an expansion lateral and medial in order to cover all the possible critical areas for the ERE. We also defined a volume of interest as 5mmlayer into the lung contour in the area of the target volume to measure the impact of the ERE at the air/ tissue interface. A dose of 40.05 Gy, according to ICRU 50 recommendation, in 15 fractions was prescribed. A step-and-shoot IMRT plan for the 1.5 T MR-Linac was generated using the treatment planning system (TPS) Monaco® 5.4 (Elekta AB, Stockholm, Sweden). The reference plan was adapted using virtual couch shift and subsequent segment weight optimization based on the daily MR-images ("adapt-to-position" [199]). According to the dose calculations obtained with Monaco® and previous publications [66, 114, 137], out-of-field dose spots in the area of the chin might result as an effect of the ESE. Therefore, we placed a 1 cm bolus (Unger Medizintechnik GmbH Co. KG, Mülheim-Kärlich, Germany) on the patient´s chin. To investigate the out of field dose and the potentially increased field dose in the target area as function of the magnetic field (MF), two treatment plans with and without the 1.5 T MF were simulated using Monaco® research 5.19.03. The plans were reviewed by an expert radiation oncologist (C.D.C.) to ensure comparability with the reference plan regarding target coverage ($D_{2\%}$,$D_{98\%}$) and dose to OARs (mean heart dose, mean lung dose, lung V_{20Gy}, mean dose and $D_{2\%}$ contralateral breast). To investigate the out-of-field dose to the chin area, an in vivo dosimetry was performed for one fraction using Gafchromic® EBT3 (Gafchromic, Ashland Specialty Ingredients, NJ, USA) films placed on top and underneath the bolus. The dose was averaged in an area of 1.5 × 4 cm^2 of the radiochromic films. For the evaluation of the simulated dose, a margin of 3 mm thickness (corresponding to the dose grid resolution) was created in the TPS on top and underneath the bolus. The dose was averaged over an equivalent area of the highest scoring dose voxels. Results of the in vivo dosimetry and the simulated dose were compared. A follow up visit took place 3 months after the end of RT. Breast cosmetic outcomes were assessed by the treating physician, supported by photographic comparison with baseline (post-surgery and preradiotherapy) and scored on a 3-point graded scale (excellent, good and poor).

2.5.4 Results

PBI using the 1.5 T MR-linac was successfully performed. The patient completed radiotherapy as planned with CTC V.4 grade 1 breast oedema, erythema, warm feeling and fatigue. No other toxicities were observed. At the first follow up visit

3 months after radiotherapy there was still a breast oedema present, without other signs of toxicity. Objective and subjective cosmesis were scored as good. The treatment was feasible, all 15 fractions were performed at the 1.5 T MR-Linac with an average in-room-time needed for all treated fractions of 30.5 minutes. The detailed timeframes are shown in Table 12. A 7-beam step-and-shoot IMRT plan (5°/30°/45°/195°/240°/260°/280°) with a maximum of 4 segments

Table 12: In-room-time averaged on the 15 fractions according to the different workflow phases.

Workflow categorization	**Average time [min]**
Setup time	5,6
Image acquisition	4
Online Plan adaption	4,8
Plan approval	3,4
Data transfer	2,1
Radiation time	3,1
Post-treatment scan	3,2
Total in-room time	30,5

per beam and a total of 586 monitor units was used. The target coverage criteria and OAR constraints according to our institutional guidelines were met. Details of the plan as well as representative images of the planning and daily MR are shown in Figure 23. Regarding the ESE, the reference plan and the simulated plan with 1.5 T MF showed a fractional dose of 0.17 Gy in the chin area corresponding to a total dose of 2.6 Gy in 15 fractions. The reference plan showed a dose stream distribution from the breast to the chin suggesting that this chin dose is a result of the ESE (Figure 24 A). The simulated plan without MF showed a dose reduction by 2.3 Gy in the chin area, confirming the role of the ESE in the out-of-field dose on the chin (Figure 24 B–F). In the presence of 1 cm bolus, the TPS calculated a fractional dose of 0.05 Gy in the chin area corresponding to a total dose of 0.72 Gy in 15 fractions. In vivo dosimetry revealed a fractional dose of 0.12 Gy (total dose 1.8 Gy) on top of the bolus, 0.034 Gy (total dose 0.51 Gy) underneath.

Table 13: Dosimetric comparison between 1.5 and 0 T MF in terms of dose to the skin ($D_{2\%}$ and V_{35Gy}), dose at the interface between lung and chest wall ($D_{2\%}$ and V_{35Gy}) and maximal dose.

B Field	**1.5 T**	**0 T**
Skin $D_{2\%}$	40 Gy	39,7 Gy
Skin V_{35Gy}	40,2%	24,9%
interface lung/chest wall$D_{2\%}$	39,7 Gy	37,6 Gy
interface lung/chest wall V_{35Gy}	7.1%	7.3%
Maximal Dose	31.5 Gy	28 Gy

Regarding the ERE, the plan with 1.5 T MF showed a skin $D_{2\%}$ of 40 Gy and a skin V_{35Gy} of 40.2%. In the simulated plan without MF the skin $D_{2\%}$ was 39.7 Gy and the skin V_{35Gy} 24.9%, respectively. At the interface between lung and chest wall the $D_{2\%}$ in the presence of the MF was 39.7 Gy and 37.6 Gy without MF. The corresponding V_{35Gy} was 7.1 % with and 7.3 % without magnetic field. Data are summarized in Table 13. ERE at the interface close to the PTV resulted in an increased maximal dose of about 8.7% compared to the plan without MF (Figure 25, maximal dose in the presence of 1.5 T MF 31.5 Gy and 28 Gy without MF).

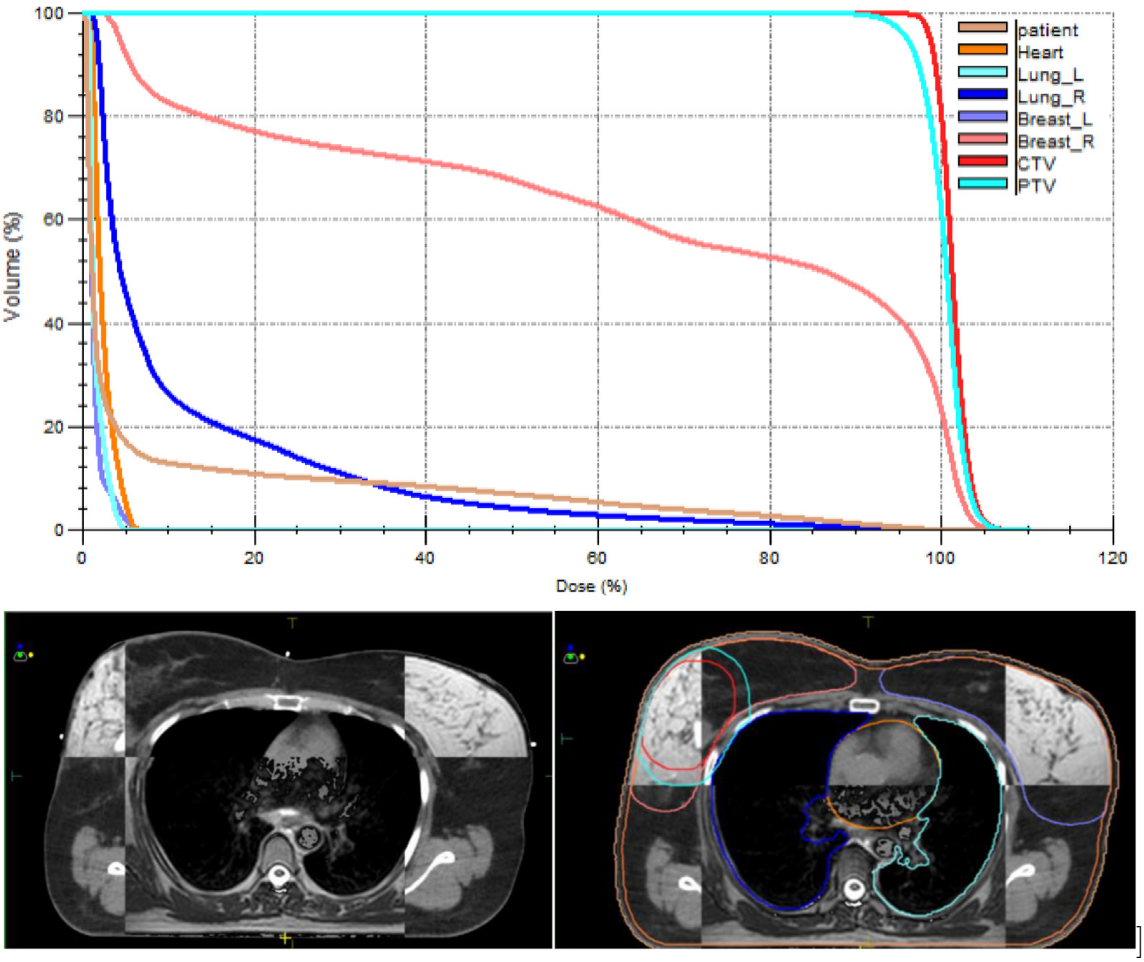

Figure 23: Upper part: Dose-volume histogram showing the CTV and PTV coverage (PTV: $D_{2\%}$ = 41.8 Gy, $D_{98\%}$ = 37.7 Gy; CTV: $D_{2\%}$ = 41.9 Gy, $D_{98\%}$ = 39.2) and the dose to the OARs (lung right: V_{20Gy} = 3.7 %, mean = 3.7 Gy, V_{5Gy} = 18.4 %; lung left: mean = 0.6 Gy, V_{5Gy} = 0 %; heart: $D_{2\%}$ = 2.4 Gy, mean = 1 Gy, breast left: $D_{2\%}$ = 2.3 Gy, mean = 0.7 Gy, V_{5Gy} = 0 %, skin $D_{2\%}$ = 33.6 Gy). Lower left: match between the planning CT and the planning MR. Lower right: match between the planning CT and the MR of the day (different craniocaudal levels).

2.5.5 Discussion

Here we report the first-in-human PBI using a 1.5 T MR-linac and investigate the ESE and ERE in this setting. PBI using lowfield magnetic resonance image guidance at cobalt-devices has already been described in the past [2, 71, 137]. During the last year, the clinical feasibility of the 1.5 T MR-linac was proved [20, 150]. For PBI, there are a number of challenges related to the design of the hybrid device including the effects of the interaction of secondary electrons with the MF. An additional challenge is represented by the beam arrangement, which has itself an impact on the ESE and ERE. Even though clinically optimal, for PBI at the 1.5

T MRlinac, beam angles between 210°–23°and 130°–150°were omitted in this case. Due to high density material in the table structure, usage of those angles might result in unpredictable dose effects during plan adaptation. The potential increase of in-field dose to the skin and at interfaces between air and issue caused by the ERE and of out-of-field dose, especially on the chin, due to the ESE, is particularly critical in low risk breast cancer patients given their excellent prognosis for long term survival. Park et al [137] described the results of a dosimetric analysis of dose on the chin in breast cancer patients treated in a 0.35 T Cobalt hybrid device. Based on the measurements of the ESE the use of a 1 cm bolus was suggested. Phantom measurements revealed a higher ESE dose in 1.5 T compared to 0.35 T with 1 cm bolus to effectively decrease this dose [114]. Based on these reports, we calculated the dose on

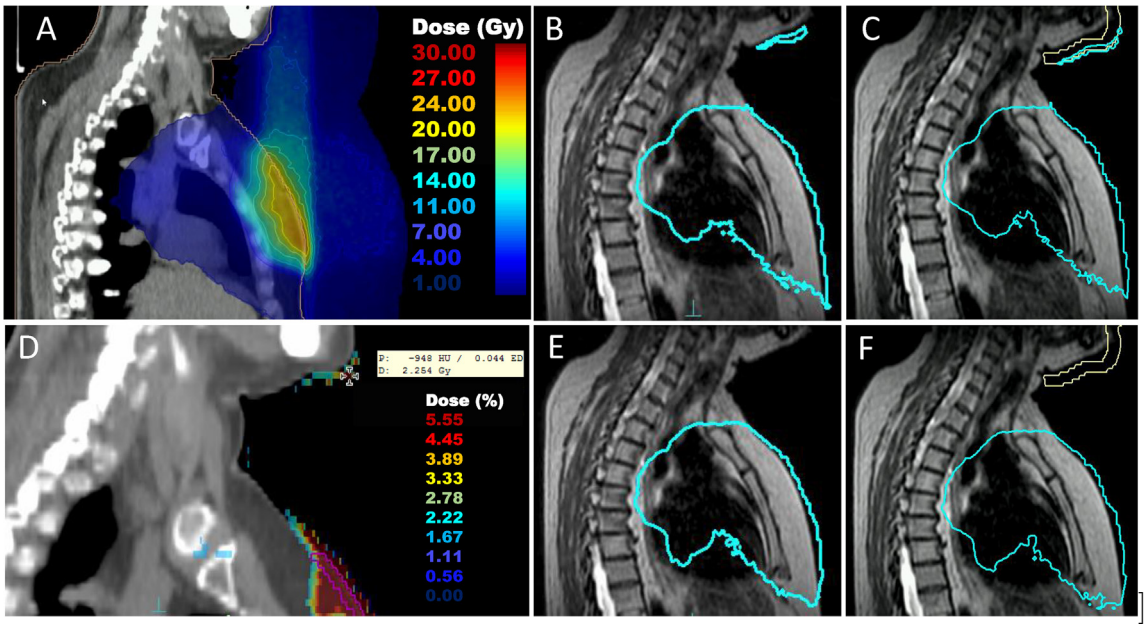

Figure 24: Treatment plan generated with Monaco displaying the dose distribution, including the dose distribution outside the patient. Here, a dose stream from the target towards the chin can be observed (A, for visualization purpose the 30 Gy isodose is shown as maximal dose, in dark red). Two plans for the same patients with and without 1.5 T magnetic field were calculated with Monaco research (B–F). The dose on the chin observed in the presence of the magnetic field (B and C) is almost reduced to zero and not visible in the plan that was generated simulating the absence of the magnetic field (E and F). With 1 cm bolus the dose to the chin is also almost reduced to zero (exact values in the text). In B-C-E-F the 1 Gy isodose is displayed in light blue. The maximal dose chin difference between the two plans is 2.3 Gy (D). (For interpretation of the references to colour in this figure legend, the reader is referred to the web version of this article.)

the chin with the dedicated TPS Monaco® and performed the treatment using a 1 cm bolus. The in vivo dosimetry confirmed the outof- field dose and its reduction by the bolus. Importantly, the in vivo measurements were consistent with the TPS dose

calculations, i.e. 4.5 % and 6.5 % of the prescribed dose (top of the bolus) and 1.3% and 1.8 % (underneath the bolus), respectively. This indicates a dose reduction by a factor of 3.5 by the bolus. In line with the low outof- field dose no acute skin toxicity was observed. Of course, no outof- field dose would be ideal. However, it should be considered that at a conventional linac besides scattered dose, image guidance modalities such as cone beam CT contribute to a comparable dose in the range of 0.03 Gy per scan [196]. Notably we could attest the GPUMCD Monte-Carlo dose calculation in the low dose out-offield region. Regarding the ERE, different planning studies and phantom experiments demonstrated an increase of the skin dose in the presence of the MF, in particular for WBI compared to PBI and for plans with tangential fields compared to multiple fields IMRT plans [48, 66, 69, 113, 148]. Our data indicate that the near maximum skin dose ($D_{2\%}$) is increased by the presence of the MF by 0.3 Gy, corresponding to 0.75 % of the prescribed dose. According to a simulation study with 0 T, 0.35 T and 1.5 T, the largest difference was found for skin volume receiving doses between 30 and 40 Gy [69]. Therefore, in the present report the skin V_{35Gy} was evaluated with and without 1.5 T MF and showed an increase by a factor of 1.6. The clinical relevance of skin V_{35Gy} is not established. Importantly, in our patient only grade 1 acute oedema and erythema was observed, i.e. no indication of increased acute toxicity. While the selected dose volume histogram (DVH) parameters to describe ERE at the interface between lung and thoracic wall were not different, it should be noted that the ERE in small subvolumes in the adjacent lung close to the PTV results to an additional dose of about 8.7 % (Fig. 3). The DVH predictive parameters for radiation induced pneumonitis are mostly derived from lung cancer patients and their applicability to breast cancer patients is questionable. Recently, Vasiljevic et al. proposed a mean lung dose (MLD) >10 Gy as predictive parameter for lung toxicity after breast irradiation [185]. The MLD in our patient was very low (3.7 Gy). It appears unlikely that the small additional dose due to ERE increases the risk of radiation-induced lung toxicity especially if one considers that in treatments with tangential fields this subvolume receives high doses. Obviously the data and conclusions derived from a single patient report are limited. In addition, an important limitation of this report is represented by the fact that the results base on a single measurement and therefore uncertainties related to the reproducibility of the dosimetric procedure are unknown. Instead of repeated measurements in individual patients we performed measurements in further nine patients as part of a larger clinical evaluation. The results are currently evaluated. The extent and potential impact of ESE and ERE need to be validated in a larger group of patients in order to substantiate the opportunities of the new 1.5

T MR-Linac for PBI. Nevertheless, our data indicate that ERE and ESE need to be taken into account in the planning phase, e.g. imaging the patient up to the nose, displaying the low doses including the chin area, eventually delineating the skin as organ at risk, optimizing the plan according to a higher dose to the skin and/or the air/tissue interface and placing a bolus on the chin during treatment delivery. We used margins to generate the PTV which are similar to those used for PBI at conventional linac. This was done in order to investigate the feasibility

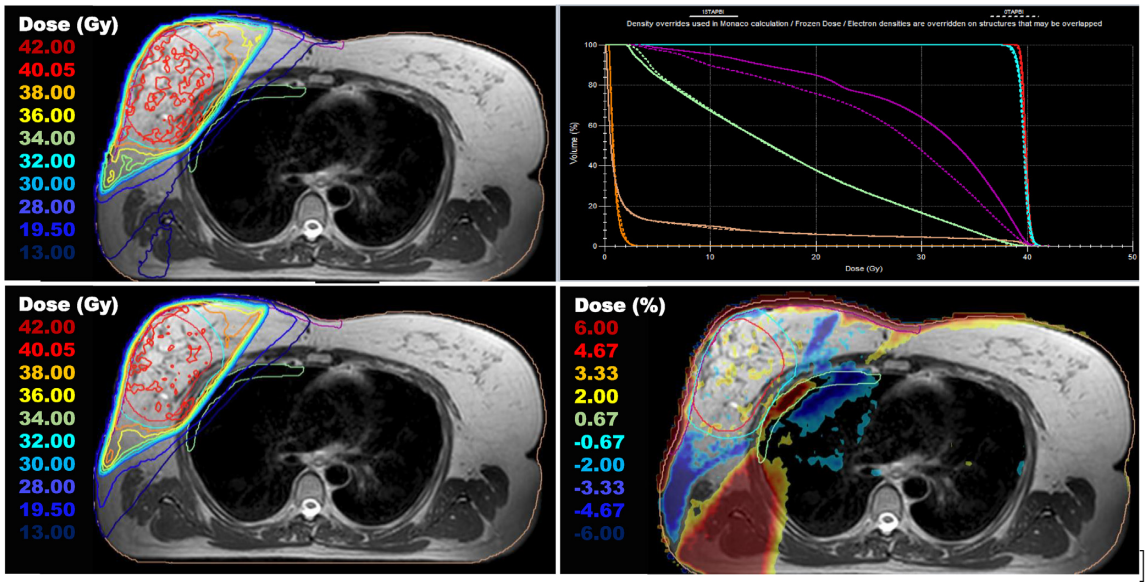

Figure 25: Comparison of the dose distribution in the simulated plans in the presence of the 1.5 T magnetic field (upper left) and without magnetic field (0 T, lower left). The dose volume histograms of the two plans (upper right, solid line with magnetic field, dotted line without magnetic field). For visualisation purpose the 6% of the dose (6% of 29.8 Gy, the maximum dose difference) is displayed as maximum dose difference (dark red). The values of the dose difference on the skin and the chest wall are described in the text. (For interpretation of the references to colour in this figure legend, the reader is referred to the web version of this article.)

and safety of the treatment at MR linac as well as the ERE and ESE in comparable conditions to the standard treatment at a conventional linac. Nevertheless, the MR planning and especially the MR daily imaging and plan adaption open to future opportunities such as margin and fraction number reduction as well as novel treatment paradigms such as single dose neoadjuvant PBI [31]. Regarding adjuvant PBI, benefits are represented by a better visualization of the postoperative tissue changes and, if needed, modify the target volume on the basis of anatomic changes (e.g. seroma, breast swelling). Regarding neoadjuvant treatments, important advantages are represented by a better tumour visualization (e.g. tumor extent and edges), the possibility to adapt the treatment daily especially on the basis of changes in the target (e.g. target shrinkage) and the possibility to track the tumour position

during treatment with real time MR imaging. Altogether, we demonstrated that a PBI with the 1.5 T MR-linac is feasible and that ESE is accurately calculated by the TPS, can be effectively reduced with a 1 cm bolus and is comparable to dose from CBCT guided PBI. Moreover, dose from ERE appears to be low and not associated with an increased risk of acute of toxicity.

Supplementary Material

The supplementary material of the publication is depicted in the supplementary material of the dissertation at section 9.5.

3 Discussion

In the context of this dissertation, the challenges of MRgRT have been successfully investigated troughout several steps of implementation into clinical radiotherapy. During step-wise implementation of MRgRT a number of technical and dosimetric drawbacks were investigated, novel quality assurance systems for safe and fast patient treatments developed and consequently first patient treatments executed and their prospects evaluated.

In the first investigative step, the initial drawbacks show clear differences to a conventional accelerator system, which limit treatment quality on the current technical implementation. Following this investigation on technical drawbacks, a secondary extensive dose calculation system has been designed, verifying that the additional complexity of the hybrid MR-linac system design is modeled correctly.

For the clinical implementation of MRgRT quality assurance systems and workflows were developed, since neither the dosimetric equipment was designed to work in magnetic field nor adaptive radiotherapy has ever been enabled to such extend. Therefore a novel workflow for the experimental verification of simulated dose distribution, as they are calculated by the prior verified dose algorithm, has been developed. As an experimental measurement can not be part of an online adaptive workflow, an additional system was developed to validate online calculated treatment plans while the patient is being treated.

After these prior investigations and developed quality assurances, the thesis concluded in treatment of patients of multiple tumor entities with online adaptive MR-guided Radiotherapy. At this final endpoint different tumor entities were treated and the perspective of additional clinical value evaluated.

3.1 Investigation of challenges related to the hybrid hardware design

In the first objective [133] we investigated the differences between a state of the art modern linear accelerator and a research prototype MR-linac system in a planing study.

The primary tumor entity investigated in this study was esophageal tumor, as MRgRT exhibits high potential in treatment, but as well anticipated drawbacks. Whereas the prospective value of treating this entity with MRI was based on increased differentiation of tumor tissue and therefore possible increase in TCP, the disadvantages were considered the high probability of magnetic field effects on the multitude of air-tissue interfaces. Up to this point no study was published identifying such differences in dose distributions of MRgRT for esophageal cancer.

In this simulation study, twelve esophageal cancer patients were analysed. In the framework of a standardized optimization a special developed beam angle detection for the MR-linac plans and optimal unbiased dose distributions for both systems were generated and their dosimetric parameters compared. For a characterization of magnetic field effects, the skin as well as the lung fringe have been analysed and the dose increases characterized. In addition to organ at risk (OAR) dose-volume-parameters, conformality parameters were characterized and additional dose to tissue cranio-caudally of the primary target were analysed.

Within the study it was shown, that the MR-linac system exhibits drawbacks in comparison to the standard linac. As a first drawback two patients had to be excluded as a caudal-cranial size limitation on the MR-linac system is present. This limitation on treatment size prohibits treatment of target volumes with a length greater than 18 cm and consequently limits the treatability of further tumor entities such as sarcoma and cervical patients. The dosimetric results showed, that clinical dose constraints could be met allowing clinical feasibility. However, OARs which did already experience low doses and corresponding low complication probabilities did encounter more dose with the MR-linac system. Consequently, on the MR-linac greater focus has to be put on low and middle dose ranges and conventional low priority OARs included in optimization.

This is the first work characterizing the difference in dose distribution for esophageal cancer to a state of the art linear accelerator. For the highly respiratory influenced

lung cancer Bainbridge et al.[14] published the potential benefit of MR-guided treatments of lung cancer in comparison to a standard linac. Bainbridge et al. proposed, that the drawbacks of the system can be compensated for by reduction of margins. Whereas the reduction of margins is a potential benefit of the improved soft tissue contrast or potential respiratory gating, no corresponding published data is so far available.

Liu et al. [109] has further investigated the possible influence of ESE for esophageal cancer showing an additional dose increase on the skin surface in the cranial direction. Whereas additional caudal-cranial dose was characterized in our paper, an maximal dose increase of in average 6.5 Gy, as showed by Li et al., was not noted. This can be due to the different tumor locations or as a result of different optimizations.

Until may 2021 no esophageal cancer patient was treated in Tuebingen, due to the dominant magnetic field effects for esophageal cancer in concurrence with the loss in conformality and only one center worldwide has started respective treatments on the 1.5 T MR-linac system [104]. However, due to these findings the focus on plan evaluation and optimization in comparison to conventional systems was changed. On the hybrid system greater emphasis has to be put on low dose areas and organ at risk (OAR) must be taken into optimization, which did not need to be explicitly accounted for in conventional systems.

3.2 Simulation of energy dose deposition in the presence of a magnetic field

In the second study [53] the dose calculation in the presence of the magnetic field was investigated. Whereas a GPU based Monte Carlo (MC) algorithm is available (GPUMCD), clinical simulations apply approximations for a calculation of dose distributions in a matter of minutes.

The clinical XVMC dose calculations, on which the code is based on, neglect stopping radiation from secondary electrons and are conventionally using phase space files located after the beam accelerator head [52]. However, at a MR-linac system, a cryostat is located between the accelerator head and the patient surface. This additional scatter material, mainly helium and aluminium, differ in terms of their

interaction with radiation compared to human tissue. This introduces incorrect interaction probabilities for the clinical XVMC, as this exploits water cross sections as basis for the calculation. Whereas this GPUMCD algorithm has been evaluated based on rectangular fields and on experimental measurements, a detailed validation of the implemented dose calculation algorithm in combination with the magnetic field did not exist before.

Therefore, we verified the GPUMCD algorithm, by building a independent accelerator head in the full Monte Carlo framework EGSnrc [53]. Based on construction details, supplied by Elekta for the accelerator head and by Philips for the MRI system all materials and dimensions of the system were taken into account. However, a linear accelerator system has three free variables, which are calibrated on installation of the system and therefore did not present fixed values. For the derivation of electron energies, energy distributions and the geometric spot sizes of the primary electron beam, we varied these within a set of simulations and compared the resulting dose distributions to experimental data. The best possible combination of primary parameters confirmed by the measured experimental data was selected for the EGSnrc based accelerator head model. Based on this model a clinical dose distribution of a prostate patient treatment was recalculated and the differences to the vendor supplied algorithm investigated.

This is the first work validating the GPUMCD in clinical plans by incorporating the magnetic field effect and fully modelling the accelerator head. The model presents very good agreement on the percentage depth-dose with a gamma passing rate [2 mm/2 %] of 100 % as well as an average output factor deviation 0.6 %. However, the comparison of profiles showed greater deviation to measured data with a gamma passing rate [2 mm/2 %] for the crossplane of 100 % and for the inplane profile of 90.8 % at a field size of $22 \times 22\, cm^2$. This deviation is due to small differences on the penumbra as most likely the diaphragm position between systems were specified differently. Whereas the agreement of profiles was better for smaller fields, the deviation increased for bigger field sizes. This could be due to limitations of modeling curved structures in EGSnrc. In the published model all attenuating materials were positioned orthogonal to the beam direction, and therefore did not exhibit greater attenuation when irradiating trough the curved structure of the MRI at big field sizes.

The recalculation of the patient treatment showed a good validation between the two systems with a gamma passing rate of 97.77 %, evaluating every voxel surpassing 40 % of the maximal dose. However, slight differences were visible at the definition

of table materials, which showed greater dose in the clinical TPS than EGSnrc, as EGSnrc models cross sections of material differentiating to tissue more exact. Additionally field edges of individual segments differed slightly between the two systems. This might be due to difference in MLC- or diaphragm-positioning or due to the necessity of two different patient models. Every MC system needs a discrete voxel-grid to calculate and the two different methods for the systems slightly differ in their respective discretization of voxel centers and dimensions. Whereas this corresponds to sub-millimeters between voxels, these slight differences can present big dose changes within a gradient.

Consequently the vendor supplied algorithm was verified with the independent head model. In this work not only the high dose area could be verified but also the low dose areas were reproducibly calculated between the two systems. This verifies that the approximation, implemented in GPUMCD in regard to secondary generated photons and the additional scattering within the cryostat, did not significantly change the dose distribution.

The recalculation of clinical dose depositions within EGSnrc took half a day on a dedicated Cluster, running on $4 \cdot 10^6$ histories in 40 parallel jobs for each segment. Whereas, this was still a multitude of times greater than clinical algorithms serveral research groups have implemented algorithms speeding up this process, that calculation could be executed in time periods equivalent to today's MC systems [192].

Although this MC model can not be used for optimization of treatment plans, the flexibility combined with the possibility to simulate phantom material, based on their composition, has already been implemented in a multitude of different investigations. Pojtinger et al. [142] used this model to correctly simulate the magnetic field effect in ionization chambers, as air-filled chambers detect more signal, when they are being irradiated in the presence of a magnetic field. Additional research topics of the designed system included the correct detection of effective points of measurement, detailed tracking of electron exhibiting the electron stream effect (ESE), and dose calculation based on artificial intelligence. These investigations rely on research MC systems without approximations and a variable framework.

3.3 Online and offline quality assurance for adaptive MRgRT

For investigations related to online [132] and offline experimental [126] quality assurance, we focused on developing and evaluating the safe patient treatments at the MR-linac system.

While for conventional systems, the quality assurance has been developed and specified over decades, the quality assurance of an online adaptive workflow in the presence of an magnetic field must derive from these standards. Prior to this study, the primary focus of quality assurance publications in MRgRT was on the detection and characterization of the magnetic field influence on ionization chambers in respect to the chamber type and orientation allowing a correct calibration of absolute dose [140, 165].

Therefore two distinct topics of quality assurance in MRgRT were investigated. In the first study [126] we investigated the experimental verification of patient treatment dose distributions with a 2D ionization chamber array and in the second step a method for the online verification of newly optimized treatment plans, while the patient is on the table, was developed.

The experimental verification of dose distributions using a 2D ionization chamber array is a critical clinical used routine quality assurance method for verification of machine parameters. In this concept clinical used machine parameter setups, pre-optimized for patient specific treatments, are irradiated at a phantom, equipped with a chamber array, detecting a multitude of dose points. This measured dose distribution is then compared to a simulated dose distribution in the defined phantom, using a gamma analysis, allowing for small uncertainties in setup and dose with a distance- and dose-to-agreement factor. This comparison assures, that simulated dose distributions are correctly calculated and that the linear accelerator is capable to deliver the machine specifications, as they were optimized. Based on these two main uncertainties treatment plans can be characterized as applicable or system parameters need to be adjusted.

Whereas in clinical practice experimental treatment verification is usually performed in different phantoms, magnetic field effects did not allow the conventional setups as these contained ferromagnetic materials. Additionally, used dose calibrations were not incorporating deflected secondary electrons, which changed dose deposition dependencies in an air filled ionization chamber array.

In this work a novel optimized workflow for a correct measurement of dose distributions was developed. A characterization of gantry angle dependencies of a chamber array was investigated. This consisted of investigations on a modified phantom in different orientations and the identification of a corresponding lookup table. Using this characterization 106 treatment plans were experimentally evaluated and the detected results investigated. Based on the results, recommendations were published for measurements in a 1.5 Tesla MR-linac system [126].

The investigation showed that ion chamber calibrations supplied by the vendor can not be used in the magnetic field due to the influence of the Lorentz force on secondary electrons. In addition, an anisotropic dependency of the array was visible, which is, in our hypothesis, caused by the electron return effect (ERE) in air cavities within the ionization chambers. The developed method showed additional value based on its flexibility, allowing for dispositioning and measurements of dose distributions lateral to the central axis and consequently verification of dose distributions of non central tumor locations.

The proposed method presents with limitations on large target areas, which could not be fully verified based on the size of the phantom and limited orientation on a hexagonal setup. In addition, the developed method is time consuming as human interactions, for rotating the phantom, based on the gantry angle, were needed. In a conventional setting this manual work could be reduced by positioning of the chamber array on a rotating system, which allows for a consistent orthogonal orientation towards the treatment head. However, for the usage of such system, no rotating platform without ferromagnetic materials and, therefore, compatibility with the magnetic field was available. Future improvements on this system consist of the integration of newly developed liquid instead of air filled ionization chamber arrays, which consequently limit incorrect dose measurement due to ERE effects. The hypothesis of anisotropic dependency must be investigated in more complex simulations, as this dependency would still be present, even if the detector rotates with the treatment head. However, for this simulations, the technical information on the chamber array needs to be supplied by the vendor for an individual tracking of electron paths.

In the second study on quality assurance, a software tool was developed to validate optimized machine parameters in an adapted online treatment, while the patient is on the table, and before patient irradiation. Whereas no comprehensive system for adaptive radiotherapy is available, a new system was designed from the ground up and installed in a clinical treatment workflow.

To this point and the du to the necessity of a validation system, several groups have investigated and implemented different methods for an independent dose verification. In a lowest complexity Kaas et al. [87] considered a correlation of the number of segments and monitor unit (MU) between a reference plan and the daily optimization. In a more sophisticated system a secondary point dose recalculation was employed, which calculates one single dose point within the patient and compares it to the online calculated value [203, 204]. Only Intven et al. [81] considered a full recalculation in a secondary dose calculation system with the comparison to the online dose based on predefined metrics and tolerance levels.

However, based on experiences of prior patient studies, we concluded that this simplified methods were due to the variability of MU and segments not suitable for extensive analysis. Therefore for a check of errors in density assignments, registrations and dose calculation parameters an independent simulation of the proposed dose distribution on the patient anatomy is needed.

To independently calculate these, a treatment head model of the in-house developed Monte Carlo algorithm replicating the MR-linac system was designed. This head model was defined based on measured beam data and installed in a programmed automatic workflow allowing for an independent online secondary dose check. Prior to the final clinical implementation, the secondary dose calculation was validated by comparison of the treatment head model to experimental base data, a evaluation within a simplified phantom and by comparison of secondary dose check of patients to their respective experimental data [132].

This was the first publication describing a developed workflow for 3-D verification of dose distributions in online adaptive radiotherapy. We showed the potential of 3D secondary dose calculation (3D-SDC) in adaptive radiotherapy, allowing extensive quality assurance even in the presence of limited time.

The developed treatment head was able to reproduce base data accurately, even though the currently used algorithm does not include magnetic field effects. The non inclusion of magnetic field effects was based on the hypothesis that, since the Lorentz force is depended on the direction of velocity, the magnetic field effect of opposed beams cancel each other out. Therefore in the high dose area, the dose distribution of a multiple beam IMRT should be independent of the magnetic field.

This hypothesis was validated in the second step, in which we showed that given certain circumstances, the magnetic field effect within a simulation is minimal. This

appears to be more relevant on target areas, which are in proximity to air-tissue interfaces and irradiated from multiple beam angles. In correspondence the developed workflow validated in the third step dose distribution for tumor entities fulfilling the given dependencies. For rectal cancer the 3D-SDC showed significant better results than the respective experimental measurements. However for entities such as head and neck and breast cancer the comparison were significantly worse. For these treatment sites we recommend an more extensive workflow, in which a experimental reference should be taken into account.

Whereas other groups have executed prior studies on a simplified single dose point verification [61] or on the feasibility of using a kernel based dose simulation in an online workflow [107], this paper was the first one elaborating on a developed 3D-SDC system implemented in a clinical workflow. However with further complexity of treatment plans this system needs to include the magnetic field effect in the MC calculation to no longer rely on simplified assumptions as well as for an exacter dose representation and consequently stricter possible passing criteria. In addition with improving annotation and optimization steps within the MRgRT workflow the calculation- and validation- speed of the secondary dose calculation needs to be improved as well. Further investigations on this behalf should incorporate live calculation by the inclusion of artificial intelligence, to be capable to validate optimizations calculated during patient treatments [95].

These quality assurance workflows are employed at the MR-linac system in Tuebingen for a safe radiation of online adaptive MRgRT and could be adapted in other centers thanks to the published data.

3.4 MR-guided radiotherapy on the hybrid system

In the final step of clinical implementation we have translated the investigated limitations, characterizations and developed methods in a safe irradiation of patients on the MR-linac system. With this primary endpoint novel patient treatments were applied in a step wise and developing process to a multitudes of different tumor locations and entity specific research questions investigated [10, 25, 56, 58, 118, 131].

In a recently published work [131] we reported the worldwide first treatment of partial breast on the MR-linac system and investigated the entity specific magnetic field effects, which potentially limited breast treatments. Due to a high number of targeted normal tissue structures, the potential to increase the quality of live (QOL) by clearer visualization during treatment [63] and the possibility for extreme hypofractionation up to a single fraction in an neoadjuvant setting, breast cancer is a widely discussed tumor location for treatment on the MR-linac.

However, the proximity to air-tissue interfaces such as skin and lung fringe, as well as the lateral orientation within the static magnetic field yield complications in the hybrid setting. The lateral position of the tumor position causes a less homogeneous magnetic field due to the increased distance to the MR-isocenter. This inhomogeneity can result in potential spatial distortion and, if targeted based on these, in a wrong treated position. An additional drawback for breast cancer treatments is the specific tumor position in relation to the table, preventing usage of favourable treatment angles. These angles are yielding at the given system high uncertainties in dose calculation, due to the specific materials used in the treatment table. Further drawback are the electron return effect (ERE), increasing potential dose at the skin of the patient and the for breast cancer dominant electron stream effect (ESE). This electron stream leads unhandled to medium and low dose irradiation of a anatomical points outside of the target, as for breast cancer on the chin of the patient.

We demonstrated the feasibility of partial breast treatments on the MR-linac system, if the magnetic field effects are correctly taken into account. With an adapted treatment planning, with respect to beam angles and optimization, it was possible to generate a comparable treatment plan quality in terms of critical dose volume parameters and electron return effect. However, on the specific evaluation of the electron return effect an increase of skin dose due to the magnetic field was identified. Whereas a relative skin volume of 40.2 % receives 35 Gy in the presence of the magnetic field, without the magnetic field this only correspond to 24.9 %. However,

even tough this medium dose range increased due to the magnetic field, the high dose parameters, which correspond to side effects on the skin [180] did not substantially increase. In a simulated plan without the magnetic field the near maximum dose $D_{2\%}$ showed a value of 39.7 Gy, whereas this value increased 0.3 Gy to 40 Gy with the inclusion of the magnetic field.

For a reduction of the electron stream effect (ESE), a 1 cm bolus material was applied on to the chin as the primary organ at risk and experimental film measurements executed on top and under the bolus. The additional attenuation of the respective bolus in this setting was simulated showing a decrease of the dose to the chin from 2.6 Gy to 0.72 Gy and verified with the measurements. A visible check of the geometric distortion was executed by aligning the daily MRI to the spatial absolutely correct CT assuring minimal differences.

Based on our results in this study [131], further experimental measurements were executed, verifying our findings [40] and the general application of a bolus for the treatment of breast cancer was recommended [63]. Whereas we could verify the correct dose simulation in regard to the ESE, the pathways of electrons are not clear and need to be simulated in more detail.

Even though we showed that geometric distortion for partial breast was not visible, further investigation need to be executed, if a treatment should be fully independent of a CT and if smaller margin should be employed. Additional improvements are better simulations of dose attenuation of the treatment table, improving plan quality and consequently irradiation of healthy tissue.

3.5 Conclusion

In this work the medical physics basis for the novel treatment of patients with MR-guided radiotherapy (MRgRT) was developed. In simulation studies the expected drawbacks and potential pitfalls were demonstrated, which must be taken into account for treatments. With an exact research Monte Carlo investigation the approximations of the clinical algorithm were analysed, showing small, for patient treatment insignificant, differences. New quality assurances workflows were developed, allowing experimental measurements in the presence of the magnetic field as well as online extensive checks within the adaptive workflow. Consequently with the inclusion of these works, as one of the first centers worldwide, patients were treated with MR-guided radiotherapy (MRgRT) and the respective magnetic field effects analysed.

These first partient treatments were practiced concurrent to clinical practice with a focus on safety and analysis of possible uncertainites. This process lead to a treatment of almost all tumor entities within radiotherapy and an analysis of the respective magnetic field effects as well as comparative analysis against conventional CT based approaches. Within these, even though clinical concepts were not changed, an additional dosimetric value of MRgRT was present by exacter daily application of dose leading to smaller toxicities for normal tissues. In addition novel tumor entities, such as small lymph node metastases next to sensitive OARs or liver metastasis were treated due to the increased visibility.

However, as methods are now developed and the magnetic field effects investigated, new clinical concepts are being developed starting the next phase of MRgRT, improving patient treatments in radiotherapy by deviating from current clinical practice.

4 Summary

The advances in image guided radiotherapy (IGRT) lead to an significant increase in treatment quality of cancer patients. However the guidance of radiotherapy based on X-Ray shows limitations and never translated into online adaptive radiotherapy.

Therefore the new concept of MR-guided radiotherapy (MRgRT) was introduced, combining an linear accelerator with a magnetic resonance imaging (MRI). In this hybrid MR-linac system the higher soft tissue contrast of the MRI in combination with an optimization on the anatomy of the day promises increased treatment quality and new standard of practice.

However, a MRI has before only supplied additional offline information for the annotation of tumor tissue and an online adaptive workflow was not part of clinical treatments. Therefore the challenges in regard to the magnetic field effect on dose distributions, algorithms and measurement devices as well as the problems due to the online adaptive workflow have not been investigated.

In this work, the medical physics basis of MR-guided radiotherapy (MRgRT) was researched and concluded in safe clinical treatments of patients.

In a first step the technical drawbacks were researched in a simulation study comparing the possible dose distribution for esophageal cancer between the MR-linac system and a modern state of the art linear accelerator. This simulation study showed the dosimetric drawbacks of the MR-linac system due to loss of conformality and size limitations. In addition we showed, that greater focus has to be put on mid- and low-dose areas and that the corresponding OARs must be included into optimization. However, we showed as well that by adaptation of the optimization, the clinical parameters can be fulfilled leading to feasibility of treatment plans.

In a second step the only existing algorithm for calculation of dose distributions at the 1.5 T MR-Linac was compared to a detailed research Monte Carlo (MC) system, due to possible approximations on behalf of the magnetic field and attenuating layers of the MRI. In this investigation the detailed MC-simulation was designed

to incorporate the material specific information of the accelerator and MRI and their corresponding cross sections for an exact dose calculation. With an iterative comparison to experimental data the linac specific free parameters were derived and the independent accelerator head model finalized for a validation of patient treatments. This validation showed, with gamma criterion of 3 mm and 3% a passing rate of 99.83 % and therefore validated that the approximations do not correspond to a significant change in dose distribution.

In a third step new quality assurances were developed to allow treatment of patients on the MR-linac system. For an experimental measurement of dose deposition a novel workflow was developed and integrated, as the conventional systems showed high influences by the static magnetic field. Based on the characterization, a 2D ionization chamber inside a hexagonal phantom can accurately measure the applied dose and, by comparison with the respective simulation, assure correct machine calibration.

For an comprehensive check of online adaptive plans within a treatment workflow an independent secondary dose calculation was established. Based on an independent build Monte Carlo accelerator head and a 3D comparison of dose distributions this secondary dose calculation can verify clinical plans in a median time of 1:23 min. In this comparison of dose distributions a gamma criterion validates the machine parameters and assures correct dose over the full patient anatomy.

In the final step the acquired knowledge from the previous studies and developed quality assurances allowed first treatments of patients with online adaptive MR-guided radiotherapy. In this dissertation the first worldwide MR-guided treatment of partial breast stands representative to the multitude of different tumor entities initiated at the MR-linac system. Equivalent to the investigations on ERE, ESE and geometric distortion in partial breast, further tumor specific magnetic field effects were evaluated for an assessment of potential risks.

With this work the basis for a safe treatment with MR-guided radiotherapy (MRgRT) was developed. Therefore, as methods and respective handling of magnetic field effects are now established, new clinical concepts are being developed starting the next phase of MRgRT improving patient treatments in radiotherapy by deviating from current clinical practice.

5 Zusammenfassung

Die Fortschritte in Bildgestützter Strahlentherapie (IGRT) haben zu einer signifikanten Verbesserung der Behandlungsqualität für Krebspatienten in der Strahlentherapie geführt. Jedoch sind klare Limitationen bei der Strahlführung auf Grundlage von Röntgenstrahlung vorhanden und ein Übertrag dieser Methode in ein online adaptives Setting wurde niemals ausgeführt.

Daher wurde das neue Konzept der Magnetresonanz-geführten Strahlentherapie (MRgRT) eingeführt, welches einen Linearbeschleuniger mit einem Magnetresonanztomograf (MRT) kombiniert. Bei diesem hybriden MR-Linac-System verspricht der erhöhte Weichteilkontrast des MRTs in Kombination mit dem Potential für eine Behandlugsoptimierung auf die Anatomie des Tages eine gesteigerte Behandlungsqualität und einen neuen klinischen Standard.

Jedoch wurde bisher durch ein MRT nur offline Informationen für die Annotation von Tumorgewebe geliefert und ein online adaptiver Workflow war nie Teil der klinischen Behandlung. Daher wurden bisher die Herausforderungen der Magnetfeldeinwirkung auf Dosisverteilungen, Algorithmen und Messgeräte sowie die Probleme durch einen adaptiven Online Workflows nicht untersucht.

In dieser Arbeit wurde der medizin-physikalische Hintergrund von Magnetresonanzgeführten Strahlentherapie erforscht, welches zu einer sicheren klinische Behandlungen von Patienten führte.

In einem ersten Schritt wurden die technischen Nachteile in einer Simulationsstudie untersucht, bei welcher die möglichen Dosisverteilungen für Speiseröhrenkrebs zwischen dem MR-Linac-System und einem modernen Linearbeschleuniger verglichen wurden. Diese Simulationsstudie zeigte die dosimetrischen Nachteile des MR-Linac-Systems aufgrund von Konformitätsverlust und Größenbeschränkungen. Darüber hinaus wurde gezeigt, dass ein stärkerer Fokus auf mittlere und geringe Dosisbereiche gelegt werden muss und die entsprechenden Risikostrukturen in die Optimierung

miteinbezogen werden müssen. Wir haben jedoch ebenfalls gezeigt, dass durch Anpassung der Optimierung die klinischen Parameter erfüllt werden können und somit klinisch durchführbare Behandlungen möglich sind.

In einem zweiten Schritt wurde der einzig vorhandene Algorithmus für den 1.5 T MR-Linac zur Berechnung von Dosisverteilungen mit einem detaillierterem Forschungs-Monte Carlo (MC) System verglichen um die möglichen Vereinfachungen im Hinblick auf das Magnetfeld und die abschwächenden Bestandteile des MRT zu analysieren. In dieser Untersuchung wurde eine detaillierte MC-Simulation entworfen, um die materialspezifischen Informationen des Beschleunigers und des MRTs mit deren entsprechenden Wirkungsquerschnitte für eine genaue Dosisberechnung einzubeziehen. Durch einen iterativen Vergleich mit experimentellen Daten wurden die Linac-spezifischen freien Parameter abgeleitet und das unabhängige Beschleunigerkopfmodell zur Validierung von Patientenbehandlungen finalisiert. Diese Validierung zeigte mit einem Gammakriterium von 3 mm und 3 % eine Akzeptanzrate von 99,83 % und bestätigte damit, dass die Näherungen zu keiner signifikanten Änderung der Dosisverteilung führen.

In einem dritten Schritt wurden neue Qualitätssicherungsmethoden entwickelt, um die Behandlung von Patienten an dem MR-Linac-System zu ermöglichen. Für eine experimentelle Messung der Dosisdeposition wurde ein neuartiger Workflow entwickelt, da die konventionellen Systeme stark von dem statischen Magnetfeld beeinflusst werden. Basierend auf der entwickelten Charakterisierung kann mit einem 2D-Ionisationskammerarray in einem hexagonalen Phantom die applizierte Dosis genau gemessen und, im Vergleich mit der entsprechenden Simulation, eine korrekte Maschinenkalibrierung sichergestellt werden.

Um eine umfassende Überprüfung von online adaptiven Plänen innerhalb einer Behandlung zu ermöglichen wurde eine unabhängige sekundäre Dosisberechnung erstellt. Basierend auf einem unabhängig entwickelten Monte Carlo Beschleunigerkopf und einem 3D-Dosisvergleich kann diese sekundäre Dosisberechnung klinische Pläne in einer medianen Zeit von 1:23 min verifizieren. Bei diesem Vergleich der Dosisverteilungen validiert ein Gamma-Kriterium die Maschinenparameter und gewährleistet eine korrekte Dosisverteilung über die gesamte Patientenanatomie.

Im letzten Schritt ermöglichten die gewonnenen Erkenntnisse aus den vorangegangenen Studien und die entwickelten Qualitätssicherungsmethoden erste Behandlungen von Patienten mit online adaptiver MR-geführter Strahlentherapie.

In dieser Dissertation steht die weltweit erste MR-geführte Behandlung der Teilbrust stellvertretend für die Vielzahl an unterschiedlicher Tumorentitäten, welche am MR-Linac-System etabliert wurden. Äquivalent zu den Untersuchungen von ERE, ESE und geometrischer Verzerrung bei der Behandlung der Teilbrust, wurden weitere tumorspezifische Magnetfeldeffekte zur Abschätzung potenzieller Risiken evaluiert.

In dieser Arbeit wurde die Grundlage für eine sichere Behandlung mit MRgRT geschaffen. Daher, da nun die Methoden und der Umgang mit Magnetfeldeffekten spezifiziert wurden, können neue klinische Konzepte entwickelt werden, um die nächste Phase der MRgRT zu starten, bei welcher, für eine Verbesserung der Patientenbehandlung, von dem aktuellen klinisches Standard abgewichen wird.

Ort, Datum, Unterschrift Prof. Dr. rer. nat. Daniela Thorwarth

6 Publications related to the dissertation

1. Comparison of treatment plans for a high-field MRI-linac and a conventional linac for esophageal cancer

   M. Nachbar, D. Mönnich, P. Kalwa, D. Zips, D. Thorwarth and C. Gani

   Strahlentherapie und Onkologie 2019 Vol. 195 Issue 4 Pages 327-334

2. Development and validation of a 1.5 T MR-Linac full accelerator head and cryostat model for Monte Carlo dose simulations

   M. Friedel, **M. Nachbar**, D. Mönnich, O. Dohm and D. Thorwarth

   Med Phys 2019 Vol. 46 Issue 11 Pages 5304-5313

3. Quality assurance of IMRT treatment plans for a 1.5 T MR-linac using a 2D ionization chamber ar-ray and a static solid phantom

   D. Mönnich, J. Winter, **M. Nachbar**, L. Künzel, S. Boeke, C. Gani, O. Dohm, D. Zips and D. Thorwarth

   Physics in Medicine & Biology 2020 Vol. 65 Issue 16 Pages 16NT01

4. Partial breast irradiation with the 1.5 T MR-Linac: First patient treatment and analysis of electron return and stream effects

   M. Nachbar, D. Mönnich, S. Boeke, C. Gani, N. Weidner, V. Heinrich, M. lo Russo, L. Livi, J. Winter, S. Tsitsekidis, O. Dohm, D. Thorwarth, D. Zips and C. De-Colle

   Radiotherapy and Oncology 2020 Vol. 145 Pages 30-35

5. Experimental determination of magnetic field correction factors for ionization chambers in paral-lel and perpendicular orientations

   S. Pojtinger, **M. Nachbar**, S. Ghandour, O. Pisaturo, M. Pachoud, R.-P. Kapsch and D. Thorwarth

   Physics in Medicine & Biology 2020 Vol. 65 Issue 24 Pages 245044

6. Influence of beam quality on reference dosimetry correction factors in magnetic resonance guid-ed radiation therapy

   S. Pojtinger, **M. Nachbar**, R.-P. Kapsch and D. Thorwarth

   Physics and Imaging in Radiation Oncology 2020 Vol. 16 Pages 95-98

7. Quantitative magnetic resonance imaging on hybrid magnetic resonance linear accelerators: Per-spective on technical and clinical validation

   D. Thorwarth, M. Ege, **M. Nachbar**, D. Mönnich, C. Gani, D. Zips and S. Boeke

   Physics and Imaging in Radiation Oncology 2020 Vol. 16 Pages 69-73

8. Prospective Image Quality and Lesion Assessment in the Setting of MR-Guided Radiation Therapy of Prostate Cancer on an MR-Linac at 1.5 T: A Comparison to a Standard 3 T MRI

   H. Almansour, S. Afat, V. Fritz, F. Schick, **M. Nachbar**, D. Thorwarth, D. Zips, A.-C. Müller, K. Niko-laou, A. E. Othman and D. Wegener

   Cancers 2021 Vol. 13 Issue 7 Pages 1533

9. 1.5 T MR-linac planning study to compare two different strategies of rectal boost irradiation

   P. Bonomo, M. Lo Russo, **M. Nachbar**, S. Boeke, S. Gatidis, D. Zips, D. Thorwarth and C. Gani

   Clinical and Translational Radiation Oncology 2021 Vol. 26 Pages 86-91

10. Initial Feasibility and Clinical Implementation of Daily MR-Guided Adaptive Head and Neck Can-cer Radiation Therapy on a 1.5T MR-Linac System: Prospective R-IDEAL 2a/2b Systematic Clinical Evaluation of Technical Innovation

    B. A. McDonald, S. Vedam, J. Yang, J. Wang, P. Castillo, B. Lee, A. Sobremonte, S. Ahmed, Y. Ding, A. S. R. Mohamed, P. Balter, N. Hughes, D. Thorwarth, **M. Nachbar**, M. E. P. Philippens, C. H. J. Ter-haard, D. Zips, S. Böke, M. J. Awan, J. Christodouleas and C. D. Fuller

    International Journal of Radiation Oncology*Biology*Physics 2021 Vol. 109 Issue 5 Pages 1606-1618

11. Analysis of the electron-stream effect in patients treated with partial breast irradiation using the 1.5 T MR-linear accelerator

    C. De-Colle, **M. Nachbar**, D. Mönnich, S. Boeke, C. Gani, N. Weidner, V. Heinrich, J. Winter, S. Tsitsekidis, O. Dohm, D. Zips and D. Thorwarth

    Clinical and Translational Radiation Oncology 2021 Vol. 27 Pages 103-108

12. Marker-less online MR-guided stereotactic body radiotherapy of liver metastases at a 1.5 T MR-Linac - Feasibility, workflow data and patient acceptance

    C. Gani, S. Boeke, H. McNair, J. Ehlers, **M. Nachbar**, D. Mönnich, A. Stolte, J. Boldt, C. Marks, J. Winter, L. A. Künzel, S. Gatidis, M. Bitzer, D. Thorwarth and D. Zips

    Clinical and Translational Radiation Oncology 2021 Vol. 26 Pages 55-61

13. First experience of autonomous, un-supervised treatment planning integrated in adaptive MR-guided radiotherapy and delivered to a patient with prostate cancer

    L. A. Künzel, **M. Nachbar**, M. Hagmüller, C. Gani, S. Boeke, D. Zips and D. Thorwarth

    Radiotherapy and Oncology 2021 Vol. 159 Pages 197-201

14. Automatic 3D Monte-Carlo-based secondary dose calculation for online verification of 1.5 T magnetic resonance imaging guided radiotherapy

    M. Nachbar, D. Mönnich, O. Dohm, M. Friedlein, D. Zips and D. Thorwarth

    Physics and Imaging in Radiation Oncology 2021 Vol. 19 Pages 6-12

15. A novel approach for radiotherapy dose escalation in rectal cancer using online MR-guidance and rectal ultrasound gel filling – Rationale and first in human

    C. Gani, M. Lo Russo, S. Boeke, D. Wegener, S. Gatidis, S. Butzer, J. Boldt, D. Mönnich, D. Thorwarth, K. Nikolaou, D. Zips, **M. Nachbar**

    Radiotherapy and Oncology 2021 Vol. 164 Pages 37-42

7 References

[1] S. Acharya, B. W. Fischer-Valuck, R. Kashani, P. Parikh, D. Yang, T. Zhao, et al., Online Magnetic Resonance Image Guided Adaptive Radiation Therapy: First Clinical Applications, International Journal of Radiation Oncology*Biology*Physics 94 (2) (2016) pp. 394–403, DOI: https://doi.org/10.1016/j.ijrobp.2015.10.015.

[2] S. Acharya, B. W. Fischer-Valuck, T. R. Mazur, A. Curcuru, K. Sona, R. Kashani, et al., Magnetic Resonance Image Guided Radiation Therapy for External Beam Accelerated Partial-Breast Irradiation: Evaluation of Delivered Dose and Intrafractional Cavity Motion, International Journal of Radiation Oncology*Biology*Physics 96 (4) (2016) pp. 785–792, DOI: https://doi.org/10.1016/j.ijrobp.2016.08.006.

[3] S. B. Ahmad, A. Sarfehnia, M. R. Paudel, A. Kim, S. Hissoiny, A. Sahgal, et al., Evaluation of a commercial MRI Linac based Monte Carlo dose calculation algorithm with GEANT4, Med Phys 43 (2) (2016) pp. 894–907, DOI: 10.1118/1.4939808.

[4] S. B. Ahmad, A. Sarfehnia, M. R. Paudel, A. Kim, S. Hissoiny, A. Sahgal, et al., Evaluation of a commercial MRI Linac based Monte Carlo dose calculation algorithm with geant 4, Med Phys 43 (2) (2016) pp. 894–907, DOI: https://doi.org/10.1118/1.4939808.

[5] A. Ahnesj´o, Collapsed cone convolution of radiant energy for photon dose calculation in heterogeneous media, Medical Physics 16 (4) (1989) pp. 577–592, DOI: https://doi.org/10.1118/1.596360.

[6] E. E. Ahunbay, O. Ates, X. A. Li, An online replanning method using warm start optimization and aperture morphing for flattening-filter-free beams, Medical Physics 43 (8Part1) (2016) pp. 4575–4584, DOI: https://doi.org/10.1118/1.4955439.

[7] M. Alber, M. Birkner, W. Laub, F. Nüsslin, Hyperion — An integrated IMRT planning tool, in: The Use of Computers in Radiation Therapy, Springer Berlin Heidelberg pp. 46–48.

[8] M. Alber, F. Nüsslin, An objective function for radiation treatment optimization based on local biological measures, Phys Med Biol 44 (2) (1999) pp. 479–493, DOI: 10.1088/0031-9155/44/2/014.

[9] J. Allison, K. Amako, J. Apostolakis, H. Araujo, P. A. Dubois, M. Asai, et al., Geant4 developments and applications, IEEE Transactions on Nuclear Science 53 (1) (2006) pp. 270–278, DOI: 10.1109/TNS.2006.869826.

[10] H. Almansour, S. Afat, V. Fritz, F. Schick, M. Nachbar, D. Thorwarth, et al., Prospective Image Quality and Lesion Assessment in the Setting of MR-Guided Radiation Therapy of Prostate Cancer on an MR-Linac at 1.5 T: A Comparison to a Standard 3 T MRI, Cancers 13 (7) (2021) p. 1533.

[11] W.-H. AM, K. PS, W. D, A. EM, van Asselen B, B. GH, et al., Feasibility of stereotactic radiotherapy using a 1.5 T MR-linac: Multi-fraction treatment of pelvic lymph node oligometastases, Radiother Oncol 134 (2019) pp. 50–54.

[12] M. N. Anjum, W. Parker, R. Ruo, I. Aldahlawi, M. Afzal, IMRT Quality Assurance Using a Second Treatment Planning System, Med Dosim 35 (4) (2010) pp. 274–279, DOI: https://doi.org/10.1016/j.meddos.2009.09.001.

[13] B. Walters, I. Kawrakow, D. W. O. Rogers., DOSXYZnrc Users Manual. Technical Report PIRS-794revB, National Research Council Canada (2018).

[14] H. E. Bainbridge, M. J. Menten, M. F. Fast, S. Nill, U. Oelfke, F. McDonald, Treating locally advanced lung cancer with a 1.5T MR-Linac – Effects of the magnetic field and irradiation geometry on conventionally fractionated and isotoxic dose-escalated radiotherapy, Radiotherapy and Oncology 125 (2) (2017) pp. 280–285, DOI: https://doi.org/10.1016/j.radonc.2017.09.009.

[15] J. Baró, J. Sempau, J. M. Fernández-Varea, F. Salvat, PENELOPE: An algorithm for Monte Carlo simulation of the penetration and energy loss of electrons and positrons in matter, Nuclear Instruments and Methods in Physics Research Section B: Beam Interactions with Materials and Atoms 100 (1) (1995) pp. 31–46, DOI: https://doi.org/10.1016/0168-583X(95)00349-5.

[16] R. Baskar, K. A. Lee, R. Yeo, K.-W. Yeoh, Cancer and radiation therapy: current advances and future directions, International journal of medical sciences 9 (3) (2012) pp. 193–199, DOI: 10.7150/ijms.3635.

[17] P. S. Basran, M. K. Woo, An analysis of tolerance levels in IMRT quality assurance procedures, Med Phys 35 (6) (2008) pp. 2300–7, DOI: 10.1118/1.2919075.

[18] M. Baumann, C. Petersen, TCP and NTCP: a basic introduction, Rays 30 (2) (2005) pp. 99–104.

[19] J. E. Bayouth, D. A. Low, H. Zaidi, MRI-linac systems will replace conventional IGRT systems within 15 years, Medical Physics 46 (9) (2019) pp. 3753–3756, DOI: https://doi.org/10.1002/mp.13657.

[20] A. S. Bertelsen, T. Schytte, P. K. Moller, F. Mahmood, H. L. Riis, K. L. Gottlieb, et al., First clinical experiences with a high field 1.5 T MR linac, Acta Oncol (2019) pp. 1–6, DOI: 10.1080/0284186X.2019.1627417.

[21] A. K. Berthelsen, J. Dobbs, E. Kjellén, T. Landberg, T. R. Möller, P. Nilsson, et al., What's new in target volume definition for radiologists in ICRU Report 71? How can the ICRU volume definitions be integrated in clinical practice?, Cancer imaging : the official publication of the International Cancer Imaging Society 7 (1) (2007) pp. 104–116, DOI: 10.1102/1470-7330.2007.0013.

[22] J. C. Beukema, P. van Luijk, J. Widder, J. A. Langendijk, C. T. Muijs, Is cardiac toxicity a relevant issue in the radiation treatment of esophageal cancer?, Radiother Oncol 114 (1) (2015) pp. 85–90, DOI: 10.1016/j.radonc.2014.11.037.

[23] Y. V. Bogachev, A. V. Nikitina, V. V. Frolov, V. I. Chizhik, MRI-Guided Therapy, Technical Physics 65 (9) (2020) pp. 1427–1435, DOI: 10.1134/S1063784220090078.

[24] G. H. Bol, S. Hissoiny, J. J. W. Lagendijk, B. W. Raaymakers, Fast online Monte Carlo-based IMRT planning for the MRI linear accelerator, Phys Med Biol 57 (5) (Feb. 2012) pp. 1375–1385, DOI: 10.1088/0031-9155/57/5/1375.

[25] P. Bonomo, M. Lo Russo, M. Nachbar, S. Boeke, S. Gatidis, D. Zips, et al., 1.5 T MR-linac planning study to compare two different strategies of rectal boost irradiation, Clinical and Translational Radiation Oncology 26 (2021) pp. 86–91, DOI: https://doi.org/10.1016/j.ctro.2020.11.016.

[26] T. Bortfeld, IMRT: a review and preview, Physics in Medicine and Biology 51 (13) (2006) R363–R379, DOI: 10.1088/0031-9155/51/13/r21.

[27] D. H. Brand, J. R. Yarnold, The Linear–Quadratic Model and Implications for Fractionation, Clinical Oncology 31 (10) (2019) pp. 673–677, DOI: 10.1016/j.clon.2019.06.007.

[28] A. M. E. Bruynzeel, F. J. Lagerwaard, The role of biological dose-escalation for pancreatic cancer, Clinical and Translational Radiation Oncology 18 (2019) pp. 128–130, DOI: https://doi.org/10.1016/j.ctro.2019.04.020.

[29] F. Cardoso, S. Kyriakides, S. Ohno, F. Penault-Llorca, P. Poortmans, I. T. Rubio, et al., Early breast cancer: ESMO Clinical Practice Guidelines for di-

agnosis, treatment and follow-up, Annals of Oncology 30 (8) (2019) pp. 1194–1220, DOI: 10.1093/annonc/mdz173.

[30] D. S. Chang, F. D. Lasley, I. J. Das, M. S. Mendonca, J. R. Dynlacht, Radiation Survival Models, SLD, PLD, and Dose Rate, in: *Basic Radiotherapy Physics and Biology*, Cham: Springer International Publishing, 2021 pp. 243–253, DOI: 10.1007/978-3-030-61899-5_23.

[31] K. R. Charaghvandi, T. van't Westeinde, S. Yoo, A. C. Houweling, A. Rodrigues, H. M. Verkooijen, et al., Single dose partial breast irradiation using an MRI linear accelerator in the supine and prone treatment position, Clin Transl Radiat Oncol 14 (2019) pp. 1–7, DOI: https://doi.org/10.1016/j.ctro.2018.09.001.

[32] G. P. Chen, E. Ahunbay, X. A. Li, Technical Note: Development and performance of a software tool for quality assurance of online replanning with a conventional Linac or MR-Linac, Med Phys 43 (4) (2016) p. 1713, DOI: 10.1118/1.4943795.

[33] X. Chen, E. S. Paulson, E. Ahunbay, A. Sanli, S. Klawikowski, X. A. Li, Measurement validation of treatment planning for a MR-Linac, J Appl Clin Med Phys 20 (7) (2019) pp. 28–38, DOI: 10.1002/acm2.12651.

[34] X. Chen, P. Prior, G. P. Chen, C. J. Schultz, X. A. Li, Technical note: dose effects of 1.5 T transverse magnetic field on tissue interfaces in MRI-guided radiotherapy, Med Phys 43 (2016), DOI: 10.1118/1.4959534.

[35] I. J. Chetty, B. Curran, J. E. Cygler, J. J. DeMarco, G. Ezzell, B. A. Faddegon, et al., Report of the AAPM Task Group No. 105: Issues associated with clinical implementation of Monte Carlo-based photon and electron external beam treatment planning, Med Phys 34 (12) (2007) pp. 4818–4853, DOI: https://doi.org/10.1118/1.2795842.

[36] L. Chiloiro G.and Boldrini, E. Meldolesi, A. Re, F. Cellini, D. Cusumano, B. Corvari, et al., MR-guided radiotherapy in rectal cancer: first clinical experience of an innovative technology, Clin Transl Radiat Oncol 18 (2019) pp. 80–86, DOI: https://doi.org/10.1016/j.ctro.2019.04.006.

[37] R. W. Chuter, P. Whitehurst, A. Choudhury, M. van Herk, A. McWilliam, Technical Note: Investigating the impact of field size on patient selection for the 1.5T MR-Linac, Med Phys 44 (11) (2017) pp. 5667–5671, DOI: 10.1002/mp.12557.

[38] F. of Clinical Oncology TRCoR, Postoperative radiotherapy for breast cancer: UK consensus statements. Press Release, Nov. November 2016.

[39] C. E. Coles, C. L. Griffin, A. M. Kirby, J. Titley, R. K. Agrawal, A. Alhasso, et al., Partial-breast radiotherapy after breast conservation surgery for patients

with early breast cancer (UK IMPORT LOW trial): 5-year results from a multicentre, randomised, controlled, phase 3, non-inferiority trial, The Lancet 390 (10099) (2017) pp. 1048–1060, DOI: https://doi.org/10.1016/S0140-6736(17)31145-5.

[40] C. De-Colle, M. Nachbar, D. M'onnich, S. Boeke, C. Gani, N. Weidner, et al., Analysis of the electron-stream effect in patients treated with partial breast irradiation using the 1.5 T MR-linear accelerator, Clinical and Translational Radiation Oncology 27 (2021) pp. 103–108, DOI: https://doi.org/10.1016/j.ctro.2020.12.005.

[41] S. Corradini, F. Alongi, N. Andratschke, C. Belka, L. Boldrini, F. Cellini, et al., MR-guidance in clinical reality: current treatment challenges and future perspectives, Radiat Oncol 14 (1) (2019) p. 92, DOI: 10.1186/s13014-019-1308-y.

[42] S. Corradini, F. Alongi, N. Andratschke, C. Belka, L. Boldrini, F. Cellini, et al., MR-guidance in clinical reality: current treatment challenges and future perspectives, Radiat Oncol 14 (1) (2019) p. 92, DOI: 10.1186/s13014-019-1308-y.

[43] R. Damadian, Tumor Detection by Nuclear Magnetic Resonance, Science 171 (3976) (1971) pp. 1151–1153, DOI: 10.1126/science.171.3976.1151.

[44] I. J. Das, K. P. McGee, N. Tyagi, H. Wang, Role and future of MRI in radiation oncology, Br J Radiol 92 (1094) (2019) p. 20180505, DOI: 10.1259/bjr.20180505.

[45] G. X. Ding, Energy spectra, angular spread, fluence profiles and dose distributions of 6 and 18 MV photon beams: results of Monte Carlo simulations for a Varian 2100EX accelerator, Phys Med Biol 47 (7) (Mar. 2002) pp. 1025–1046, DOI: 10.1088/0031-9155/47/7/303.

[46] B. Dörschel, V. Schuricht, J. Steuer, Praktische Strahlenschutzphysik, in: Spektrum Akademischer Verlag, 1992, chap. Praktische Grundlagen des Strahlenschutzes p. 58.

[47] S. Ehrbar, A. Jöhl, A. Tartas, L. S. Stark, O. Riesterer, S. Klöck, et al., ITV, mid-ventilation, gating or couch tracking &2013; A comparison of respiratory motion-management techniques based on 4D dose calculations, Radiotherapy and Oncology 124 (1) (2017) pp. 80–88, DOI: 10.1016/j.radonc.2017.05.016.

[48] H. EY, W. Z, L. HJ, dela Cruz Paulino A, L. C, Measurement of electron return effect and skin dose reduction by a bolus in an anthropomorphic physical phantom under a magnetic resonance guided linear accelerator (MR-LINAC) system, Int'l J. of Medical Physics, Clinical Eng. and Radiation Oncology (7) (2018) pp. 339–346.

[49] M. Fast, A. van de Schoot, T. van de Lindt, C. Carbaat, U. van der Heide, J. J. Sonke, Tumor Trailing for Liver SBRT on the MR-Linac, Int J Radiat Oncol Biol Phys 103 (2) (2019) pp. 468–478, DOI: 10.1016/j.ijrobp.2018.09.011.

[50] T. Finazzi, J. R. van Sörnsen de Koste, M. A. Palacios, F. O. B. Spoelstra, B. J. Slotman, C. J. A. Haasbeek, et al., Delivery of magnetic resonance-guided single-fraction stereotactic lung radiotherapy, Phys Imag Radiat Oncol 14 (2020) pp. 17–23, DOI: 10.1016/j.phro.2020.05.002.

[51] C. Fiorino, M. Guckenberger, M. Schwarz, U. A. van der Heide, B. Heijmen, Technology-driven research for radiotherapy innovation, Molecular Oncology 14 (7) (2020) pp. 1500–1513, DOI: https://doi.org/10.1002/1878-0261.12659.

[52] M. Fippel, Fast Monte Carlo dose calculation for photon beams based on the VMC electron algorithm, Med Phys 26 (8) (1999) pp. 1466–1475, DOI: https://doi.org/10.1118/1.598676.

[53] M. Friedel, M. Nachbar, D. Mönnich, O. Dohm, D. Thorwarth, Development and validation of a 1.5 T MR-Linac full accelerator head and cryostat model for Monte Carlo dose simulations, Med Phys 46 (11) (2019) pp. 5304–5313, DOI: 10.1002/mp.13829.

[54] R. Fusco, M. Petrillo, V. Granata, S. Filice, M. Sansone, O. Catalano, et al., Magnetic Resonance Imaging Evaluation in Neoadjuvant Therapy of Locally Advanced Rectal Cancer: A Systematic Review, Radiol Oncol 51 (3) (2017) pp. 252–262, DOI: 10.1515/raon-2017-0032.

[55] R. Gahbauer, T. Landberg, J. Chavaudra, J. Dobbs, N. Gupta, G. Hanks, et al., ICRU Report 71, Journal of the International Commission on Radiation Units and Measurements 4 (1) (2016) NP–NP, DOI: 10.1093/jicru/4.1.Report71.

[56] C. Gani, S. Boeke, H. McNair, J. Ehlers, M. Nachbar, D. Ḿonnich, et al., Marker-less online MR-guided stereotactic body radiotherapy of liver metastases at a 1.5 T MR-Linac - Feasibility, workflow data and patient acceptance, Clin Transl Radiat Oncol 26 (2021) pp. 55–61, DOI: 10.1016/j.ctro.2020.11.014.

[57] C. Gani, L. Boldrini, V. Valentini, Online MR guided radiotherapy for rectal cancer. New opportunities, Clin Transl Radiat Oncol 18 (2019) pp. 66–67, DOI: 10.1016/j.ctro.2019.04.005.

[58] C. Gani, M. Lo Russo, S. Boeke, D. Wegener, S. Gatidis, S. Butzer, et al., A novel approach for radiotherapy dose escalation in rectal cancer using online MR-guidance and rectal ultrasound gel filling – Rationale and first in human, Radiotherapy and Oncology 164 (2021) pp. 37–42, DOI: https://doi.org/10.1016/j.radonc.2021.09.002.

[59] J. I. Geh, S. J. Bond, S. M. Bentzen, R. Glynne-Jones, Systematic overview of preoperative (neoadjuvant) chemoradiotherapy trials in oesophageal cancer: evidence of a radiation and chemotherapy dose response, Radiother Oncol 78 (3) (2006) pp. 236–44, DOI: 10.1016/j.radonc.2006.01.009.

[60] P. Giraud, E. Morvan, L. Claude, F. Mornex, C. Le Pechoux, J.-M. Bachaud, et al., Respiratory Gating Techniques for Optimization of Lung Cancer Radiotherapy, Journal of Thoracic Oncology 6 (12) (2011) pp. 2058–2068, DOI: https://doi.org/10.1097/JTO.0b013e3182307ec2.

[61] S. A. Graves, J. E. Snyder, A. Boczkowski, J. St-Aubin, D. Wang, S. Yaddanapudi, et al., Commissioning and performance evaluation of RadCalc for the Elekta unity MRI-linac, J Appl Clin Med Phys 20 (12) (2019) pp. 54–62, DOI: 10.1002/acm2.12760.

[62] E. Gregersen, The Britannica Guide to Particle Physics (Physics Explained), Britannica Educational Publishing, 2011 p. 116.

[63] M. L. Groot Koerkamp, J. E. Vasmel, N. S. Russell, S. F. Shaitelman, C. N. Anandadas, A. Currey, et al., Optimizing MR-Guided Radiotherapy for Breast Cancer Patients, Frontiers in Oncology 10 (1107) (2020), DOI: 10.3389/fonc.2020.01107.

[64] A. Gustafsson, B. K. Lind, A. Brahme, A generalized pencil beam algorithm for optimization of radiation therapy, Medical Physics 21 (3) (1994) pp. 343–356, DOI: https://doi.org/10.1118/1.597302.

[65] S. L. Hackett, B. van Asselen, J. W. H. Wolthaus, J. J. Bluemink, K. Ishakoglu, J. Kok, et al., Spiraling contaminant electrons increase doses to surfaces outside the photon beam of an MRI-linac with a perpendicular magnetic field, Phys Med Biol 63 (9) (2018) p. 095001, DOI: 10.1088/1361-6560/aaba8f.

[66] S. L. Hackett, B. Asselen, J. W. H. Wolthaus, Spiraling contaminant electrons increase doses to surfaces outside the photon beam of an MRI-linac with a perpendicular magnetic field, Phys Med Biol 63 (2018), DOI: 10.1088/1361-6560/aaba8f.

[67] K. Hanno, Strahlungsquellen für Technik und Medizin, in: Springer Spektrum, 2013, chap. Wechselwirkungen ionisierender Photonenstrahlung pp. 167–173.

[68] K. Hanno, Strahlungsquellen für Technik und Medizin, in: Springer Spektrum, 2013, chap. Medizinische Elektronenliniearbeschleunier pp. 195–243.

[69] T. C. Heijst, M. D. Hartogh, J. J. Lagendijk, H. J. Bongard, B. Asselen, MR-guided breast radiotherapy: feasibility and magnetic-field impact on skin dose, Phys Med Biol 58 (2013), DOI: 10.1088/0031-9155/58/17/5917.

[70] R. E. Hendrick, Breast MRI, in: *Fundamentals and Technical Aspects*, Springer-Verlag New York, 2008, chap. Fundamentals of Magnetic Resonance Imaging pp. 1–17, DOI: 10.1007/978-0-387-73507-8.

[71] L. E. Henke, J. A. Contreras, O. L. Green, B. Cai, H. Kim, M. C. Roach, et al., Magnetic Resonance Image-Guided Radiotherapy (MRIgRT): A 4.5-Year Clinical Experience, Clinical Oncology 30 (11) (2018) pp. 720–727, DOI: https://doi.org/10.1016/j.clon.2018.08.010.

[72] M. van Herk, Errors and margins in radiotherapy, Seminars in Radiation Oncology 14 (1) (2004) pp. 52–64, DOI: https://doi.org/10.1053/j.semradonc.2003.10.003.

[73] M. van Herk, P. Remeijer, C. Rasch, J. V. Lebesque, The probability of correct target dosage: dose-population histograms for deriving treatment margins in radiotherapy, International Journal of Radiation Oncology, Biology, Physics 47 (4) (2000) pp. 1121–1135, DOI: 10.1016/S0360-3016(00)00518-6.

[74] S. Hissoiny, A. J. E. Raaijmakers, B. Ozell, P. Després, B. W. Raaymakers, Fast dose calculation in magnetic fields withGPUMCD, Phys Med Biol 56 (16) (July 2011) pp. 5119–5129, DOI: 10.1088/0031-9155/56/16/003.

[75] S. Hissoiny, B. Ozell, H. Bouchard, P. Després, GPUMCD: A new GPU-oriented Monte Carlo dose calculation platform, Med Phys 38 (2) (2011) pp. 754–764, DOI: https://doi.org/10.1118/1.3539725.

[76] P. J. van Houdt, H. Saeed, D. Thorwarth, C. D. Fuller, W. A. Hall, B. A. McDonald, et al., Integration of quantitative imaging biomarkers in clinical trials for MR-guided radiotherapy: Conceptual guidance for multicentre studies from the MR-Linac Consortium Imaging Biomarker Working Group, European Journal of Cancer 153 (2021) pp. 64–71, DOI: https://doi.org/10.1016/j.ejca.2021.04.041.

[77] A. C. Houweling, J. H. de Vries, J. Wolthaus, S. Woodings, J. G. Kok, B. van Asselen, et al., Performance of a cylindrical diode array for use in a 1.5 T MR-linac, Phys Med Biol 61 (3) (2016) N80–9, DOI: 10.1088/0031-9155/61/3/n80.

[78] I. Kawrakow, E. Mainegra-Hing, D. W. O. Rogers, F. Tessier, B. R. B. Walters., BEAMnrc Users Manual, Technical Report PIRS-0509(A)revL, National Research Council Canada (2018).

[79] I. Kawrakowa, E. Mainegra-Hing, D. W. and O. Rogers, F. Tessier, B. R. B. Walters., The EGSnrc Code System: Monte Carlo simulation of electron and photon transport. Technical Report PIRS-701, National Research Council Canada (2018).

[80] Interdisziplinäre S3-Leitlinie für die Früherkennung Diagnostik Therapie und Nachsorge des Mammakarzinoms. Generic, Dec. 2017.

[81] M. P. W. Intven, S. R. de Mol van Otterloo, S. Mook, P. A. H. Doornaert, E. N. de Groot-van Breugel, G. G. Sikkes, et al., Online adaptive MR-guided radiotherapy for rectal cancer; feasibility of the workflow on a 1.5T MR-linac: clinical implementation and initial experience, Radiotherapy and Oncology 154 (2021) pp. 172–178, DOI: https://doi.org/10.1016/j.radonc.2020.09.024.

[82] B. A. Jereczek-Fossa, L. Santoro, D. Zerini, C. Fodor, B. Vischioni, M. Dispinzieri, et al., Image Guided Hypofractionated Radiotherapy and Quality of Life for Localized Prostate Cancer: Prospective Longitudinal Study in 337 Patients, The Journal of Urology 189 (6) (2013) pp. 2099–2103, DOI: https://doi.org/10.1016/j.juro.2013.01.005.

[83] D. Jones, ICRU Report 50—Prescribing, Recording and Reporting Photon Beam Therapy, Medical Physics 21 (6) (1994) pp. 833–834, DOI: https://doi.org/10.1118/1.597396.

[84] M. Jones, G. Hruby, P. Stanwell, S. Gallagher, K. Wong, J. Arm, et al., Multiparametric MRI as an outcome predictor for anal canal cancer managed with chemoradiotherapy, BMC Cancer 15 (2015) p. 281, DOI: 10.1186/s12885-015-1244-7.

[85] T. Ju, T. Simpson, J. O. Deasy, D. A. Low, Geometric interpretation of the dose distribution comparison technique: Interpolation-free calculation, Medical Physics 35 (3) (2008) pp. 879–887, DOI: https://doi.org/10.1118/1.2836952.

[86] J. H. A. M. Kaanders, J. Bussink, A. J. van der Kogel, ARCON: a novel biology-based approach in radiotherapy, The Lancet Oncology 3 (12) (2002) pp. 728–737, DOI: https://doi.org/10.1016/S1470-2045(02)00929-4.

[87] J. G. Kaas, W. v. d. Wollenberg, A. v. d. Schoot, F. Wittkämper, T. M. Janssen, PO-0994: A fast automated sanity check for online plan adaptation in MR-guided RT, Radiotherapy and Oncology 127 (2018).

[88] M. Kawashima, S. Ozawa, A. Haga, A. Sakumi, C. Kurokawa, S. Sugimoto, et al., Comparison of total MU and segment areas in VMAT and step-and-shoot IMRT plans, Radiol Phys Technol 6 (1) (2013) pp. 14–20, DOI: 10.1007/s12194-012-0164-3.

[89] I. Kawrakow, M. Fippel, Investigation of variance reduction techniques for Monte Carlo photon dose calculation using XVMC, Phys Med Biol 45 (8) (2000) pp. 2163–83, DOI: 10.1088/0031-9155/45/8/308.

[90] I. Kawrakow, D. W. O. Rogers, B. R. B. Walters, Large efficiency improvements in BEAMnrc using directional bremsstrahlung splitting, Med Phys 31 (10) (2004) pp. 2883–2898, DOI: https://doi.org/10.1118/1.1788912.

[91] I. Kawrakow, B. R. B. Walters, Efficient photon beam dose calculations using DOSXYZnrc with BEAMnrc, Med Phys 33 (8) (2006) pp. 3046–3056, DOI: https://doi.org/10.1118/1.2219778.

[92] A. Kim, S. Lim-Reinders, C. McCann, S. B. Ahmad, A. Sahgal, J. Lee, et al., Magnetic field dose effects on different radiation beam geometries for hypofractionated partial breast irradiation, J Appl Clin Med Phys 18 (6) (2017) pp. 62–70, DOI: 10.1002/acm2.12182.

[93] S. Kluter, Technical design and concept of a 0.35 T MR-Linac, Clin Transl Radiat Oncol 18 (2019) pp. 98–101, DOI: 10.1016/j.ctro.2019.04.007.

[94] S. Klüter, O. Schrenk, C. K. Renkamp, S. Gliessmann, M. Kress, J. Debus, et al., A practical implementation of risk management for the clinical introduction of online adaptive Magnetic Resonance-guided radiotherapy, Phys Imag Radiat Oncol 17 (2021) pp. 53–57, DOI: 10.1016/j.phro.2020.12.005.

[95] C. Kontaxis, G. H. Bol, J. J. Lagendijk, B. W. Raaymakers, Towards adaptive IMRT sequencing for the MR-linac, Phys Med Biol 60 (6) (2015) pp. 2493–509, DOI: 10.1088/0031-9155/60/6/2493.

[96] C. Kontaxis, G. H. Bol, J. J. W. Lagendijk, B. W. Raaymakers, DeepDose: Towards a fast dose calculation engine for radiation therapy using deep learning, Phys Med Biol 65 (7) (2020) p. 075013, DOI: 10.1088/1361-6560/ab7630.

[97] T. Krieger, O. A. Sauer, Monte Carlo- versus pencil-beam-/collapsed-cone-dose calculation in a heterogeneous multi-layer phantom, Physics in Medicine and Biology 50 (5) (2005) pp. 859–868, DOI: 10.1088/0031-9155/50/5/010.

[98] M. F. Kruis, J. B. van de Kamer, J. S. A. Belderbos, J.-J. Sonke, M. van Herk, 4D CT amplitude binning for the generation of a time-averaged 3D mid-position CT scan, Physics in Medicine and Biology 59 (18) (2014) pp. 5517–5529, DOI: 10.1088/0031-9155/59/18/5517.

[99] J. J. W. Lagendijk, B. W. Raaymakers, C. A. T. V. den Berg, M. A. Moerland, M. E. Philippens, M. van Vulpen, MR guidance in radiotherapy, Phys Med Biol 59 (21) (Oct. 2014) R349–R369, DOI: 10.1088/0031-9155/59/21/r349.

[100] J. J. Lagendijk, B. W. Raaymakers, A. J. Raaijmakers, J. Overweg, K. J. Brown, E. M. Kerkhof, et al., MRI/linac integration, Radiother Oncol 86 (1) (2008) pp. 25–29, DOI: https://doi.org/10.1016/j.radonc.2007.10.034.

[101] J. J. Lagendijk, B. W. Raaymakers, M. van Vulpen, The Magnetic Resonance Imaging–Linac System, Seminars in Radiation Oncology 24 (3) (2014), Magnetic Resonance Imaging in Radiation Oncology pp. 207–209, DOI: https://doi.org/10.1016/j.semradonc.2014.02.009.

[102] T. Landberg, J. Chavaudra, J. Dobbs, J. .-. Gerard, G. Hanks, J. .-. Horiot, et al., ICRU Report 62–Prescribing, Recording and Reporting Photon Beam Therapy (Supplement to ICRU Report 50), Journal of the International Commission on Radiation Units and Measurements os32 (1) (2016) NP–NP, DOI: 10.1093/jicru/os32.1.Report62.

[103] P. C. Lauterbur, Image Formation by Induced Local Interactions: Examples Employing Nuclear Magnetic Resonance, Nature 242 (5394) (1973) pp. 190–191, DOI: 10.1038/242190a0.

[104] S. L. Lee, M. Bassetti, G. J. Meijer, S. Mook, Review of MR-Guided Radiotherapy for Esophageal Cancer, Frontiers in Oncology 11 (468) (2021), DOI: 10.3389/fonc.2021.628009.

[105] C. M. van Leeuwen, A. L. Oei, J. Crezee, A. Bel, N. A. P. Franken, L. J. A. Stalpers, et al., The alfa and beta of tumours: a review of parameters of the linear-quadratic model, derived from clinical radiotherapy studies, Radiation oncology (London, England) 13 (1) (2018) pp. 96–96, DOI: 10.1186/s13014-018-1040-z.

[106] D. Létourneau, M. Gulam, D. Yan, M. Oldham, J. W. Wong, Evaluation of a 2D diode array for IMRT quality assurance, Radiother Oncol 70 (2) (2004) pp. 199–206, DOI: 10.1016/j.radonc.2003.10.014.

[107] Y. Li, B. Wang, S. Ding, H. Liu, B. Liu, Y. Xia, et al., Feasibility of using a commercial collapsed cone dose engine for 1.5T MR-LINAC online independent dose verification, Phys Med 80 (2020) pp. 288–296, DOI: 10.1016/j.ejmp.2020.11.014.

[108] T. N. van de Lindt, M. F. Fast, S. R. van Kranen, M. E. Nowee, E. P. M. Jansen, U. A. van der Heide, et al., MRI-guided mid-position liver radiotherapy: Validation of image processing and registration steps, Radiotherapy and Oncology 138 (2019) pp. 132–140, DOI: https://doi.org/10.1016/j.radonc.2019.06.007.

[109] H. Liu, S. Ding, B. Wang, Y. Li, Y. Sun, X. Huang, In-Air Electron Streaming Effect for Esophageal Cancer Radiotherapy With a 1.5 T Perpendicular Magnetic Field: A Treatment Planning Study, Frontiers in oncology 10 (2020) pp. 607061–607061, DOI: 10.3389/fonc.2020.607061.

[110] D. A. Low, W. B. Harms, S. Mutic, J. A. Purdy, A technique for the quantitative evaluation of dose distributions, Med Phys 25 (5) (1998) pp. 656–61, DOI: 10.1118/1.598248.

[111] G. M, Renal cell cancer: a new indication, Clin Transl Radiat Oncol in press (2019).

[112] D. S. Makrani, H. Hasanzadeh, T. A. Pourfallah, A. Ghasemi, M. Jadidi, H. Babapour., Determination of primary electron beam parameters in a Siemens Primus Linac using Monte Carlo simulation. Journal of Paramedical Sciences (2015).

[113] V. N. Malkov, S. L. Hackett, B. van Asselen, B. W. Raaymakers, J. W. H. Wolthaus, Monte Carlo simulations of out-of-field skin dose due to spiralling contaminant electrons in a perpendicular magnetic field, Med Phys 46 (3) (2019) pp. 1467–1477, DOI: 10.1002/mp.13392.

[114] V. N. Malkov, S. L. Hackett, J. W. H. Wolthaus, B. W. Raaymakers, B. van Asselen, Monte Carlo simulations of out-of-field surface doses due to the electron streaming effect in orthogonal magnetic fields, Phys Med Biol 64 (11) (2019) p. 115029, DOI: 10.1088/1361-6560/ab0aa0.

[115] P. Mansfield, Multi-planar image formation using NMR spin echoes, Journal of Physics C: Solid State Physics 10 (3) (1977) pp. L55–L58, DOI: 10.1088/0022-3719/10/3/004.

[116] S. Marzi, B. Saracino, M. G. Petrongari, S. Arcangeli, S. Gomellini, G. Arcangeli, et al., Modeling of alpha/beta for late rectal toxicity from a randomized phase II study: conventional versus hypofractionated scheme for localized prostate cancer, Journal of experimental & clinical cancer research : CR 28 (1) (2009) pp. 117–117, DOI: 10.1186/1756-9966-28-117.

[117] E. Mayyas, I. J. Chetty, M. Chetvertkov, N. Wen, T. Neicu, T. Nurushev, et al., Evaluation of multiple image-based modalities for image-guided radiation therapy (IGRT) of prostate carcinoma: A prospective study, Medical Physics 40 (4) (2013) p. 041707, DOI: https://doi.org/10.1118/1.4794502.

[118] B. A. McDonald, S. Vedam, J. Yang, J. Wang, P. Castillo, B. Lee, et al., Initial Feasibility and Clinical Implementation of Daily MR-Guided Adaptive Head and Neck Cancer Radiation Therapy on a 1.5T MR-Linac System: Prospective R-IDEAL 2a/2b Systematic Clinical Evaluation of Technical Innovation, International Journal of Radiation Oncology*Biology*Physics 109 (5) (2021) pp. 1606–1618, DOI: https://doi.org/10.1016/j.ijrobp.2020.12.015.

[119] C. Ménard, U. van der Heide, Introduction: Systems for Magnetic Resonance Image Guided Radiation Therapy, Seminars in Radiation Oncology 24 (3) (2014), Magnetic Resonance Imaging in Radiation Oncology p. 192, DOI: https://doi.org/10.1016/j.semradonc.2014.02.010.

[120] M. J. Menten, M. F. Fast, S. Nill, C. P. Kamerling, F. McDonald, U. Oelfke, Lung stereotactic body radiotherapy with an MR-linac – quantifying the

impact of the magnetic field and real-time tumor tracking, Radiother Oncol 119 (2016), DOI: 10.1016/j.radonc.2016.04.019.

[121] M. J. Menten, J. K. Mohajer, R. Nilawar, J. Bertholet, A. Dunlop, A. U. Pathmanathan, et al., Automatic reconstruction of the delivered dose of the day using MR-linac treatment log files and online MR imaging, Radiother Oncol 145 (2020) pp. 88–94, DOI: https://doi.org/10.1016/j.radonc.2019.12.010.

[122] M. Miften, A. Olch, D. Mihailidis, J. Moran, T. Pawlicki, A. Molineu, et al., Tolerance limits and methodologies for IMRT measurement-based verification QA: Recommendations of AAPM Task Group No. 218, Med Phys 45 (4) (2018) e53–e83, DOI: 10.1002/mp.12810.

[123] B. D. Minsky, T. F. Pajak, R. J. Ginsberg, T. M. Pisansky, J. Martenson, R. Komaki, et al., INT 0123 (Radiation Therapy Oncology Group 94-05) phase III trial of combined-modality therapy for esophageal cancer: high-dose versus standard-dose radiation therapy, J Clin Oncol 20 (5) (2002) pp. 1167–74, DOI: 10.1200/JCO.2002.20.5.1167.

[124] R. Miralbell, S. A. Roberts, E. Zubizarreta, J. H. Hendry, Dose-Fractionation Sensitivity of Prostate Cancer Deduced From Radiotherapy Outcomes of 5,969 Patients in Seven International Institutional Datasets: Alpha/Beta = 1.4 (0.9–2.2) Gy, International Journal of Radiation Oncology Biology Physics 82 (1) (2012) e17–e24, DOI: https://doi.org/10.1016/j.ijrobp.2010.10.075.

[125] E. J. Moding, M. B. Kastan, D. G. Kirsch, Strategies for optimizing the response of cancer and normal tissues to radiation, Nature reviews. Drug discovery 12 (7) (2013) pp. 526–542, DOI: 10.1038/nrd4003.

[126] D. Mönnich, J. Winter, M. Nachbar, L. Künzel, S. Boeke, C. Gani, et al., Quality assurance of IMRT treatment plans for a 1.5 T MR-linac using a 2D ionization chamber array and a static solid phantom, Phys Med Biol 65 (16) (2020) 16nt01, DOI: 10.1088/1361-6560/aba5ec.

[127] P. Montay-Gruel, L. Meziani, C. Yakkala, M.-C. Vozenin, Expanding the therapeutic index of radiation therapy by normal tissue protection, The British journal of radiology 92 (1093) (2019) pp. 20180008–20180008, DOI: 10.1259/bjr.20180008.

[128] D. M. de Muinck Keizer, A. U. Pathmanathan, A. Andreychenko, L. G. W. Kerkmeijer, J. R. N. van der Voort van Zyp, A. C. Tree, et al., Fiducial marker based intra-fraction motion assessment on cine-MR for MR-linac treatment of prostate cancer, Phys Med Biol 64 (7) (2019) 07nt02, DOI: 10.1088/1361-6560/ab09a6.

[129] S. Munch, M. Oechsner, S. E. Combs, D. Habermehl, DVH- and NTCP-based dosimetric comparison of different longitudinal margins for VMAT-IMRT of esophageal cancer, Radiat Oncol 12 (1) (2017) p. 128, DOI: 10.1186/s13014-017-0871-3.

[130] T. A. Murray J, Prostate cancer – Advantages and disadvantages of MR-guided RT, Clin Transl Radiat Oncol in press (2019).

[131] M. Nachbar, D. Mönnich, S. Boeke, C. Gani, N. Weidner, V. Heinrich, et al., Partial breast irradiation with the 1.5 T MR-Linac: First patient treatment and analysis of electron return and stream effects, Radiother Oncol 145 (2019) pp. 30–35, DOI: 10.1016/j.radonc.2019.11.025.

[132] M. Nachbar, D. Mönnich, O. Dohm, M. Friedlein, D. Zips, D. Thorwarth, Automatic 3D Monte-Carlo-based secondary dose calculation for online verification of 1.5 T magnetic resonance imaging guided radiotherapy, Phys Imaging Radiat Oncol 19 (2021) pp. 6–12, DOI: 10.1016/j.phro.2021.05.002.

[133] M. Nachbar, D. Mönnich, P. Kalwa, D. Zips, D. Thorwarth, C. Gani, Comparison of treatment plans for a high-field MRI-linac and a conventional linac for esophageal cancer, Strahlentherapie und Onkologie 195 (4) (2019) pp. 327–334, DOI: 10.1007/s00066-018-1386-z.

[134] N. P. Nguyen, R. Davis, S. R. Bose, S. Dutta, V. Vinh-Hung, A. Chi, et al., Potential Applications of Image-Guided Radiotherapy for Radiation Dose Escalation in Patients with Early Stage High-Risk Prostate Cancer, Frontiers in Oncology 5 (2015) p. 18.

[135] F. A. van Nimwegen, M. Schaapveld, D. J. Cutter, C. P. Janus, A. D. Krol, M. Hauptmann, et al., Radiation Dose-Response Relationship for Risk of Coronary Heart Disease in Survivors of Hodgkin Lymphoma, J Clin Oncol 34 (3) (2016) pp. 235–43, DOI: 10.1200/JCO.2015.63.4444.

[136] D. J. O'Brien, D. A. Roberts, G. S. Ibbott, G. O. Sawakuchi, Reference dosimetry in magnetic fields: formalism and ionization chamber correction factors, Med Phys 43 (8Part1) (2016) pp. 4915–4927, DOI: https://doi.org/10.1118/1.4959785.

[137] J. M. Park, K. H. Shin, J. I. Kim, S. Y. Park, S. H. Jeon, N. Choi, et al., Air-electron stream interactions during magnetic resonance IGRT : Skin irradiation outside the treatment field during accelerated partial breast irradiation, Strahlenther Onkol 194 (1) (2018) pp. 50–59, DOI: 10.1007/s00066-017-1212-z.

[138] A. U. Pathmanathan, N. J. van As, L. G. Kerkmeijer, J. Christodouleas, C. A. Lawton, D. Vesprini, et al., Magnetic Resonance Imaging-Guided Adaptive Radiation Therapy: A "Game Changer" for Prostate Treatment?, In-

ternational Journal of Radiation Oncology*Biology*Physics 100 (2) (2018) pp. 361–373, DOI: https://doi.org/10.1016/j.ijrobp.2017.10.020.

[139] K. A. Pearlstein, R. C. Chen, Comparing Dosimetric, Morbidity, Quality of Life, and Cancer Control Outcomes After 3D Conformal, Intensity-Modulated, and Proton Radiation Therapy for Prostate Cancer, Seminars in Radiation Oncology 23 (3) (2013) pp. 182–190, DOI: https://doi.org/10.1016/j.semradonc.2013.01.004.

[140] S. Pojtinger, O. S. Dohm, R. P. Kapsch, D. Thorwarth, Ionization chamber correction factors for MR-linacs, Phys Med Biol 63 (11) (2018) 11nt03, DOI: 10.1088/1361-6560/aac4f2.

[141] S. Pojtinger, O. S. Dohm, R.-P. Kapsch, D. Thorwarth, Ionization chamber correction factors for MR-linacs, Physics in Medicine & Biology 63 (11) (June 2018) 11NT03, DOI: 10.1088/1361-6560/aac4f2.

[142] S. Pojtinger, M. Nachbar, R.-P. Kapsch, D. Thorwarth, Influence of beam quality on reference dosimetry correction factors in magnetic resonance guided radiation therapy, Physics and Imaging in Radiation Oncology 16 (2020) pp. 95–98, DOI: https://doi.org/10.1016/j.phro.2020.10.005.

[143] C. Polgar, T. Major, J. Fodor, Z. Sulyok, A. Somogyi, K. Lovey, et al., Accelerated partial-breast irradiation using high-dose-rate interstitial brachytherapy: 12-year update of a prospective clinical study, Radiother Oncol 94 (3) (2010) pp. 274–9, DOI: 10.1016/j.radonc.2010.01.019.

[144] C. Polgar, O. J. Ott, G. Hildebrandt, D. Kauer-Dorner, H. Knauerhase, T. Major, et al., Late side-effects and cosmetic results of accelerated partial breast irradiation with interstitial brachytherapy versus whole-breast irradiation after breast-conserving surgery for low-risk invasive and in-situ carcinoma of the female breast: 5-year results of a randomised, controlled, phase 3 trial, Lancet Oncol 18 (2) (2017) pp. 259–268, DOI: 10.1016/S1470-2045(17)30011-6.

[145] J. M. Pollard, Z. Wen, R. Sadagopan, J. Wang, G. S. Ibbott, The future of image-guided radiotherapy will be MR guided, The British journal of radiology 90 (1073) (2017) pp. 20160667–20160667, DOI: 10.1259/bjr.20160667.

[146] A. J. E. Raaijmakers, B. Hårdemark, B. W. Raaymakers, C. P. J. Raaijmakers, J. J. W. Lagendijk, Dose optimization for the MRI-accelerator: IMRT in the presence of a magnetic field, Phys Med Biol 52 (23) (Nov. 2007) pp. 7045–7054, DOI: 10.1088/0031-9155/52/23/018.

[147] A. J. E. Raaijmakers, B. W. Raaymakers, J. J. W. Lagendijk, Magnetic-field-induced dose effects in MR-guided radiotherapy systems: dependence on the magnetic field strength, Phys Med Biol 53 (4) (Jan. 2008) pp. 909–923, DOI: 10.1088/0031-9155/53/4/006.

[148] A. J. Raaijmakers, B. W. Raaymakers, J. J. Lagendijk, Integrating a MRI scanner with a 6 MV radiotherapy accelerator: dose increase at tissue-air interfaces in a lateral magnetic field due to returning electrons, Phys Med Biol 50 (7) (2005) pp. 1363–76, DOI: 10.1088/0031-9155/50/7/002.

[149] A. J. E. Raaijmakers, B. W. Raaymakers, S. v. d. Meer, J. J. W. Lagendijk, Integrating a MRI scanner with a 6 MV radiotherapy accelerator: impact of the surface orientation on the entrance and exit dose due to the transverse magnetic field, Physics in Medicine and Biology 52 (4) (2007) pp. 929–939, DOI: 10.1088/0031-9155/52/4/005.

[150] B. W. Raaymakers, I. M. Jürgenliemk-Schulz, G. H. Bol, M. Glitzner, A. N. T. J. Kotte, B. van Asselen, et al., First patients treated with a 1.5 T MRI-Linac: clinical proof of concept of a high-precision, high-field MRI guided radiotherapy treatment, Physics in Medicine & Biology 62 (23) (Nov. 2017) pp. L41–L50, DOI: 10.1088/1361-6560/aa9517.

[151] B. W. Raaymakers, A. J. E. Raaijmakers, A. N. T. J. Kotte, D. Jette, J. J. W. Lagendijk, Integrating a MRI scanner with a 6 MV radiotherapy accelerator: dose deposition in a transverse magnetic field, Phys Med Biol 49 (17) (Aug. 2004) pp. 4109–4118, DOI: 10.1088/0031-9155/49/17/019.

[152] B. W. Raaymakers, J. J. Lagendijk, J. Overweg, J. G. Kok, A. J. Raaijmakers, E. M. Kerkhof, et al., Integrating a 1.5 T MRI scanner with a 6 MV accelerator: proof of concept, Phys Med Biol 54 (12) (2009) N229–37, DOI: 10.1088/0031-9155/54/12/n01.

[153] M. L. Reyhan, T. Chen, M. Zhang, Characterization of the effect of MRI on Gafchromic film dosimetry, Journal of applied clinical medical physics 16 (6) (2015) 325–332-325–332, DOI: 10.1120/jacmp.v16i6.5743.

[154] F. J. Reynoso, A. Curcuru, O. Green, S. Mutic, I. J. Das, L. Santanam, Technical Note: Magnetic field effects on Gafchromic-film response in MR-IGRT, Med Phys 43 (12) (2016) p. 6552, DOI: 10.1118/1.4967486.

[155] S. Richter, S. Pojtinger, D. Mönnich, O. Dohm, D. Thorwarth, Influence of a transverse magnetic field on the dose deposited by a 6 MV linear accelerator, Current Directions in Biomedical Engineering 3 (2) (2017) pp. 281–285.

[156] S. Richter, D. Mönnich, S. Pojtinger, O. Dohm, D. Zips, D. Thorwarth, PO-0887: Influence of a magnetic field on the dose deposited by a 6 MV linac at tissue interfaces. Aug. 2018.

[157] W. C. Röntgen, On a new kind of rays, Science 3 (59) (1896) pp. 227–231.

[158] P. S. N. van Rossum, A. L. H. M. W. van Lier, M. van Vulpen, O. Reerink, J. J. W. Lagendijk, S. H. Lin, et al., Diffusion-weighted magnetic resonance imaging for the prediction of pathologic response to neoadjuvant chemoradio-

therapy in esophageal cancer, Radiother Oncol 115 (2) (2015) pp. 163–170, DOI: 10.1016/j.radonc.2015.04.027.

[159] O. Schrenk, C. K. Spindeldreier, L. N. Burigo, J. Hoerner-Rieber, A. Pfaffenberger, Effects of magnetic field orientation and strength on the treatment planning of nonsmall cell lung cancer, Med Phys 44 (2017), DOI: 10.1002/mp.12631.

[160] N. W. Schurink, D. M. J. Lambregts, R. G. H. Beets-Tan, Diffusion-weighted imaging in rectal cancer: current applications and future perspectives, The British journal of radiology 92 (1096) (2019) pp. 20180655–20180655, DOI: 10.1259/bjr.20180655.

[161] R. A. Sharma, R. Plummer, J. K. Stock, T. A. Greenhalgh, O. Ataman, S. Kelly, et al., Clinical development of new drug–radiotherapy combinations, Nature Reviews Clinical Oncology 13 (10) (2016) pp. 627–642, DOI: 10.1038/nrclinonc.2016.79.

[162] D. Sheikh-Bagheri, D. W. O. Rogers, Sensitivity of megavoltage photon beam Monte Carlo simulations to electron beam and other parameters, Med Phys 29 (3) (2002) pp. 379–390, DOI: https://doi.org/10.1118/1.1446109.

[163] D. Sheikh-Bagheri, D. W. O. Rogers, C. K. Ross, J. P. Seuntjens, Comparison of measured and Monte Carlo calculated dose distributions from the NRC linac, Med Phys 27 (10) (2000) pp. 2256–2266, DOI: https://doi.org/10.1118/1.1290714.

[164] R. L. Siegel, K. D. Miller, A. Jemal, Cancer statistics, 2019, CA Cancer J Clin 69 (1) (2019) pp. 7–34, DOI: 10.3322/caac.21551.

[165] C. K. Spindeldreier, O. Schrenk, A. Bakenecker, I. Kawrakow, L. Burigo, C. P. Karger, et al., Radiation dosimetry in magnetic fields with Farmer-type ionization chambers: determination of magnetic field correction factors for different magnetic field strengths and field orientations, Physics in Medicine & Biology 62 (16) (2017) pp. 6708–6728, DOI: 10.1088/1361-6560/aa7ae4.

[166] C. W. Stanhope, D. G. Drake, J. Liang, M. Alber, M. S´ohn, C. Habib, et al., Evaluation of machine log files/MC-based treatment planning and delivery QA as compared to ArcCHECK QA, Med Phys 45 (7) (2018) pp. 2864–2874, DOI: 10.1002/mp.12926.

[167] M. Stasi, S. Bresciani, A. Miranti, A. Maggio, V. Sapino, P. Gabriele, Pretreatment patient-specific IMRT quality assurance: a correlation study between gamma index and patient clinical dose volume histogram, Med Phys 39 (12) (2012) pp. 7626–34, DOI: 10.1118/1.4767763.

[168] T. S. Stelljes, A. Harmeyer, J. Reuter, H. K. Looe, N. Chofor, D. Harder, et al., Dosimetric characteristics of the novel 2D ionization chamber array

OCTAVIUS Detector 1500, Med Phys 42 (4) (2015) pp. 1528–37, DOI: 10.1118/1.4914151.

[169] V. Strnad, O. J. Ott, G. Hildebrandt, D. Kauer-Dorner, H. Knauerhase, T. Major, et al., 5-year results of accelerated partial breast irradiation using sole interstitial multicatheter brachytherapy versus whole-breast irradiation with boost after breast-conserving surgery for low-risk invasive and in-situ carcinoma of the female breast: a randomised, phase 3, non-inferiority trial, Lancet 387 (10015) (2016) pp. 229–38, DOI: 10.1016/S0140-6736(15)00471-7.

[170] J. C. Stroom, H. C. J. de Boer, H. Huizenga, A. G. Visser, Inclusion of geometrical uncertainties in radiotherapy treatment planning by means of coverage probability, International Journal of Radiation Oncology*Biology*Physics 43 (4) (1999) pp. 905–919, DOI: https://doi.org/10.1016/S0360-3016(98)00468-4.

[171] T. Sumanaweera, G. Glover, S. Song, J. Adler, S. Napel, Quantifying MRI geometric distortion in tissue, Magnetic Resonance in Medicine 31 (1) (1994) pp. 40–47, DOI: https://doi.org/10.1002/mrm.1910310106.

[172] D. Thorwarth, Functional imaging for radiotherapy treatment planning: current status and future directions-a review, Br J Radiol 88 (1051) (2015) p. 20150056, DOI: 10.1259/bjr.20150056.

[173] D. Thorwarth, M. Notohamiprodjo, D. Zips, A. C. Muller, Personalized precision radiotherapy by integration of multi-parametric functional and biological imaging in prostate cancer: A feasibility study, Z Med Phys 27 (1) (2017) pp. 21–30, DOI: 10.1016/j.zemedi.2016.02.002.

[174] D. Thorwarth, M. Alber, [Individualised radiotherapy on the basis of functional imaging with FMISO PET], Zeitschrift fur medizinische Physik 18 (1) (2008) pp. 43–50, DOI: 10.1016/j.zemedi.2007.08.003.

[175] D. Thorwarth, M. Ege, M. Nachbar, D. Mönnich, C. Gani, D. Zips, et al., Quantitative magnetic resonance imaging on hybrid magnetic resonance linear accelerators: Perspective on technical and clinical validation, Phys Imag Radiat Oncol 16 (2020) pp. 69–73, DOI: 10.1016/j.phro.2020.09.007.

[176] R. H. N. Tijssen, M. E. P. Philippens, E. S. Paulson, M. Glitzner, B. Chugh, A. Wetscherek, et al., MRI commissioning of 1.5T MR-linac systems a multi-institutional study, Radiotherapy and Oncology 132 (2019) pp. 114–120, DOI: 10.1016/j.radonc.2018.12.011.

[177] J. E. van Timmeren, M. Chamberlain, J. Krayenbuehl, L. Wilke, S. Ehrbar, M. Bogowicz, et al., Comparison of beam segment versus full plan re-optimization in daily magnetic resonance imaging-guided online-adaptive radiotherapy,

Phys Imag Radiat Oncol 17 (2021) pp. 43–46, DOI: 10.1016/j.phro.2021.01.001.

[178] K. D. Toennies, Guide to Medical Image Analysis, in: *Methods and Algorithms*, Springer-Verlag London, 2012, chap. Digital Image Acquisition pp. 21–60.

[179] I. Torres-Xirau, I. Olaciregui-Ruiz, R. A. Rozendaal, P. González, B. J. Mijnheer, J. J. Sonke, et al., A back-projection algorithm in the presence of an extra attenuating medium: towards EPID dosimetry for the MR-Linac, Phys Med Biol 62 (15) (2017) pp. 6322–6340, DOI: 10.1088/1361-6560/aa779e.

[180] G. Tortorelli, L. Di Murro, R. Barbarino, S. Cicchetti, D. di Cristino, M. D. Falco, et al., Standard or hypofractionated radiotherapy in the postoperative treatment of breast cancer: a retrospective analysis of acute skin toxicity and dose inhomogeneities, BMC Cancer 13 (1) (2013) p. 230, DOI: 10.1186/1471-2407-13-230.

[181] K.-R. Trott, W. Doerr, A. Facoetti, J. Hopewell, J. Langendijk, P. van Luijk, et al., Biological mechanisms of normal tissue damage: Importance for the design of NTCP models, Radiotherapy and Oncology 105 (1) (2012) pp. 79–85, DOI: 10.1016/j.radonc.2012.05.008.

[182] A. Tzedakis, J. E. Damilakis, M. Mazonakis, J. Stratakis, H. Varveris, N. Gourtsoyiannis, Influence of initial electron beam parameters on Monte Carlo calculated absorbed dose distributions for radiotherapy photon beams, Med Phys 31 (4) (2004) pp. 907–913, DOI: https://doi.org/10.1118/1.1668551.

[183] J. S. Vaidya, F. Wenz, M. Bulsara, J. S. Tobias, D. J. Joseph, M. Keshtgar, et al., Risk-adapted targeted intraoperative radiotherapy versus whole-breast radiotherapy for breast cancer: 5-year results for local control and overall survival from the TARGIT-A randomised trial, Lancet 383 (9917) (2014) pp. 603–13, DOI: 10.1016/S0140-6736(13)61950-9.

[184] A. Van Esch, K. Basta, M. Evrard, M. Ghislain, F. Sergent, D. P. Huyskens, The Octavius1500 2D ion chamber array and its associated phantoms: dosimetric characterization of a new prototype, Med Phys 41 (9) (2014) p. 091708, DOI: 10.1118/1.4892178.

[185] D. Vasiljevic, C. Arnold, D. Neuman, K. Fink, M. Popovscaia, I. Kvitsaridze, et al., Occurrence of pneumonitis following radiotherapy of breast cancer - A prospective study, Strahlenther Onkol 194 (6) (2018) pp. 520–532, DOI: 10.1007/s00066-017-1257-z.

[186] D. Verellen, M. D. Ridder, N. Linthout, K. Tournel, G. Soete, G. Storme, Innovations in image-guided radiotherapy, Nature Reviews Cancer 7 (12) (2007) pp. 949–960, DOI: 10.1038/nrc2288.

[187] U. Veronesi, R. Orecchia, P. Maisonneuve, G. Viale, N. Rotmensz, C. Sangalli, et al., Intraoperative radiotherapy versus external radiotherapy for early breast cancer (ELIOT): a randomised controlled equivalence trial, Lancet Oncol 14 (13) (2013) pp. 1269–77, DOI: 10.1016/S1470-2045(13)70497-2.

[188] R. Visser, D. J. Wauben, M. de Groot, J. Godart, J. A. Langendijk, A. A. van't Veld, et al., Efficient and reliable 3D dose quality assurance for IMRT by combining independent dose calculations with measurements, Med Phys 40 (2) (2013) p. 021710, DOI: 10.1118/1.4774048.

[189] J. H. W. de Vries, E. Seravalli, A. C. Houweling, S. J. Woodings, R. van Rooij, J. W. H. Wolthaus, et al., Characterization of a prototype MR-compatible Delta4 QA system in a 1.5 tesla MR-linac, Physics in Medicine & Biology 63 (2) (2018) 02NT02, DOI: 10.1088/1361-6560/aa9d26.

[190] J. Z. Wang, X. A. Li, Impact of tumor repopulation on radiotherapy planning, International Journal of Radiation Oncology*Biology*Physics 61 (1) (2005) pp. 220–227, DOI: https://doi.org/10.1016/j.ijrobp.2004.09.043.

[191] K. Wang, M. J. Eblan, A. M. Deal, Cardiac toxicity after radiotherapy for stage III non-small-cell lung cancer: pooled analysis of dose-escalation trials delivering 70 to 90 Gy, J Clin Oncol 35 (2017), DOI: 10.1200/JCO.2016.70.0229.

[192] Y. Wang, T. R. Mazur, O. Green, Y. Hu, H. Li, V. Rodriguez, et al., A GPU-accelerated Monte Carlo dose calculation platform and its application toward validating an MRI-guided radiation therapy beam model, Med Phys 43 (7) (2016) pp. 4040–4052, DOI: https://doi.org/10.1118/1.4953198.

[193] J. Welsh, S. H. Settle, A. Amini, L. Xiao, A. Suzuki, Y. Hayashi, et al., Failure patterns in patients with esophageal cancer treated with definitive chemoradiation, Cancer 118 (10) (2012) pp. 2632–40, DOI: 10.1002/cncr.26586.

[194] M. Wendling, L. J. Zijp, L. N. McDermott, E. J. Smit, J. J. Sonke, B. J. Mijnheer, et al., A fast algorithm for gamma evaluation in 3D, Med Phys 34 (5) (2007) pp. 1647–54, DOI: 10.1118/1.2721657.

[195] A. M. Werensteijn-Honingh, P. S. Kroon, D. Winkel, E. M. Aalbers, B. van Asselen, G. H. Bol, et al., Feasibility of stereotactic radiotherapy using a 1.5 T MR-linac: Multi-fraction treatment of pelvic lymph node oligometastases, Radiother Oncol 134 (2019) pp. 50–54, DOI: 10.1016/j.radonc.2019.01.024.

[196] E. A. White, J. Cho, K. A. Vallis, M. B. Sharpe, G. Lee, H. Blackburn, et al., Cone beam computed tomography guidance for setup of patients receiving accelerated partial breast irradiation, Int J Radiat Oncol Biol Phys 68 (2) (2007) pp. 547–54, DOI: 10.1016/j.ijrobp.2007.01.048.

[197] J. B. Wilkinson, P. D. Beitsch, C. Shah, D. Arthur, B. G. Haffty, D. E. Wazer, et al., Evaluation of current consensus statement recommendations for accelerated partial breast irradiation: a pooled analysis of William Beaumont Hospital and American Society of Breast Surgeon MammoSite Registry Trial Data, Int J Radiat Oncol Biol Phys 85 (5) (2013) pp. 1179–85, DOI: 10.1016/j.ijrobp.2012.10.010.

[198] M. J. Willemink, P. B. Noël, The evolution of image reconstruction for CT—from filtered back projection to artificial intelligence, European Radiology 29 (5) (2019) pp. 2185–2195, DOI: 10.1007/s00330-018-5810-7.

[199] D. Winkel, G. H. Bol, P. S. Kroon, B. van Asselen, S. S. Hackett, A. M. Werensteijn-Honingh, et al., Adaptive radiotherapy: The Elekta Unity MR-linac concept, Clin Transl Radiat Oncol 18 (2019) pp. 54–59, DOI: https://doi.org/10.1016/j.ctro.2019.04.001.

[200] J. W. H. Wolthaus, J.-J. Sonke, M. van Herk, E. M. F. Damen, Reconstruction of a time-averaged midposition CT scan for radiotherapy planning of lung cancer patients using deformable registrationa), Medical Physics 35 (9) (2008) pp. 3998–4011, DOI: https://doi.org/10.1118/1.2966347.

[201] S. J. Woodings, J. J. Bluemink, J. H. W. de Vries, Y. Niatsetski, B. van Veelen, J. Schillings, et al., Beam characterisation of the 1.5 T MRI-linac, Phys Med Biol 63 (8) (2018) p. 085015, DOI: 10.1088/1361-6560/aab566.

[202] A. J. Wu, W. R. Bosch, D. T. Chang, T. S. Hong, S. K. Jabbour, L. R. Kleinberg, et al., Expert Consensus Contouring Guidelines for Intensity Modulated Radiation Therapy in Esophageal and Gastroesophageal Junction Cancer, Int J Radiat Oncol Biol Phys 92 (4) (2015) pp. 911–20, DOI: 10.1016/j.ijrobp.2015.03.030.

[203] B. Yang, Y. S. Wong, W. W. Lam, H. Geng, C. Y. Huang, K. K. Tang, et al., Initial clinical experience of patient-specific QA of treatment delivery in online adaptive radiotherapy using a 1.5 T MR-Linac, Biomedical Physics & Engineering Express 7 (3) (2021) p. 035022, DOI: 10.1088/2057-1976/abfa80.

[204] J. Yang, S. Vedam, B. Lee, P. Castillo, A. Sobremonte, N. Hughes, et al., Online adaptive planning for prostate stereotactic body radiotherapy using a 1.5 Tesla magnetic resonance imaging-guided linear accelerator, Physics and Imaging in Radiation Oncology 17 (2021) pp. 20–24, DOI: https://doi.org/10.1016/j.phro.2020.12.001.

[205] Y. M. Yang, M. Geurts, J. B. Smilowitz, E. Sterpin, B. P. Bednarz, Monte Carlo simulations of patient dose perturbations in rotational-type radiotherapy due to a transverse magnetic field: a tomotherapy investigation, Med Phys 42 (2015), DOI: 10.1118/1.4905168.

[206] L. Yin, H. Wu, J. Gong, J. H. Geng, F. Jiang, A. H. Shi, et al., Volumetric-modulated arc therapy vs. c-IMRT in esophageal cancer: a treatment planning comparison, World J Gastroenterol 18 (37) (2012) pp. 5266–75, DOI: 10.3748/wjg.v18.i37.5266.

[207] O. Zelyak, B. Fallone, J. St. Aubin, TH-AB-BRA-09: Stability Analysis of a Novel Dose Calculation Algorithm for MRI Guided Radiotherapy, Med Phys 43 (6Part44) (2016) pp. 3855–3855, DOI: https://doi.org/10.1118/1.4958060.

[208] W. Z. Zhang, T. T. Zhai, J. Y. Lu, J. Z. Chen, Z. J. Chen, D. R. Li, et al., Volumetric modulated arc therapy vs. c-IMRT for the treatment of upper thoracic esophageal cancer, PLoS One 10 (3) (2015) e0121385, DOI: 10.1371/journal.pone.0121385.

8 Statement on own contribution

Statement of own contribution of the dissertation

This thesis was conducted in the section for Biomedical Physics at the University hospital for Radiationoncology Tübingen under supervision of Prof. Dr. rer. nat. Daniela Thorwarth.

The study was designed in collaboration with Prof. Dr. rer. nat. Daniela Thorwarth and Prof. Dr. med. Daniel Zips.

Parts of this thesis are published as peer-reviewed papers and correlating statement of contributions for each of the collective work are listed as follows.

I assure, that I have written the manuscript myself and not to have used any other sources than those given by me.

Tübingen, the 15.10.2021

Comparison of treatment plans for a high-field MRI-linac and a conventional linac for esophageal cancer

Statement of own contribution: **Marcel Nachbar**

Title: Comparison of treatment plans for a high-field MRI-linac and a conventional linac for esophageal cancer

Authors: M. Nachbar, D. Mönnich, P. Kalwa, D. Zips, D. Thorwarth and C. Gani

Published in: Strahlentherapie und Onkologie 2019 Vol. 195 Issue 4 Pages 327-334

The original research article was conducted in the section for Biomedical Physics at the University hospital for Radiation Oncology Tübingen under supervision of Prof. Dr. rer. nat. Daniela Thorwarth.

The study was designed in collaboration with Prof. Dr. rer. nat. Daniela Thorwarth and Dr. rer. nat. David Mönnich, who additionally supported me in clinical treatment planning.

I conducted the study by creating all treatment plans. All analysis for robust analyzation of entrance angles as well as the comparison of the specified techniques was done by me.

The statistical analysis of the results as well as a co-conception of the manuscript with Dr. med. Gani was done by me.

Prof. Dr. med. Zips and Dr. med. Gani gave advice about medical issues and evaluated the generated treatment plans. Mr. Kalwa supported in a generation of available patient data and first installation of the system.

All co-authors of the publication provided critical proofreading of the manuscript.

Development and validation of a 1.5 T MR-Linac full accelerator head and cryostat model for Monte Carlo dose simulations

Statement of own contribution: **Marcel Nachbar**

Title: Development and validation of a 1.5 T MR-Linac full accelerator head and cryostat model for Monte Carlo dose simulations

Authors: M. Friedel, M. Nachbar, D. Mönnich, O. Dohm and D. Thorwarth

Published in: Med Phys 2019 Vol. 46 Issue 11 Pages 5304-5313

The original research article was conducted in the section for Biomedical Physics at the University hospital for Radiation Oncology Tübingen under supervision of Prof. Dr. rer. nat. Daniela Thorwarth.

The study was planned in collaboration with Prof. Dr. rer. nat. Daniela Thorwarth and myself.

I setup the simulation engine on the external BWHpC Cluster, programmed parts of the code, implemented with Ms. Friedel the construction design of the MR-Linac, gave constant feedback on behalf of the simulation system and its necessities and proofread the manuscript.

In collaboration with Dr. Mönnich, I measured the beam data and identified the patient plan which was used in the simulation.

The study was conducted by Mrs. Friedel under my and Prof. Dr. rer. nat. Daniela Thorwarths supervision.

Dr Dohm gave advise about the implementation of treatment plans into the EGSnrc system.

The statistical analysis and conception of the manuscript was done by Ms Friedel.

All co-authors provided critical proofreading of the manuscript.

Quality assurance of IMRT treatment plans for a 1.5 T MR-linac using a 2D ionization chamber array and a static solid phantom

Statement of own contribution: **Marcel Nachbar**

Title: Quality assurance of IMRT treatment plans for a 1.5 T MR-linac using a 2D ionization chamber ar-ray and a static solid phantom

Authors: D. Mönnich, J. Winter, M. Nachbar, L. Künzel, S. Boeke, C. Gani, O. Dohm, D. Zips and D. Thorwarth

Published in: Physics in Medicine & Biology 2020 Vol. 65 Issue 16 Pages 16NT01

The original research article was conducted in the section for Biomedical Physics at the Universityhospital for Radiation Oncology Tübingen under supervision of Prof. Dr. rer. nat. Daniela Thorwarth.

The study was planned in collaboration with Prof. Dr. rer. nat. Daniela Thorwarth and Dr. med. Daniel Zips.

In collaboration with Dr. rer. nat. Mönnich and Ms. Winter, I measured experimental data and designed the quality assurance workflow.

The detailed implementation for given the cross calibration against the routine Linac as well as the implementation of the phantom into the treatment planning system was done by Dr. rer. nat. Mönnich, Dr. rer. nat. Dohm and myself.

The experimental data was measured by Ms. Künzel, Ms. Winter, Dr. rer. nat. Mönnich and myself.

The data collection and evaluation was done by Ms. Winter, Dr. rer. nat. Mönnich and myself. Dr. med. Böke, Dr. med. Gani, Ms. Winter, Dr. rer. nat. Mönnich and myself were involved in the generation of the verified treatment plans.

The manuscript was written by Dr. rer. nat. Mönnich and proofread by me.

All other co-authors provided critical proofreading of the manuscript.

Automatic 3D Monte-Carlo-based secondary dose calculation for online verification of 1.5 T magnetic resonance imaging guided radiotherapy

Statement of own contribution: **Marcel Nachbar**

Title: Automatic 3D Monte-Carlo-based secondary dose calculation for online verification of 1.5 T magnetic resonance imaging guided radiotherapy

Authors: M. Nachbar, D. Mönnich, O. Dohm, M. Friedlein, D. Zips and D. Thorwarth

Published in: Physics and Imaging in Radiation Oncology 2021 Vol. 19 Pages 6-12

The original research article was conducted in the section for Biomedical Physics at the University hospital for Radiation Oncology Tübingen under supervision of Prof. Dr. rer. nat. Daniela Thorwarth.

The study was planned in collaboration with Prof. Dr. rer. nat. Daniela Thorwarth and Prof. Dr. med. Daniel Zips.

The beam data collection and the programming of the automatic workflow routine was done by me. The development and implementation of the system in the online workflow setting as it is implemented in python 2.7 was done by me.

The simulated planning study was investigated by me. All The statistical analyses as well as the manuscript was done by me.

Dr. rer. nat. Mönnich and Dr. rer. nat. Dohm gave advise about the research treatment planning system Hyperion®. Dr. rer. nat. Dohm supported me in the development of a XVMC Monte Carlo accelerator head model.

Ms Winter assisted in the clinical evaluation of the secondary dose calculation system within the online adaptive workflow. Ms Friedlein helped in the data collection for patient QA and validation of code.

All co-authors provided critical proofreading of the manuscript.

Partial breast irradiation with the 1.5 T MR-Linac: First patient treatment and analysis of electron return and stream effects

Statement of own contribution: **Marcel Nachbar**

Title: Partial breast irradiation with the 1.5 T MR-Linac: First patient treatment and analysis of electron return and stream effects

Authors: M. Nachbar, D. Mönnich, S. Boeke, C. Gani, N. Weidner, V. Heinrich, M. lo Russo, L. Livi, J. Winter, S. Tsitsekidis, O. Dohm, D. Thorwarth, D. Zips and C. De-Colle

Published in: Radiotherapy and Oncology 2020 Vol. 145 Pages 30-35

The original research article was conducted in the section for Biomedical Physics at the Universityhospital for Radiation Oncology Tübingen under supervision of Prof. Dr. rer. nat. Daniela Thorwarth.

The study was planned in collaboration with Prof. Dr. rer. nat. Daniela Thorwarth and Prof. Dr. med. Daniel Zips. The concept of the partial breast irradiation was supported by Prof. Dr. Livi and Dr. Lo Russo.

I conducted the study by creation oft the treatment plan, generation of the experimental data, evaluation of electron stream effect, treatment in the online adaptive workflow and analysis of the results.

The manuscript was created by me in collaboration with Dr. med. De-Colle.

Dr. med. De-Colle, Dr. med. Böke, Dr. med. Gani, Dr. med. Weidner, Dr. med. Heinrich and Prof. Dr. med Zips were involved in the medical evaluation of the new concepted treatment plans as well as treating the patient in the online adaptive workflow.

Mr Tsitsekidis supported in the evaluation of the film dosimetry.

Ms. Winter and Dr. rer. nat. Mönnich were supporting the patient treatment as well as experimental offline patient quality assurance.

Dr . rer. nat. Mönnich and Dr. rer. nat. Dohm were in supporting with critical discussion on behalf of the simulation of electron stream effects and its reduction.

All co-authors provided critical proofreading of the manuscript.

9 Supplementary Materials

9.1 Comparison of treatment plans for a high-field MRI-linac and a conventional linac for esophageal cancer'

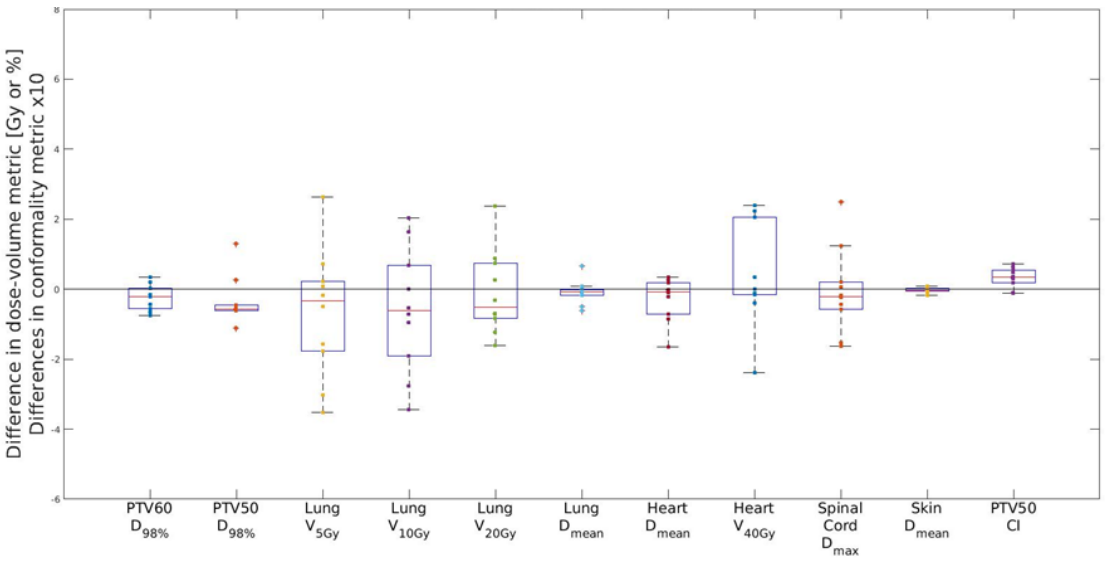

Figure S1: Differences between initial plans generated with individualized beam angles and equidistant beam angles. Positive differences mark an increase in the respective metric for the plans generated with individualized beam angles.

9.2 Development and validation of a 1.5 T MR-Linac full accelerator head and cryostat model for Monte Carlo dose simulations

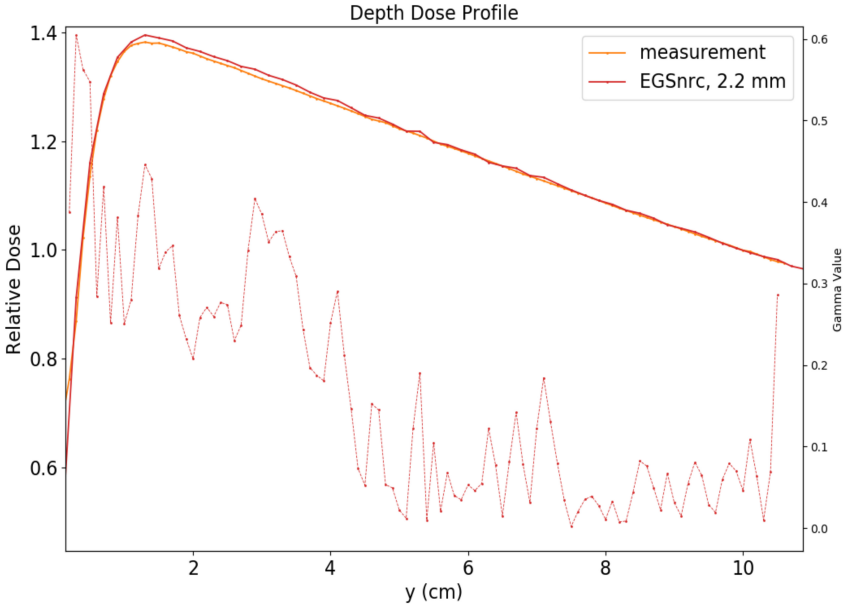

Figure S2: Comparison of measured and simulated depth dose profile of a $22 \times 22 cm^2$ field. The gamma pass rate was 100.0%.

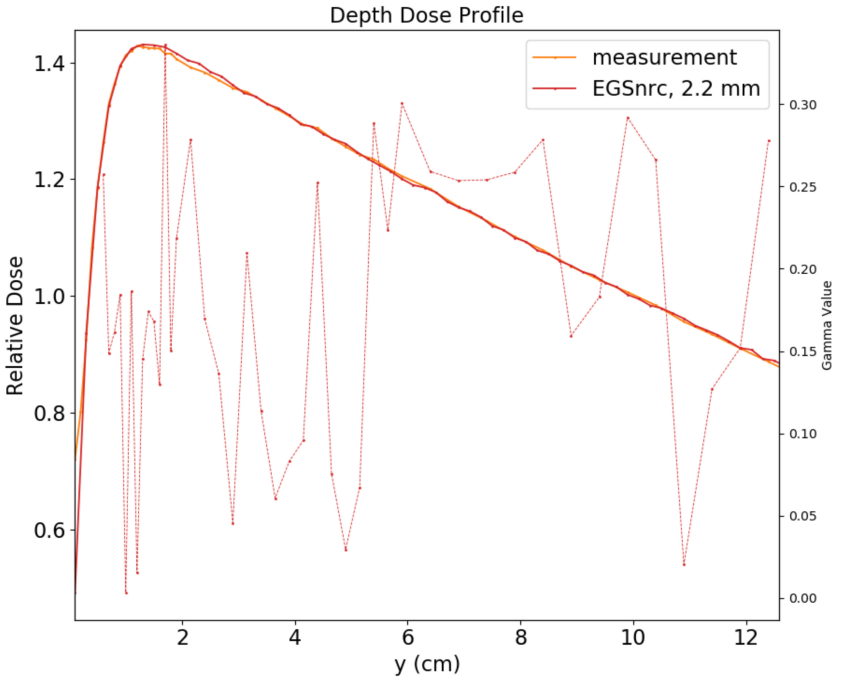

Figure S3: Comparison of measured and simulated depth dose profile of a$10 \times 10 cm^2$ field. The gamma pass rate was 100.0%

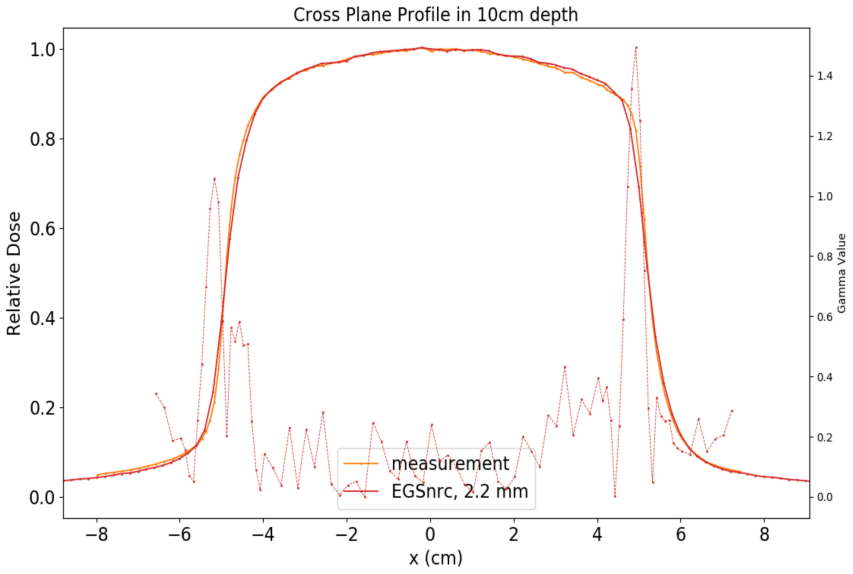

Figure S4: Comparison of measured and simulated in plane profile of a$10 \times 10cm^2$ field. The gamma pass rate was 94.44%.

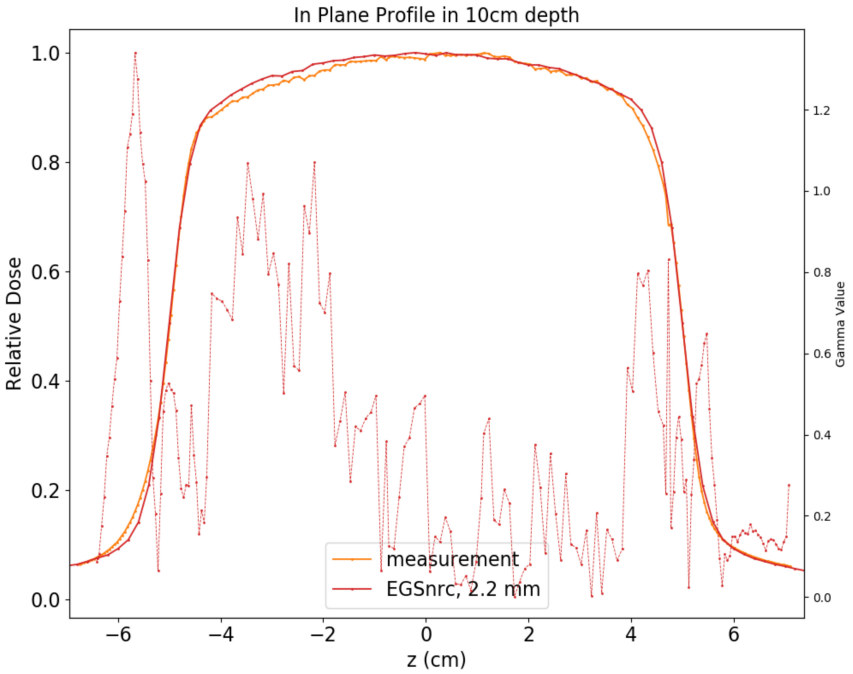

Figure S5: Comparison of measured and simulated cross plane profile of a $10 \times 10cm^2$ field. The gamma pass rate was 94.54%.

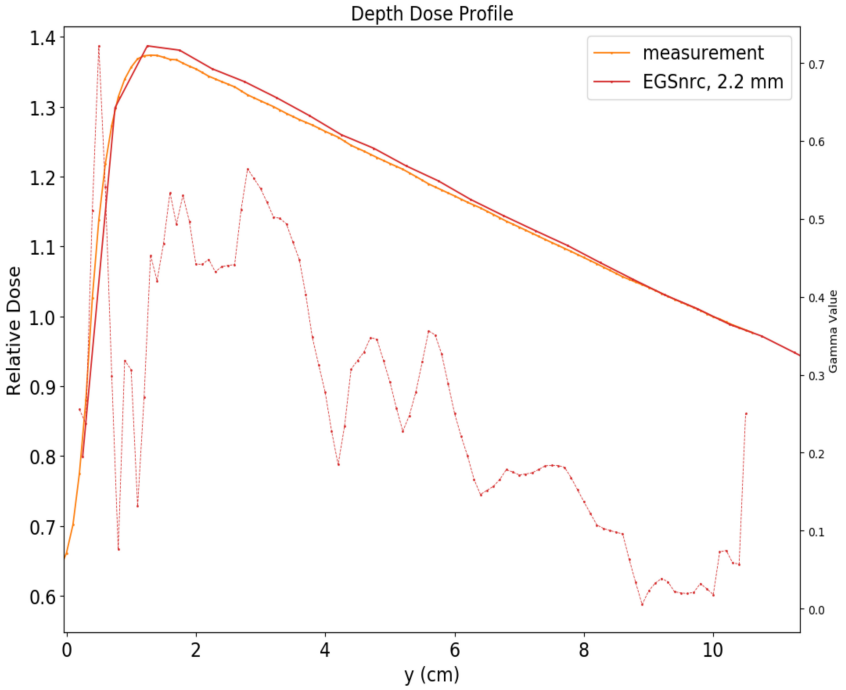

Figure S6: Comparison of measured and simulated depth dose profile of a $57 \times 22 cm^2 field$. The gamma pass rate was 100.0%.

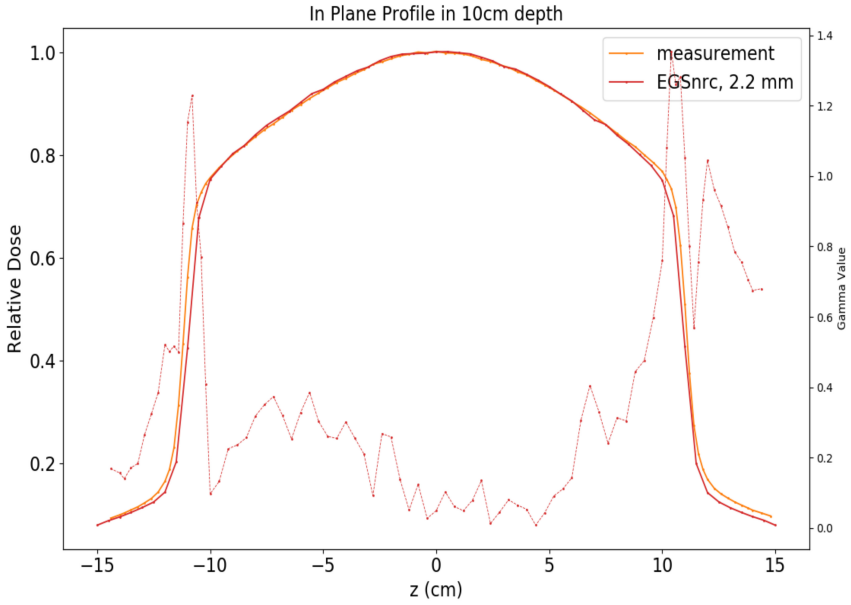

Figure S7: Comparison of measured and simulated in plane profile. The gamma passrate was 90.8%.

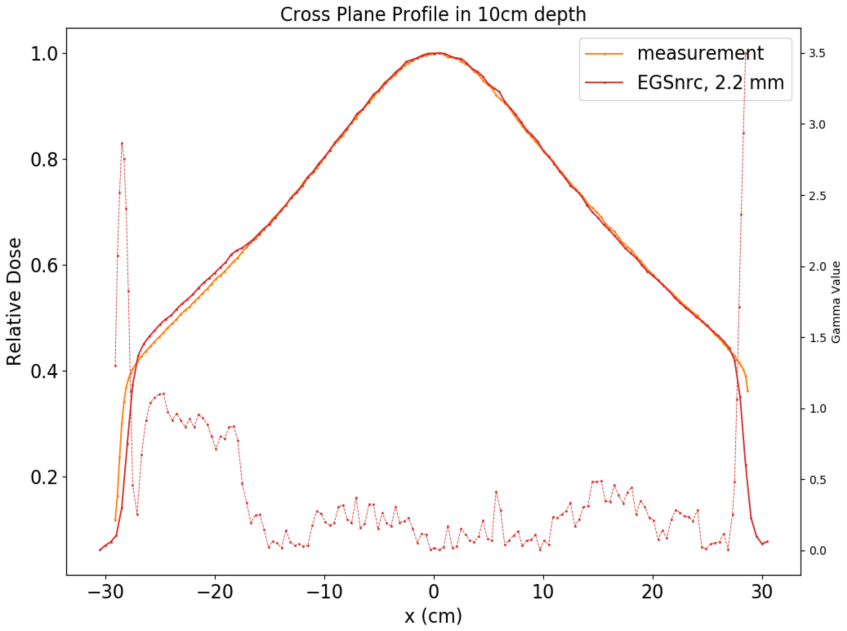

Figure S8: Comparison of measured and simulated cross plane profile. The gammapass rate was 88.89%.

9.3 Quality assurance of IMRT treatment plans for a 1.5 T MR-linac using a 2D ionization chamber array and a static solid phantom

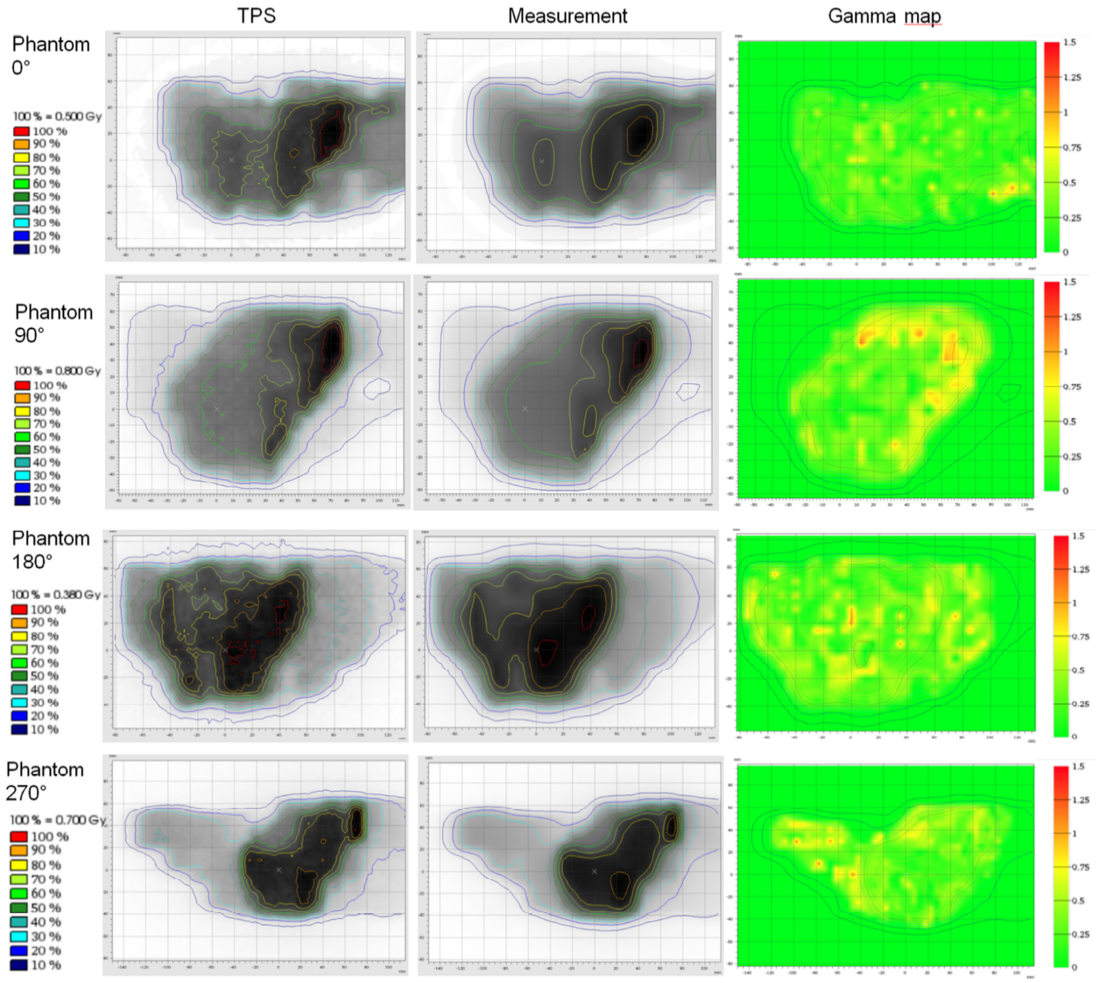

Figure S9: Gamma evaluation of the reference treatment plan of patient 52, which was measured using four phantom setups. The plan is a nine beam step-and-shoot IMRT plan with 427 MUs and 31 segments, treating the prostate bed with 30 fractions of 2 Gy. Phantom setups 0°, 90°, 180°, 270° combine measurements of beams angles 25°/60°, 100°/140°, 180°/220° and 260°/300°/340°, respectively. The pass rates were 99.0%, 98.9%, 99.4% and 98.6% respectively.

Table S1: Detailed list of measured patient treatment plans

			Gamma Pass Rate (%)					Plan Characteristics		
Patient	Type	Average All Setups	Phantom 0°	Phantom 90°	Phantom 180°	Phantom 270°	0=Ref, 1=Adapted	Number Beams	Number Segments	Total MU
14	LN met	99,7	100,0	100,0	98,9	100,0	0	7	66	914
14		99,6	100,0	99,3	99,5		1			
14		99,9	100,0	100,0	99,5	100,0	1			
15	LN met	98,1	100,0	94,2		100,0	0	7	52	1355
15		98,7	99,6	96,5		100,0	1			
16	LN met	97,9	97,1	99,1	99,6	95,8	0	8	72	981
16		98,7	98,4	99,5	99,7	97,3	1			
30	LN met	98,4	100,0	100,0	94,9	98,8	0	7	34	498
30		98,7	100,0	100,0	94,7	100,0	1			
30		95,6	100,0	98,7	83,7	100,0	1			
30		97,2	100,0	93,9	94,7	100,0	1			
30		97,6	100,0	93,6	97,4	99,3	1			
33	LN met	98,9	99,5	100,0	96,2	100,0	0	8	31	537
33		98,8	99,8	98,9	96,8	100,0	1			
21	Liver	98,3	100,0		96,0	99,0	0	4	33	861
21		98,6	100,0		95,7	100,0	1			
45	Liver	99,2	99,2		98,3	100,0	0	6	45	976
45		100,0	100,0		100,0	100,0	1			
29	Liver	97,9	100,0	95,1	96,6	100,0	0	9	57	4938
29		99,3	100,0	99,0	98,9		1			
32	Liver	99,2	100,0		97,9	99,7	0	8	60	1235
32		100,0	100,0		100,0	100,0	1			
41	Liver	98,9	99,4	97,4	98,9	100,0	0	8	58	955
41		99,9	99,4	100,0	100,0	100,0	1			
46	Liver	100,0	100,0		100,0	100,0	0	11	31	2593
46		100,0	100,0		100,0	100,0	1			
47	Liver	97,6	100,0		93,3	99,6	0	8	55	1543
47		99,0	100,0		99,1	97,8	1			
49	Liver	99,7	100,0	98,8	100,0	100,0	0	9	70	1813
49		99,1	100,0	96,5	100,0	100,0	1			
53	Liver	98,3	100,0	94,4	98,9	100,0	0	9	60	1318
57	Liver	99,8	100,0	100,0	99,3	100,0	0	9	59	1543
60	Liver	98,6	98,4	97,5	100,0	98,5	0	9	55	2490
61	Liver	99,8	100,0	99,0	100,0	100,0	0	9	68	2198
62	Liver	100,0	100,0	100,0	100,0	100,0	0	10	58	2991
17	PBI	97,3	95,9	96,4		99,5	0	5	13	410
17		97,7	100,0	93,1		100,0	1			
19	PBI	97,1	96,4	96,2		98,8	0	6	20	472
19		98,0	98,0	97,0		99,0	1			
22	PBI	98,4	96,2		99,7	99,4	0	6	32	588
22		97,2	98,5		95,9		1			
25	PBI	99,3	97,8		100,0	100,0	0	6	19	414
25		98,2	97,3		97,3	100,0	1			
27	PBI	98,5	95,6		100,0	100,0	0	6	25	576

27		97,3	96,5		98,2	97,3	1			
31	PBI	96,8	94,6		97,5	98,3	0	6	23	475
31		99,3	99,7		99,4	98,7	1			
35	PBI	95,7	90,0	99,1		97,9	0	7	21	431
35		99,5	100,0	100,0		98,4	1			
37	PBI	98,4	98,6		97,0	99,5	0	7	32	651
37		94,4	99,1		97,6	86,4	1			
39	PBI	98,9	99,2	98,4		99,1	0	7	25	586
39		96,5	100,0	90,9		98,7	1			
44	PBI	98,5	98,9	97,7		98,8	0	7	27	556
18	PC	98,8	99,1	97,5	98,8	99,7	0	9	33	435
18		97,9	96,5	99,4	97,1	98,6	1			
36	PC	99,1	99,2	99,4	98,9	98,7	0	9	21	475
36		98,5	96,0	100,0	98,0	100,0	0	9	28	593
36		99,0	99,2	99,2	100,0	97,4	1			
38	PC	99,1	99,2	98,9	98,8	99,5	0	9	33	605
38		98,6	99,2	97,9	100,0	97,2	0			
38		99,6	100,0	99,3	99,2	100,0	1			
43	PC	95,6	88,9	95,5	97,8	100,0	0	8	21	1507
43		100,0	100,0	100,0	100,0	100,0	1			
52	PC	99,0	99,0	98,9	99,4	98,6	0	9	31	427
52		99,3	98,2	99,4	99,8	99,6	1			
54	PC	99,3	99,2	100,0	97,8	100,0	0	9	14	288
54		99,3	98,9	98,3	100,0	100,0	1			
56	PC	99,3	100,0	100,0	99,0	98,1	0	9	21	290
56		98,8	99,3	100,0	99,7	96,0	1			
58	PC	98,2	97,6	99,1	97,2	99,0	0	9	27	358
59	PC	99,0	99,3	97,8	99,0	100,0	0	9	35	590
59		99,7	100,0	99,1	100,0	99,5	1			
20	Rectum	94,5	95,3	93,8	98,5	90,4	0	9	36	478
20		95,3	95,4	94,9	97,8	92,9	1			
20		98,5	99,1	96,3	99,9	98,5	1			
23	Rectum	95,4	94,1	94,0	99,0	94,5	0	9	29	389
23		93,9	94,3	97,4	91,5	92,4	1			
24	Rectum	93,3	96,5	84,6	98,6	93,5	0	9	24	382
24		93,1	92,8	91,0	94,8	93,8	1			
28	Rectum	96,2	93,9	97,8	99,6	93,3	0	8	42	501
28		91,8	90,8	96,7	98,5	81,0	1			
50	Rectum	94,0	88,9	93,6	99,2	94,4	0	9	26	328
50		94,5	98,9	87,6	99,8	91,6	1			
55	Rectum	90,4	95,1	89,3	96,0	81,0	0	9	36	432
55		90,3	95,5	85,6	95,2	84,9	1			
63	Rectum	88,6	86,3	84,3	98,4	85,4	0	9	51	577
34	HN	98,9	99,3	98,7	98,8	98,6	0	9	56	629
34		97,4	97,2	98,7	97,5	96,3	1			
34		99,7	100,0	100,0	98,8	100,0	1	9	24	387
42	HN	97,7	97,8	95,8	99,4	97,9	0	8	48	692
42		96,2	95,9	94,6	98,5	95,7	1			
42		98,1	98,7	95,5	98,6	99,5	1	9	49	822
66	HN	94,6	99,2	91,8	89,7	97,7	0	9	42	524
40	Pancreas	94,3		100,0	82,8	100,0	0	7	28	891

40		98,2		100,0	94,5	100,0	1			
48	Pancreas	99,6		100,0	100,0	98,9	0	7	50	1034
48		99,6		100,0	100,0	98,8	1			
26	Other	97,0	92,6	100,0	95,4	100,0	0	7	46	738
26		99,3	99,7	99,6	98,4	99,5	1			
51	Other	98,7	96,2	100,0	100,0		0	7	16	1543
51		96,1	93,5	96,1	98,7		1			
64	Other	94,9	86,8	94,9	98,9	99,1	0	9	34	391
65	Other	93,2	86,6	89,1	98,6	98,3	0	9	37	431
65		93,1	89,6	89,0	98,7	95,2	1			
67	Other	98,2	97,7	96,3	99,3	99,4	0	9	57	1109
Median Gamma Pass Rate All Plans (%)		98,5	99,2	98,4	98,8	99,4				
Min (%)		88,6	86,3	84,3	82,8	81,0		4	13	288
Max (%)		100,0	100,0	100,0	100,0	100,0		11	72	4938
Standard Deviation (%)		2,3	3,3	3,8	2,9	3,9				

9.4 Automatic 3D Monte-Carlo-based secondary dose calculation for online verification of 1.5 T magnetic resonance imaging guided radiotherapy

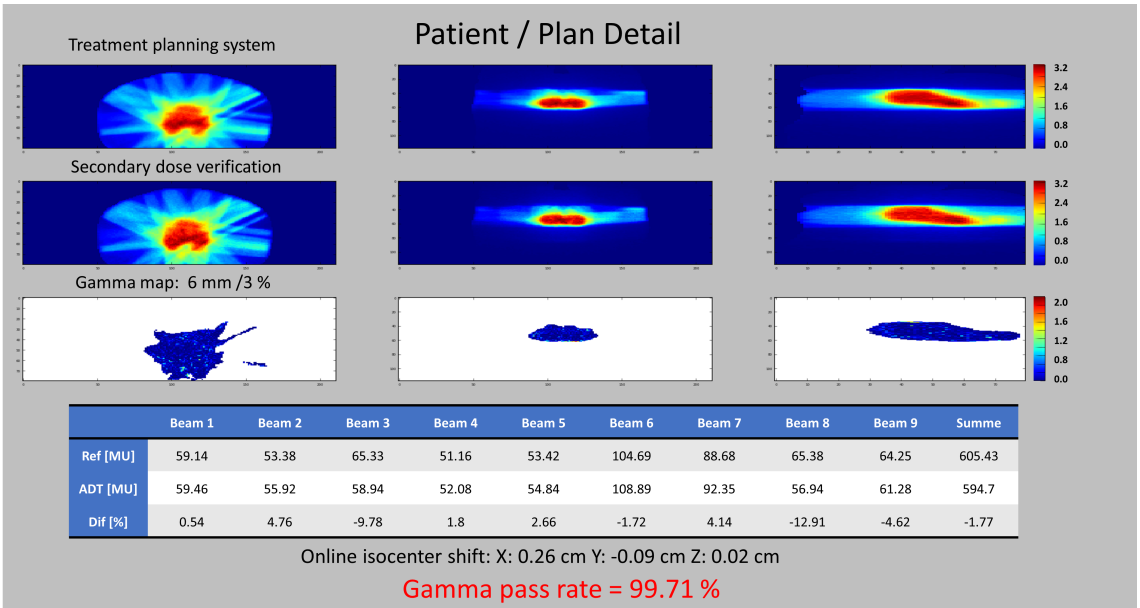

	Beam 1	Beam 2	Beam 3	Beam 4	Beam 5	Beam 6	Beam 7	Beam 8	Beam 9	Summe
Ref [MU]	59.14	53.38	65.33	51.16	53.42	104.69	88.68	65.38	64.25	605.43
ADT [MU]	59.46	55.92	58.94	52.08	54.84	108.89	92.35	56.94	61.28	594.7
Dif [%]	0.54	4.76	-9.78	1.8	2.66	-1.72	4.14	-12.91	-4.62	-1.77

Figure S10: Graphical user interface in the online workflow. Shown is the transversal, sagittal and coronal view at the maximal dose point of the treatment planning system. The SDC and gamma map are depicted at the corresponding position. Additionally, shown are the beam specific monitor units (MU) of the reference plan (Ref), the adapted plan (ADT) and their percentage difference (Dif). Additionally, shown is the isocenter shift in the online adaptation and the gamma passing rate.

Table S3: Output factor from 0 and 270 degrees normalized to the reference field of 10 x 10 cm² at isocenter position for the measurement, secondary dose calculation (SDC) and treatment planning system (TPS). Field sizes are defined at the isocenter position in crossplane × inplane [CP × IP].

Output factor 0 °	**Area [cm²]**	**Measure-ment**	**SDC [%]**		**TPS**	
Field size [CP x IP]			**Relative value**	**Relative deviation [%]**	**Relative value**	**Relative deviation [%]**
2 × 2 cm²	4	0.81	0.80	-0.92	0.80	-1.00
3 × 3 cm²	9	0.87	0.84	-2.19	0.85	-1.17
5 × 5 cm²	25	0.92	0.89	-2.60	0.92	-0.24
10 × 10 cm²	100	1	1.00	0.00	1.00	0.00
15 × 15 cm²	225	1.05	1.04	-1.06	1.05	-0.42
22 × 22 cm²	484	1.11	1.07	-3.64	1.10	-0.72
40 × 22 cm²	880	1.15	1.08	-6.36	1.13	-1.39
Output factor 270 °	**Area [cm²]**	**Measure-ment**	**SDC [%]**		**TPS**	
Field size [CP x IP]			**Relative value**	**Relative deviation [%]**	**Relative value**	**Relative deviation [%]**
2 × 2 cm²	4	0.79	0.80	1.57	0.77	-1.97
3 × 3 cm²	9	0.85	0.85	0.13	0.85	-0.44
5 × 5 cm²	25	0.91	0.91	0.29	0.91	-0.47
10 × 10 cm²	100	1	1.00	0.00	1.00	0.00
16 × 16 cm²	256	1.08	1.06	-1.56	1.07	-0.13

9.5 Partial breast irradiation with the 1.5 T MR-Linac: First patient treatment and analysis of electron return and stream effects

Figure S11: Visualization of patient´s set up, with wingboard, 1 cm bolus, feet immobilization device and the MR coil.

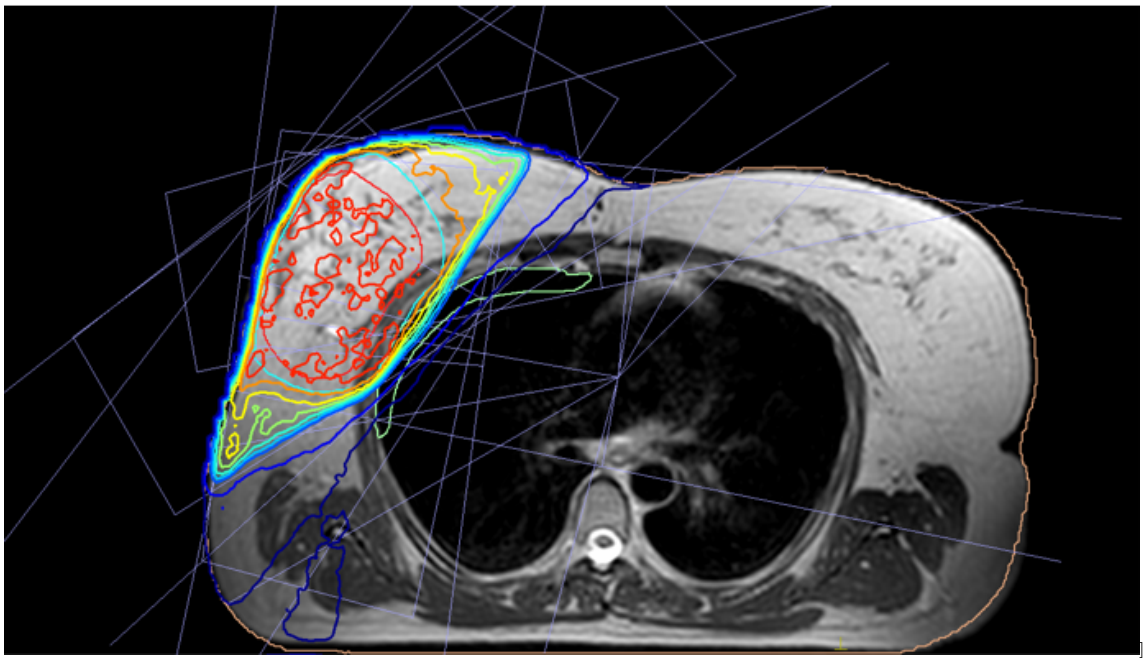

Figure S12: Visualization of the IMRT step-and-shoot plan with the 7 beams angles: 5 °/ 30°/ 45°/ 195°/ 240°/ 260°/ 280°.

10 Acknowledgments

Throughout the writing of this thesis and the continuous development of MR-guided radiotherapy i have received a great amount of support and assistance from great people out of every possible direction.
First, I would like to thank my supervisor Professor Daniela Thorwarth, whose detailed and constant input always inspired me and made me truly enjoy the scientific work.
In the same context, i would like to thank Professor Daniel Zips for his constant support and trust. The occasionally push into new waters helped me develop in different ways.
In addition i would like to thank the two different groups, within the clinic, which i am happy to be part of.
First i would like to thank the biomedical physics research group for the amazing collaboration. Without them the nights of measurements, analysis, conferences, writing of abstracts or playing table football would have not been the same. Even though all of them were part of this journey, i especially want to thank Dr. David Mönnich and Dr. Sara Leibfarth individually as they mentored me on and off the clinic.
Secondly i of course want to thank the applied MR-Linac group! This collaboration of amazing physicians such as Dr. Gani, Dr. Böke, Dr. De-Colle and Dr. Wegener with amazing RTTs such as A. Stolte, J. Boldt and S.Butzer and a great physics/engineering team with Dr. Dohm, Dr. Mondry, Dr. Voigt and N. Patel just made this possible. It is just the greatest possible pleasure to work with such dynamic and motivated colleagues.
In addition i would like to thank my parents for their full limitless support, constant motivation and open ears during difficult times.
Finally i want to thank Monica Lo Russo, without whom, i could not have finished this work. Your happy spirit, believe in me and absolute support even during difficult times was sometimes the only thing, which kept me going.